A nano-liquid hub integrating growth and immune-evasion signaling to promote survival

Authors

Taka A. Tsunoyama[1], Christian Hoffmann[2], Daiki Sasaki[3], Cheng Tan[4], Bo Tang[1], Koichiro M. Hirosawa[5], Yuri L. Nemoto[6,7], Rinshi S. Kasai[8], Takahiro K. Fujiwara[9], Kenichi G. N. Suzuki[5,8,9], Yuji Sugita[4,10,11], Hiroki Ishikawa[3], Dragomir Milovanovic[2], Akihiro Kusumi[1,9]*

Affiliations

[1]Membrane Cooperativity Unit; Okinawa Institute of Science and Technology Graduate University (OIST); Onna-son, Okinawa, 904-0495; Japan.

[2]Institute of Biochemistry, Charité – Berlin University of Medicine; Berlin, 10117; Germany.

[3]Immune Signal Unit; Okinawa Institute of Science and Technology Graduate University (OIST); Onna-son, Okinawa, 904-0495; Japan.

[4]Computational Biophysics Research Team; RIKEN Center for Computational Science; Kobe, Hyogo, 650-0047; Japan.

[5]Institute for Glyco-Core Research (iGCORE); Gifu University; Gifu, 501-1193; Japan.

[6]Biosignal Research Center; Kobe University, Kobe, Hyogo, 657-8501, Japan.

[7]Department of Biochemistry and Molecular Biology; Kobe University Graduate School of Medicine, Kobe, Hyogo, 650-0017, Japan.

[8]Division of Advanced Bioimaging; National Cancer Center Research Institute; Tokyo, 104-0045; Japan.

[9]Institute for Integrated Cell-Material Sciences (WPI-iCeMS); Kyoto University; Kyoto, 606-8501; Japan.

[10]Theoretical Molecular Science Laboratory; RIKEN Pioneering Research Institute; Wako, Saitama, 351-0198; Japan.

[11]Department of Physics; University of Tokyo; Tokyo 113–0033; Japan.

Contact info

*Corresponding author. Email: akihiro.kusumi@oist.jp

Keywords

single-molecule imaging, signal integration hub, receptor-type tyrosine kinases, CD59, PDGF receptor, immune evasion, cell growth and survival, lipid raft domain, liquid-liquid phase separation, cancer

Highlights

- GEM is a metastable hub physically integrating growth and immune evasion signaling
- GEM is a ≈34-nm nano-liquid protein co-condensate coupling CD59 and RTK signaling
- Nano-liquid confinement drives FAK–SFK chain activation and supralinear amplification
- GEM promotes tumor growth in mice by coupling growth and CD59 evasion signaling

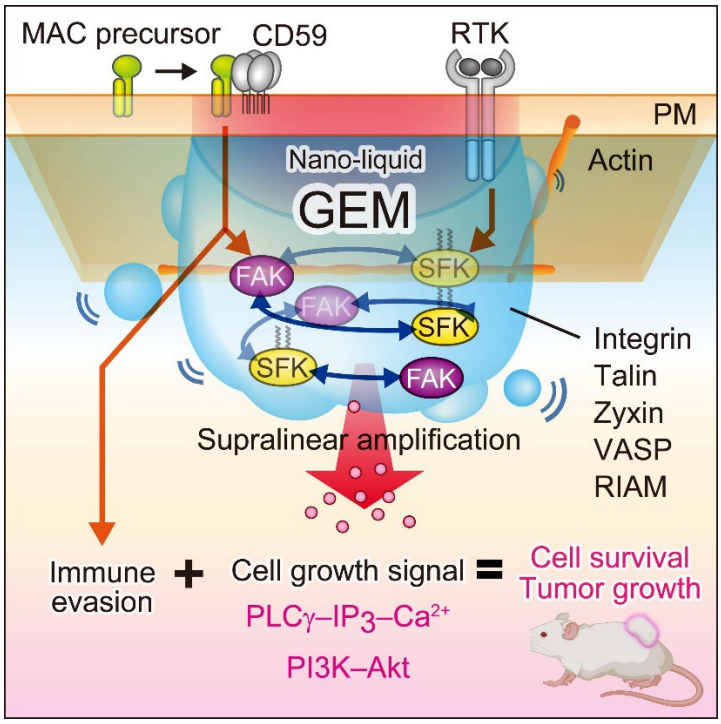

SUMMARY

Cell survival in immune-competent organisms relies on both growth and immune evasion, yet these processes have been studied as independent cellular programs. Here, using super-resolution single-molecule imaging, we identify GEM (Growth and Evasion Metastable hub), a ≈34-nm, metastable, nano-liquid, plasma membrane hub that physically integrates receptor-type tyrosine kinase (RTK) inputs with CD59-mediated immune-evasion signaling within the same assembly. GEM is formed by LLPS-like clustering on PI(4,5)P_2-containing raft nanodomains, driven by zyxin's intrinsically disordered region together with integrin-associated proteins, while remaining distinct from canonical integrin adhesions. Upon concurrent RTK and CD59 stimulations, GEM recruits both receptors and their respective downstream kinases (SFKs and focal adhesion kinase), enabling reciprocal chain activation via nano-liquid confinement that supralinearly amplifies PLCγ–IP_3–Ca^{2+} and PI3K–Akt survival signaling outputs. In mice, disrupting GEM suppresses tumor growth *in vivo*, establishing nano-liquid GEM as an integrator that physically couples growth and CD59-mediated immune-evasion signaling for cell survival.

INTRODUCTION

Cell survival in multicellular organisms with active immune systems depends on both growth signaling and mechanisms that protect cells from self-directed immune attack, yet these processes have traditionally been studied as independent cellular programs. As a result, whether growth and immune-evasion signals can be coordinated, let alone organized within shared plasma-membrane (PM) architectures, has remained largely unexplored. To address this issue, we asked whether and how growth and immune-evasion signals might be physically coordinated by dedicated architectures.

Growth signaling, typically mediated by receptor-type tyrosine kinases (RTKs) at the plasma membrane (PM), has been extensively characterized as a central driver of cell proliferation and survival.[1] Immune evasion can occur through diverse mechanisms; in this study, we focus on immune evasion in the form of resistance to complement-dependent cytotoxicity (CDC), because CDC, like RTK signaling, is initiated at the PM. CD59, a glycosylphosphatidylinositol (GPI)-anchored, raftophilic receptor expressed in virtually all cell types, is a central mediator of resistance to CDC. In the context of cancer biology, many tumors overexpress CD59.[2] CD59 prevents CDC by binding the complement C5b-8 complex, the membrane attack complex (MAC) precursor, to inhibit MAC formation.[3] Beyond this canonical role, the engagement of CD59 by MAC precursors has been reported to elicit rapid oligomerization and recruitment of cytoplasmic signaling molecules, including trimeric G proteins, Src-family kinases (SFKs) and phospholipase Cγ (PLCγ), thereby triggering proliferative signaling outputs.[4–7] PLCγ recruitment and activation occur at CD59-cluster-associated platforms.[4–6] Because these signaling molecules also operate downstream of growth-factor RTKs, growth and immune evasion signals might converge at shared membrane-associated signaling sites. Because both RTKs[8–10] and GPI-anchored receptors[11–15] can interact with integrins, we asked whether integrin-associated assemblies could provide a physical basis for such convergence.

Here, using advanced super-resolution single-molecule imaging and tracking, we identify GEM (Growth and Evasion Metastable hub), a nanoscale (≈34 nm), liquid-like, metastable, integrin-associated assemblies that integrates CD59-mediated immune-evasion signaling and growth-factor signaling. GEM consists of integrin, talin, zyxin, and other proteins associated with integrin adhesion complexes (IACs), while remaining distinct from canonical IACs, because GEM is present in the apical PM and it lacks vinculin and paxillin, essential constituent molecules for canonical IACs. GEM assembly is driven primarily by

zyxin's intrinsically disordered region (IDR) and is supported by PI(4,5)P_2-containing raft nanodomains and cortical actin, exhibiting hallmark behaviors of liquid-liquid phase separation (LLPS)-like clustering. The nano-liquid organization provides a physical basis for bringing together structurally diverse receptors and signaling molecules via weak, multivalent interactions. GEMs form constitutively at endogenous protein expression levels, at densities comparable to clathrin-coated pits (several hundred GEMs/cell), persists for ≈8.5 s, and exchange constituents with their cytoplasmic pools on second timescales.

Upon concurrent RTK and CD59 stimulations, GEM recruits both receptors together with their respective downstream kinases, SFKs and focal adhesion kinase (FAK), and cooperatively produces supralinear amplification of PLCγ-IP_3-Ca^{2+} and PI3K-Akt signals, key signaling outputs essential for cell survival. We propose that confinement within the nano-liquid GEM environment enables cooperative kinase activation that underlies this supralinearity. GEM also enhances CD59-dependent immune evasion from CDC by facilitating encounters between CD59 and MAC precursors. In murine tumor models, restoration of GEM formation markedly enhances tumor growth, while disruption of GEM attenuates it.

Taken together, these findings identify GEM as a metastable, nano-liquid PM hub in which growth signaling and CD59-associated complement evasion, long treated as independent survival programs, are physically coordinated within a shared nano-liquid domain. This framework links nanoscale architecture on the PM to functional coupling of proliferative signaling and CDC resistance *in vivo*, and provides a basis for understanding how such organization can be leveraged in cancer.

120 **RESULTS**

GPI-anchored receptors, engaged RTKs, and PLCγ1 are transiently recruited to talin clusters on the apical plasma membrane

Talin is a large, multidomain integrin-associated protein that links integrins to multiple interaction partners and is essential for the assembly and function of integrin–adhesion
125 complexes (IACs; throughout this report, IACs include mature focal adhesions).[16–18] We therefore began by asking whether talin-centered assemblies at the plasma membrane (PM) engage both growth signaling and CD59-mediated immune-evasion (CDC-resistance) pathways.

Unexpectedly, we found that talin forms discrete clusters on the apical PM, where
130 canonical IACs are absent. These talin clusters are immobile or slowly-diffusive and metastable, repeatedly assembling and disassembling (Video S1; Figure 1A) with an exponential lifetime of 9.0 s (Figure 1B; τ_2; STAR Methods). These clusters were detected using Halo7-tagged-talin1 molecules expressed in talin1/2 double-knockout mouse embryonic fibroblasts (dKO-MEFs)[19] at levels comparable to endogenous talin1 (Figures 1A
135 and S1A-S1G; STAR Methods; Table S1). Unless otherwise stated, tagged talin1 is simply referred to as talin hereafter. Raw data and statistical parameters, including SEMs, *p*-values, and numerical original data, are summarized in Table S1.

Single-molecule imaging revealed that ligated PDGFR molecules and signaling-active CD59 clusters (each consisting of an average of five CD59 molecules and recapitulating the
140 signaling-competent oligomers described previously[4,5]) were transiently recruited to talin clusters on the apical PM (Figures 1C-1D). Their dwell lifetimes were on the sub-second timescale (exponential time constant, τ_2[20]; Figure 1D; Video S2; STAR Methods). In contrast, non-ligated PDGFR molecules were not recruited to talin clusters, whereas non-clustered CD59 molecules were recruited less frequently and with shorter dwell lifetimes (Figure 1D).

145 To quantify recruitment, we used a single-molecule colocalization index[20,21] (Figure S1H). Engaged PDGFR and CD59 showed robust recruitment, and similar recruitment was observed for another RTK, EGFR, and another GPI-anchored receptor, Thy1 (Figure 1E), indicating that apical talin clusters can recruit receptors with highly diverse molecular architectures.

150 Talin clusters were detected in all five mammalian cell lines examined (Figure 1F). Because apical talin clusters were most readily visualized in human epithelial T24 cells, owing to their large, flat apical PM regions, we generated a T24-derived line stably

expressing SNAPf-talin at 0.7x the endogenous talin level (T24-T cells; Figures S1I-S1K), and used this line extensively in subsequent experiments. As in MEFs (Figures 1C and 1D), individual engaged CD59 clusters and ligand-bound PDGFR molecules were transiently recruited to talin clusters in T24-T cells (Figures S1L and S1M).

CD59 clusters are known to recruit a downstream cytoplasmic signaling protein involved in cell growth, PLCγ, at CD59 cluster-associated platforms.[4–6] We therefore examined whether talin clusters might serve as the physical sites where this signaling-related function of CD59 is executed. Using triple-color single-molecule imaging, we found that following the recruitment of an engaged CD59 cluster to a talin cluster, PLCγ1 molecules are transiently recruited to the same talin cluster (≈70 ms), predominantly immediately after CD59 arrival (Figures 1G-1I and Video S3). Because CD59 cannot directly bind PLCγ1, these observations suggest that, following CD59 engagement, tyrosine phosphorylated docking sites are generated at the talin cluster.[4–7] Upon PDGF stimulation, PLCγ1 is likewise transiently recruited to talin clusters with a comparable dwell lifetime (≈80 ms; Figure 1H).

Talin clusters contribute to CD59-mediated immune evasion

Whereas the preceding subsection addressed CD59-dependent growth signaling at talin clusters, we next examined whether talin clusters also contribute to CD59's canonical immune evasion function, resistance to CDC.[2] Specifically, we tested whether the bona-fide ligands of CD59, MAC precursors (C5b-8 complexes), are recruited to talin clusters. Using single-molecule imaging, we found that MAC precursors were transiently recruited to talin clusters (Figures 1J and 1K).

Because both ligated and non-ligated CD59 are recruited to talin clusters, these observations indicate that talin clusters can co-enrich CD59 and MAC precursors, enhancing local CD59-MAC precursor encounters and thereby suppressing C9 recruitment and MAC assembly.[3] Therefore, talin clusters are well positioned to facilitate CD59-mediated immune evasion via resistance to CDC (Figure 1L; also see Figure 5M).

Taken together with the results described in the preceding subsection, talin clusters show three defining features: (1) they engage growth signaling downstream from both RTKs and CD59 (Figures 1C-E and 1G-1I); (2) they are associated with CD59-mediated immune evasion via resistance to CDC (Figures 1J and 1K); and (3) they are metastable structures that repeatedly assemble and disassemble with short lifetimes (Figure 1B). Based on these combined growth- and evasion-related functions, we refer to these talin clusters as GEMs

(Growth and Evasion Metastable hubs) (Figure 1L). GEM constituent molecules (including integrin), formation mechanisms, and functional consequences are described in subsequent subsections.

GEM forms metastable liquid-like co-assemblies with zyxin

To further characterize GEM molecular composition and dynamics, we next asked whether another IAC protein, zyxin, is incorporated into GEMs. We employed zyxin-KO MEFs[22] rescued with Halo7-tagged zyxin, expressed at near-endogenous levels (Figures S1D-S1F). Halo7-zyxin also formed clusters on the apical PM (Figure S1G; Video S1), and ≈70% of talin clusters colocalized with zyxin clusters (Figures 2A and 2B), indicating that zyxin is a major constituent of GEMs. Accordingly, we identify GEMs as clusters detected by talin or zyxin imaging, and report the mean of metrics obtained from talin-defined and zyxin-defined GEMs in the main text (and thus these values differ slightly in the raw data shown in individual figures).

A cluster-lifetime analysis revealed two lifetime components of GEMs: 22% short-lived (0.95 s) and 78% longer-lived (8.5 s) (Figure 2C). In contrast, clusters lacking one partner, talin-only or zyxin-only clusters (hereafter "incomplete GEMs"), showed only a single short lifetime component (≈1.1 s) (Figure S2A). The longer-lived component was observed only when both talin and zyxin were present (after rescue with zyxin or talin), accounting for 78% of talin- or zyxin-containing GEMs (Figure S2A), consistent with their ≈70% colocalization. Thus talin-zyxin co-clusters are substantially more stable than incomplete GEMs.

A copy-number analysis showed broad stoichiometries for both talin and zyxin (1 to ≥20 molecules; medians 4.0 and 4.8, respectively), in contrast to the monomeric farnesylated Halo7 control (Halo7-far; median 1.0) (Figure 2D). No correlation was observed between talin and zyxin copy numbers in individual GEMs (Figures 2E and S2B).

During the 8.5-s lifetime of GEMs, individual talin and zyxin molecules in GEMs rapidly exchange with their cytoplasmic pools, repeatedly entering and leaving GEMs, with dwell lifetimes in the GEM of 2.1 and 1.4 s, respectively (Figures 2F and S2D). This rapid exchange, together with highly heterogeneous stoichiometry (Figures 2E and S2B), is consistent with the notion that GEMs possess liquid-like properties.

The mean GEM density on the apical PM was ≈0.26 clusters/μm^2 (Figure 2G), comparable to clathrin-coated structures on the apical PM,[23] suggesting the presence of

several hundred GEMs per cell. Stimulation of CD59 or PDGFR did not alter the talin copy number per GEM or the GEM density (Figures 2G and S2C).

Partial actin depolymerization with latrunculin A and cytochalasin D, as well as myosin deactivation with the ROCK inhibitor Y27632, significantly reduced both GEM size (talin copy number per cluster) and GEM density on the apical PM (Figures 2D and 2G). These results suggest that the actin-myosin system[24] contributes to GEM formation and/or association with the PM.

To summarize, these data indicate that GEMs are abundant, short-lived talin–zyxin co-assemblies that exhibit heterogeneous stoichiometry and rapid molecular exchange, features consistent with metastable, liquid-like membrane hubs supported by the actin–myosin system.

GEMs are colocalized with integrin, RIAM, VASP, α-actinin, filamin, and FAK, but not with vinculin or paxillin

We next examined the possibility that some other IAC-related proteins are incorporated into GEMs. Single-molecule colocalization analyses revealed that, in resting T24-T cells, β3 integrin, RIAM, VASP, α-actinin, filamin, and FAK colocalize with GEMs, whereas vinculin and paxillin, two major components of IACs, showed little or no detectable colocalization with GEMs (Figures 2H and S2E). Combined with the high abundance of GEMs on the apical PM (and later, also on the basal PM), these observations indicate that GEMs are distinct from classical IACs.

Upon PDGF stimulation, the single-molecule colocalization indexes of RIAM, VASP, zyxin, α-actinin and filamin with GEMs were unchanged, whereas those for integrin and FAK increased. Furthermore, paxillin and N-WASP, but not vinculin, became detectably colocalized with GEMs only after PDGF stimulation (Figure 2H). In the following subsections, we focus on integrin, talin, RIAM, VASP, and zyxin as core GEM constituents that are shared with, yet compositionally and spatially distinct from, classical IACs.

Essential roles of PM raft domains and PI(4,5)P_2 in GEM formation

Because GEMs recruit the GPI-anchored receptors CD59 and Thy1, prototypical raft-associated molecules,[25–27] we next investigated whether GEMs are associated with raft-like PM domains. Single-molecule colocalization analyses revealed that protein probes for cholesterol (D4H[28] for both outer and inner leaflets), sphingomyelin (OlyA-E69A[29] for the

outer leaflet), and phosphatidylserine (the PH domain of evectin2[30,31] for the inner leaflet) were enriched at GEMs, both before and after PDGF stimulation, to similar extents (Figures 2I, S3A, and 3B).

255 Perturbing raft integrity markedly affected GEMs: partial cholesterol depletion reduced both GEM number density and cluster size (talin copy number per cluster) on the apical PM, and the subsequent cholesterol repletion restored them (Figures 2J, 2K, and S3C).

Because the GEM-constituent molecules talin, RIAM, and FAK can bind PI(4,5)P_2 (Figure S2E), we examined whether GEMs and PI(4,5)P_2 colocalize. Single-molecule 260 colocalization analyses showed that PI(4,5)P_2 and its biosynthetic enzyme PI5K[32] are enriched at GEMs both before and after PDGF stimulation (Figures 2I, S3A, and S3B; Video S4). Partial PI(4,5)P_2 depletion from the PM, achieved either optogenetically using the CIBN-CRY2 system[33] or chemically[34], reduced both the GEM number density and cluster size on the apical PM (Figures 2J, 2K, and S3D-S3J).

265 Importantly, the depletion of cholesterol or PI(4,5)P_2 from the PM reduces not only GEM abundance on the apical PM but also the GEM cluster size (Figures 2J and 2K). These results indicate that raft domains and PI(4,5)P_2 would contribute to GEM assembly at the PM, rather than merely tethering pre-formed GEMs to the PM, consistent with a model in which PI(4,5)P_2-associated or enriched raft nanodomains provide a prewet membrane 270 surface that promotes GEM formation.[35–38]

GEM is a nanoscale structure with a diameter of ≈34 nm

To directly determine the physical size of GEMs, we performed super-resolution photoactivated localization microscopy (PALM) imaging[39–41] of mEos3.2-tagged talin and 275 zyxin on the apical PM of fixed cells (Figures 2L and S4A-S4E). The PALM analysis resolved GEMs as discrete clusters containing mean copy numbers of 6.1 talin and 8.2 zyxin molecules, with a median diameter of 40.0 nm (Figures S4F and S4G). These copy numbers per cluster were slightly higher than those evaluated by the live-cell single-molecule intensity analysis (Figure 2D), probably because the PALM tessellation analysis does not detect clusters 280 containing fewer than three molecules.

GEMs occupied the apical PM at a mean density of 0.35 clusters/μm^2 (Figure S4H), reasonably consistent, given the different quantification methods, with the 0.26 clusters/μm^2 measured by live-cell single-molecule imaging (Figure 2G). A monomeric control molecule, farnesylated mEos3.2 (mEos3.2-far), did not exhibit any sign of clustering (Figure S4H).

285 On the *basal* PM, talin-identified and zyxin-identified GEMs with a median diameter of 28.5 nm were detected (Figure S4F) outside obvious classical/conventional IACs (see the bottom-middle panel in Figure 2L). Taking the arithmetic mean of the median diameters measured on the apical and basal PMs, we estimate the characteristic GEM diameter to be ≈34 nm, as a representative value across the two membrane contexts.

290

Zyxin and VASP show intrinsic capacities to undergo LLPS

GEMs exhibit liquid-like features, including a wide-range of molecular composition stoichiometries (Figures 2E and S2B), short lifetimes, and rapid molecular exchange (Figures 2C and 2F). These properties are frequently implicated in condensates generated through 295 liquid-liquid phase separation (LLPS). Furthermore, zyxin, VASP, and RIAM, the main structural constituents of GEMs, contain long intrinsically disordered regions (IDRs; Supplementary Note S1),[42] which are frequently involved in LLPS.[43,44] Various RTK cytoplasmic tails also contain IDRs (e.g., an 88-aa IDR in PDGFR). Although GEMs are nanoscale assemblies, rather than conventional micron-scale LLPS condensates, LLPS-like 300 behavior at the nanoscale has been reported.[45–50] Furthermore, GEM formation depends on raft domains and PI(4,5)P_2 (Figures 2I-2K), features consistent with the idea that LLPS can be enhanced on the membrane surface. Therefore, we asked whether an LLPS-like process underlies GEM formation,[42] potentially aided by raft nanodomains, PI(4,5)P_2, and the cortical actin meshwork, which could provide a permissive environment for LLPS-driven 305 condensation of IDR-containing proteins.[35,37,38,51]

We first tested the intrinsic LLPS capacities of zyxin and VASP *in vitro*. Purified mCherry-zyxin and mGFP-VASP, at concentrations of 2.5-7.5 μM, formed micron-scale condensates, alone and in combination, in the presence of 1% (w/w) polyethyleneglycol (PEG) (Figures 3A and S5A). These condensates exhibited liquid-hydrogel-like FRAP behavior (Figures 3B 310 top, 3C top, S5B, and S5C) and were sensitive to 1,6-hexanediol (Figure 3A), consistent with LLPS.

To further examine whether zyxin's IDRs can drive condensation, we performed coarse-grained (CG) molecular dynamics simulations of a partial zyxin chain (IDR2, Figures 3D and 3E; Video S5). The simulations revealed temperature-dependent condensate 315 formation by IDR2 (Figures S5D-5F). Contact analysis indicated that π-π and cation-π interactions, primarily involving Phe, Tyr, Trp, and Arg residues, play key roles in condensate formation (Figure 3F), consistent with a model in which aromatic and positively charged

residues provide dominant interaction motifs stabilizing IDR2 condensates.[52]

We next asked whether zyxin and VASP can form condensates in cells. Under overexpression conditions in T24 cells, both zyxin and VASP formed micron-scale, liquid-like condensates (Figures 3B bottom, 3C bottom, S5G-S5I). Estimated cytoplasmic concentrations were ≈13 μM (zyxin) and ≈15 μM (VASP), compared with endogenous 0.73 and 0.63 μM (3.11 and 0.25 μM in a MEF line, respectively; Figures 3G, S5J-S5L). In contrast, over-expressed RIAM failed to form detectable micron-scale condensates, even at a higher intracellular concentration (≈18.4 μM, Figures 3H and S5J).

These results obtained *in vitro*, in silico, and in cells under overexpression conditions demonstrate that zyxin and VASP possess intrinsic capacities to undergo LLPS, whereas RIAM does not. The LLPS capability of VASP is consistent with previous reports.[53,54] These properties provide a physical basis for how zyxin and VASP could drive the formation of nanoscale, liquid-like assemblies at physiological expression levels.

In cells, under physiological expression conditions, zyxin and VASP form nanoscale liquid-like assemblies rather than micron-scale condensates

Although zyxin at endogenous concentrations forms micron-scale condensates *in vitro* in the presence of 1% PEG, zyxin expressed at endogenous levels does not form micron-scale condensates in living cells (Figures 3I and 3J). Instead, zyxin expressed at endogenous levels in cells assembles into *nanoscale* structures corresponding to GEMs (Figure 3K), which undergo dynamic merging and splitting (Figure 3K; see also Figure S5M for talin-identified GEMs). Furthermore, as found in talin-identified GEMs, zyxin-identified GEMs decrease in both size and number density on the apical PM upon treatment with 1,6-hexanediol (Figures 2D and 2G), exhibit rapid subsecond-to-second exchange of both recruited signaling molecules and zyxin with the cytoplasmic pools (Figures 1D, 1H, and S2D; see also Figure 2F for talin-identified GEMs), and show highly flexible stoichiometries of talin and zyxin copy numbers (Figure S2B; see also Figure 2E). Collectively, these behaviors suggest that GEMs possess liquid-like properties. We therefore describe the GEM formation process (by LLPS-capable proteins at endogenous concentrations) as an "LLPS-like process" defined here as a nanoscale liquid-like co-assembly process driven by multivalent, weak but specific interactions in cells, analogous in physical principle to micron-scale LLPS.[48,55] Submicron-scale condensates of LLPS-capable proteins under subsaturation concentrations have been reported both *in vitro* and in cells,[45–47,49] whereas nanoscale condensates as small as GEMs,

with clearly defined signaling functions, remain poorly characterized.

While signal-induced, large, micron-scale, long-lived, LLPS-driven signaling assemblies have been reported in *in vitro* systems containing very high protein concentrations or in cells overexpressing relevant molecules,[56–59] those structures differ from GEMs in spatiotemporal scales and formation regime. GEMs are substantially smaller (≈34 nm) and short-lived (≈8.5 s), form at physiological expression levels in cells, and exist constitutively in cells even before stimulation.

Zyxin's IDR is critical for GEM formation through LLPS-like processes

We hypothesized that zyxin IDRs, particularly IDR2, are major driving elements for GEM assembly (Figure 4A), given that talin lacks IDRs (Supplementary Note S1), RIAM does not form condensates in cells (Figures 3H and S5G), and endogenous VASP is expressed at substantially lower levels than zyxin (Figure 3G).

First, the isolated zyxin IDR2 forms submicron-scale condensates *in vitro* at 3 μM in the presence of 1% PEG, similar to the full-length zyxin, whereas the ΔIDR2 construct does not (Figure 4B).

Second, in T24-T cells, zyxin IDR constructs exhibited significantly higher colocalization with GEMs than their IDR-deleted counterparts (Figure 4C). A similar trend was observed for VASP constructs (Figures 4A and 4C).

Third, in five independent zyxin-KO MEF cell lines rescued with physiological levels of partial and full-length zyxin constructs (Figure 4D), confocal imaging of basal optical sections revealed that full-length zyxin, ΔIDR1-2, and ΔIDR2 localize to IACs and diffusely in the basal PM region, whereas IDR1-2 and IDR2 showed no detectable localization at IACs (Figure 4E). These results are consistent with single-molecule colocalization analyses showing the preferential association of IDR-containing zyxin constructs with GEMs on the PM (Figure 4C). Thus, zyxin's IDR1-2 and IDR2 are selectively incorporated into GEMs, but not into IACs.

Fourth, in zyxin-KO MEFs, expressed IDR2 forms nanoscale, liquid-like assemblies in the GEM size range that undergo merging and splitting (Figure 4F), similar to complete GEMs (Figure 3K), although they contain approximately half the copy number of full-length zyxin per GEM cluster (Figure 4G). Nevertheless, IDR2 rescue produced significantly larger clusters than ΔIDR rescue (Figure 4G). These results suggest that IDR2 might be a major driver of LLPS-like processes and liquid-like properties of GEMs.

Finally, rescue experiments using phospho-deficient and -mimetic zyxin mutants
385 indicated that phosphorylation lowers zyxin's ability to colocalize with or form GEMs (Figure 4C-E and G).

Taken together, these findings demonstrate that zyxin's IDR2 is necessary for GEM formation through LLPS-like processes. Moreover, in zyxin-KO cells, where other endogenous GEM components are present, zyxin's IDR2 is sufficient to drive the condensation step that
390 yields nanoscale, liquid-like clusters corresponding to GEMs. These results also indicate that IDR2 is a main cause of GEM liquidity. Importantly, zyxin's IDR2 preferentially partitions into GEMs rather than IACs (Figures 4C, 4E, and 4G). This selective GEM-rescue strategy using IDR constructs, particularly IDR2, was used extensively in subsequent experiments.

395 **GEMs recruit growth and survival signaling molecules**

We next examined whether GEMs recruit downstream cytoplasmic signaling proteins implicated in growth signaling. After PDGF stimulation, the single-molecule colocalization index analysis showed recruitment of PLCγ1 to GEMs (Figure 5A), with a dwell lifetime of ≈80 ms (Figure 1H). FAK was detectably colocalized with GEMs even before stimulation,
400 and its colocalization was strongly enhanced upon PDGF stimulation (Figure 5A) with a sub-second dwell lifetime of ≈200 ms (Figures 5B and 5C; Video S4).

These results indicate that GEMs intermittently and repetitively recruit PLCγ1 and FAK molecules, one molecule after another, resulting in multiple sequential recruitment events. This intermittent, serial recruitment mirrors the subsecond-to-second dwell behavior
405 observed for engaged receptors and core GEM constituents (Figures 1D, 2F, S1M, and S2D).

What signaling output can occur during such brief residence of a single signaling molecule at GEMs? For PLCγ1 (mean dwell ≈80 ms; Figure 1H), the reported maximal catalytic turnover rate (≈230/s)[60,61] provides an upper-bound estimate that each recruited PLCγ1 molecule could hydrolyze ≈20 PI(4,5)P_2 molecules enriched at GEMs (Figure 2I),
410 thereby generating ≈20 IP_3 molecules within ≈80 ms. Because multiple PLCγ1 molecules are repeatedly recruited to GEMs, GEMs are expected to generate frequent IP_3 bursts. The temporal summation of these burst sequences would drive robust Ca^{2+} mobilization.

Single-molecule colocalization further revealed that Lyn (an SFK; hereafter, SFK for general discussion and Lyn for this particular kinase), PI3K, and Akt, prototypical kinases
415 involved in cell survival and growth, were also recruited to GEMs after PDGF stimulation (Figure 5A). PI3K is localized at GEMs even before stimulation, and its colocalization was

enhanced upon PDGF stimulation (Figure 5A). Among these kinases, Akt activation is strongly associated with cell-survival signaling.[62] In contrast, JAK1 did not show detectable colocalization with GEMs either before or after PDGF stimulation (Figure 5A right). Taken together, these results indicate that GEMs function as hubs that preferentially recruit multiple receptors and downstream signaling molecules involved in cell growth and survival (Figure 5D).

PLCγ1 recruitment to GEMs was also triggered by the activation of another RTK, EGFR, and by the stimulation of another GPI-anchored receptor, Thy1 (Figure 5E). These results suggest that GEM-associated PLCγ1 recruitment can be induced downstream of multiple RTKs and GPI-anchored receptors.

Mechanistically, PLCγ1 recruitment to GEMs after PDGFR or CD59 stimulation was markedly suppressed by the inhibition of either FAK or SFK, and was nearly abolished when both kinases were inhibited (Figure 5F). These findings suggest that PLCγ1 is recruited to proteins that are tyrosine-phosphorylated by FAK and/or SFK at GEMs, including FAK and SFK themselves and other GEM-associated substrates.

Because PLCγ is known to be directly recruited to activated/phosphorylated RTKs, we quantified the relative contributions of GEM-dependent versus GEM-independent pathways to PLCγ1 recruitment to the apical PM after PDGF stimulation. Approximately 35% of PLCγ1 molecules arriving at the apical PM colocalized with GEMs in a FAK/SFK-dependent manner, whereas ≈65% localized outside GEMs (Figure 5G), consistent with direct binding to activated RTKs reported previously.[1] Thus, PLCγ1 likely reaches the PM through two parallel routes: (1) direct binding to activated RTKs outside GEMs (≈65%), and (2) binding to GEM-localized proteins tyrosine-phosphorylated by activated PDGFR, FAK, and/or SFK (≈35%).

In zyxin-KO cells, where complete GEMs are depleted, Ca^{2+} mobilization upon PDGF stimulation was markedly reduced and restored by the re-expression of full-length zyxin. Importantly, Ca^{2+} mobilization was partially rescued by the expression of IDR1-2 or IDR2, but not by the ΔIDR1-2 or ΔIDR2 construct (Figure 5H). PDGF-induced Akt activation was similarly impaired in zyxin-KO cells and rescued by the expression of IDR1-2 or IDR2, but not by the ΔIDR constructs (Figure 5I).

These results show that zyxin IDR-driven GEMs are required for the efficient activation of these signaling pathways. Moreover, the selective rescue by zyxin IDR constructs point to an important contribution of GEM's liquid-like organization to signaling, including the capacity to dynamically recruit RTKs, GPI-anchored receptors, and diverse downstream

450 signaling molecules.

GEMs enhance CD59-mediated immune evasion and cell growth

To examine the involvement of GEMs in CD59-mediated immune evasion, we generated a zyxin-KO MEF line in which CD59 expression was reduced to ≈15% of parental levels (Figure
455 5J). Upon rescue with full-length zyxin, MAC precursors were transiently and intermittently recruited to GEMs, as observed in T24-T cells, even at reduced CD59 expression. Furthermore, the presence of CD59 prolonged MAC-precursor dwell lifetimes at GEMs (Figures 5K and 5L). Accordingly, GEMs increase the local opportunity for CD59–MAC precursor binding and prolong MAC precursor residence at GEMs.

460 We next examined whether GEMs enhance CD59-mediated cell protection from CDC, using cell-lysis assays (Figure 5M). Zyxin-KO MEFs rescued with full-length zyxin exhibited a ≈1.5-fold increase in the IC_{50} for non-heat-inactivated serum (Figure 5M). Rescue with full-length zyxin or IDR2, but not with ΔIDR2, significantly enhanced the CDC resistance compared with non-rescued cells (Figure 5N). The CDC protection was abolished in CD59-
465 knockdown cells, regardless of zyxin rescue (Figure 5N), confirming CD59 dependence. Importantly, cholesterol depletion, which reduces GEM number and size despite the presence of all GEM protein components, markedly diminished CD59-mediated CDC protection, and the subsequent cholesterol repletion restored it (Figure 5O). These results link raft-domain-dependent GEM integrity (number/size) to CD59-mediated immune evasion.

470 Rescue with full-length zyxin or IDR2, but not with ΔIDR2, also enhanced MAC-precursor-induced, CD59-dependent cell proliferation (Figure 5P and STAR Methods), in line with the recruitment of PLCγ1, a signaling molecule involved in cell growth, to CD59-resident GEMs (Figures 1G-1I) and with our previous results.[4,5] Thus, CD59 signaling at GEMs contributes not only to CDC resistance but also to proliferative signaling (Figures 1L and 5D).

475 Because zyxin IDR1-2 and IDR2 do not localize to IACs (Figure 4E), the functional recoveries observed here (Figures 5H, 5I, and 5N-5P) can be attributed to the restoration of GEMs rather than IACs. Together, these data show that GEMs greatly enhance both CD59-dependent immune evasion via CDC resistance and growth signaling, probably by confining signaling molecules within a nanoscale liquid-like environment, consistent with the
480 requirement for IDR2 in GEM formation.

RTK and CD59 signals are physically integrated and cooperatively amplified at

GEMs

Because CD59 can trigger both CDC resistance and cell-growth signaling, whereas PDGFR is a canonical growth factor receptor, we asked how cells respond to simultaneous CD59 and PDGFR stimulation. We applied concurrent CD59 and PDGFR stimulations to zyxin-KO MEFs rescued with full-length zyxin, IDR2, or ΔIDR2, as well as to non-rescued cells.

In cells rescued with full-length zyxin, under mild, physiologically-relevant stimulation conditions, co-stimulation increased PLCγ1 recruitment to GEMs to ≈6.9-fold above the arithmetic sum of responses to the individual stimulations (Figure 6A, left). This supralinear increase was restricted to GEMs, with no corresponding enhancement detected outside GEMs on the PM (Figure 6A, right). Similar co-stimulation-dependent supralinear responses were observed for Ca^{2+} mobilization (Figures 6B and 6C) and PI3K recruitment to GEMs (Figure 6D). Thus, co-stimulation drives GEM-restricted supralinear amplification of PLCγ1/PI3K recruitment and Ca^{2+} signaling, pointing to cooperative integration of RTK- and CD59-derived inputs at GEMs.

Under mild single stimulations, CD59 preferentially induced FAK recruitment, whereas PDGF preferentially induced Lyn (SFK) recruitment (Figure 6E; note that strong PDGF stimulation induced the recruitment of both FAK and Lyn, as shown in Figure 5A). Supralinear amplification required both kinases: inhibiting either FAK or SFK abolished the enhanced PLCγ1 recruitment and Ca^{2+} mobilization upon co-stimulation (Figures 6A and 6C). These findings indicate a cooperative mechanism in which reciprocal FAK-SFK activation supralinearly increases phosphotyrosine-bearing docking sites in GEMs, thereby boosting the recruitment of PLCγ1 and PI3K (see Figure 5F).[62,63]

Given their nanoscale diameter (≈34 nm) and liquid-like environment, GEMs will increase the encounter frequency between FAK and SFKs, facilitating reciprocal chain phosphorylation (activation),[64–66] a process referred to as a "kinase spiral". To probe this possibility, we performed independent tests using the binder-tag system[67] and the optoDroplet system.[68,69] The results supported a confinement-based mechanism (Figure S6). Thus, these results together position GEMs as nanoscale integrative platforms in which RTK- and CD59-derived inputs are converted into supralinearly amplified PLCγ1-IP_3-Ca^{2+} and PI3K-PI(3,4,5)P_3-Akt outputs that are central to cell survival and growth (Figure 6F).

Importantly, IDR2-rescued GEMs fully restored the co-stimulation-induced cooperative supralinear amplification of PLCγ1 recruitment and Ca^{2+} signaling, whereas ΔIDR2 did not (Figures 6A and 6C), demonstrating that the IDR2-driven liquid-like GEM organization

(Figure 4F) is required for GEM's integrative signaling function under physiological expression and stimulation conditions.

Tumor growth in mice is promoted by GEM, with a requirement for zyxin's IDR2

520 To test whether GEMs contribute to tumor growth *in vivo*, we established a K-RasG12V-driven tumor model using zyxin-KO MEFs. The parental zyxin-KO MEF line, immortalized by serial passaging, did not form solid tumors in mice (Figures 7A and S7A). After K-RasG12V transformation, zyxin-KO MEFs formed solid tumors only slowly in mice (nude mice; BALB/cAJcl-Foxn1nu) after subcutaneous injection, whereas rescue with full-length zyxin 525 produced significantly larger and faster-growing tumors (Figures 7B-7D). IDR2 rescue phenocopied full-length zyxin rescue, whereas ΔIDR2 rescue did not (Figures 7B-7D). Because IDR2 shows minimal incorporation into IACs (Figure 4E), these tumor phenotypes are attributable to the restoration of GEMs, rather than the recovery of IACs. Meanwhile, zyxin-KO MEFs still formed tumors, albeit slowly (Figures 7B-7D), indicating that GEMs are 530 not the sole driver of proliferation. Instead, GEMs provide a substantial quantitative fitness advantage within a redundant pro-survival network *in vivo*.

Tumors derived from full-length zyxin- or IDR2-rescued cells exhibited elevated phosphorylations of FAK and Akt, whereas ΔIDR2-rescued tumors did not (Figure 7E). JAK1 phosphorylation remained uniformly low across all tumors generated from all four rescued 535 cell lines (Figure 7E), consistent with the lack of detectable JAK1 recruitment to GEMs in cultured cells (Figure 5A). Together, these findings indicate that GEM-linked FAK-SFK signaling and PI3K-Akt activation, defined in cultured cells (Figure 5A), are also engaged in tumor growth *in vivo*.

To examine generality beyond MEFs, we generated zyxin-KO clones in the human 540 cancer cell lines RKO (colon) and MDA-MB231 (breast) and re-expressed endogenous levels of full-length zyxin, IDR2, or ΔIDR2 (Figure S7B). Both the *in vitro* proliferation (Figure S7C) and tumor growth in mice (RKO; Figures S7D-S7F) showed the same IDR2 dependence as in MEFs, supporting a broad requirement for zyxin's IDR2, and thereby IDR2-dependent GEM formation, for efficient tumor growth.

545 Because nude mice lack T cells but retain intact innate immunity, including complement,[70] CD59 on grafted cells can be activated by MAC precursors *in vivo*. To assess the contributions of CD59-mediated immune evasion and proliferative signaling *in vivo*, we employed the four transformed MEF rescue lines and reduced CD59 expression by ≈85%,

using CD59 shRNA (Figure 5J). An *in vivo* analysis showed that functional GEMs (full-length
550 zyxin or IDR2 rescue) support tumor growth even with ≈85% CD59 knockdown, whereas CD59 expression further accelerates tumor progression (Figures 7F-7H), consistent with combined contributions of CD59-dependent proliferative signaling and complement evasion.

The GEM-driven, CD59-independent growth signaling *in vivo* is likely mediated in part by RTK-linked Akt activation: *in vivo*, Akt phosphorylation is elevated in GEM-competent
555 tumors (Figure 7E), and in cultured cells, Akt is recruited to GEMs upon PDGF stimulation, but not upon CD59 stimulation (Figures 5A and S7G), suggesting that RTK-dependent Akt activation is amplified, at least in part, via GEMs.

As control experiments, we examined whether CD59 knockdown affects the proliferation of the four MEF lines under standard *in vitro* culture conditions, where the
560 complement activity is eliminated by heat-inactivation. The CD59 knockdown had no detectable effect on the proliferation of any of the four MEF lines (Figure S7H), indicating that the CD59-dependent effects become biologically relevant specifically *in vivo*, where complement is active.

In conclusion, these findings demonstrate that GEMs are major contributors to tumor
565 growth in mice, boosting growth-factor signaling and CD59-associated *in vivo* advantages. The recurring requirement for zyxin IDR2 across tumor models connects these *in vivo* phenotypes to an IDR2-dependent, liquid-like GEM organization characterized *in silico* and in cultured cells (Figures 3D-3F, 3K, and 4F).

570

DISCUSSION

In this study, we demonstrate that growth signaling and CD59-mediated immune-evasion signaling, long treated as independent cellular programs, can be physically coupled at the PM by a dedicated nanoscale structure. Using super-resolution single-molecule imaging, we identify GEM (Growth and Evasion Metastable hub) as a previously unrecognized, nanoscale, (≈34 nm), metastable (8.5-s lifetime), liquid-like signaling platform on the PM that physically integrates RTK and CD59 inputs within the same nanoscale assembly and supports cooperative, supralinear amplification of survival signaling, including PLCγ1/PI3K recruitment and Ca^{2+}/Akt signaling. GEM assembles constitutively at endogenous protein levels through LLPS-like interactions driven primarily by zyxin's IDR2. In addition, GEM contributes to CD59-mediated immune evasion via CDC resistance.

A defining feature of GEM is its nanoscale liquidity. Unlike previously described LLPS-driven signaling condensates, which are typically micron-scale and often require overexpression or non-physiological concentrations *in vitro*.[56–59] GEM forms constitutively at endogenous protein levels and remains confined to the tens-of-nanometer length scales. It is also distinct from stable micron-scale signaling structures observed in specialized contexts (e.g., neuronal and immune synapses,[71–73] and septin-stabilized blebs,[74]), and becomes apparent only through single-molecule imaging capable of detecting individual recruited molecules and GEM clusters composed of as few as 2–20 constituents, as observed in the present study. Importantly, GEM's short lifetime (≈8.5 s) and the sub-second dwell lifetimes of recruited signaling molecules (0.1–0.4 s) ensure rapid and reliable signal termination.[48]

These physical characteristics plausibly provide the basis for GEMs' unique ability to cooperatively integrate the concurrent RTK and CD59 inputs. We propose that repeated encounters between FAK and SFKs by nanoconfinement within liquid-like GEM enhance reciprocal chain activation, a process we term a "kinase spiral" (Figure 6F). This kinase spiral can, in turn, drive supralinear amplification of downstream PI3K-PI(3,4,5)P_3-Akt and PLCγ-IP_3-Ca^{2+} outputs, pathways central to cell survival and proliferation.

GEM also enhances CD59's two key functions: immune evasion via CDC resistance by co-recruiting CD59 and MAC precursors (Figures 1J, 1K, 5K-5O) and CD59-dependent cell-growth signaling (Figure 5P). Collectively, these results provide a mechanistic basis for the coupling of growth signaling and CDC resistance signaling, previously considered separate processes, at the PM that promotes cell survival and tumor growth *in vivo*.

More generally, confining signaling components within a liquid nanoscale volume can

dramatically increase encounter frequencies, enabling cooperative, supralinear signal amplification beyond what is achievable by classical solid scaffolds[75] or diffusion-limited cytoplasmic signaling.[48] A related precedent is FcεRI phosphorylation by Lyn in raft nanodomains induced by receptor oligomerization.[76]

GEM formation is enhanced by raft domains, PI(4,5)P_2, and cortical actin filaments (Figures 2D, 2G, 2I-2K, and S3). Talin and RIAM can bind to PI(4,5)P_2 associated with raft domains, and might be activated by lipid-binding.[77] Both RIAM and folded talin directly bind PI(4,5)P_2-rich membranes, allowing them to co-assemble at low-tension cortical sites before any force-driven talin unfolding or adhesion maturation.[78–81] In this pre-mechanochemical regime, integrins typically reside in ligand-engaged or preactivated, but not fully tension-activated, states that support receptor-proximal signaling without triggering vinculin recruitment or IAC growth.[82,83] Our results suggest that GEM selectively captures this PI(4,5)P_2-dependent, low-force configuration as a biochemical pre-assembly step for GEM formation.

Importantly, this arrangement might create a prewet membrane surface that favors zyxin/VASP recruitment and condensation[35–38], converting the RIAM–talin precomplex into the nanoscale liquid-like scaffold characteristic of GEM. In this way, GEM leverages only the tension-independent initiation module of the adhesion machinery and repurposes it to seed a zyxin/VASP-based nano-liquid hub dedicated to signal integration, rather than mechanical anchoring. The cortical actin meshwork may further help establish a prewet surface for recruiting talin and VASP for GEM assembly.

From an evolutionary perspective, phylogenetic analyses suggest that many IAC components originated as ancient signaling scaffolds before being co-opted for force transmission,[84,85] although talin might also have played a central role in the evolution of cell adhesion and force transmission.[86] GEM might thus preserve a primordial signaling function of these scaffolds that persists in modern cells alongside their mechanical roles.

LLPS drivers for IAC formation include p130Cas, FAK, paxillin, kindlin, vinculin, talin, and integrin tails,[55,77,87] but zyxin's IDRs are largely excluded from mature IACs, whereas the dominant GEM driver is zyxin's IDR2 (Figure 4E). These findings underscore that distinct molecular grammars underlie different condensate types within the same protein network. However, given the overlap in components between GEMs and IACs, specific IAC states might exhibit signaling functions under certain mechanical and compositional regimes.

GEM also differs fundamentally from previously described aster structures or GPI-

anchored protein nanoclusters, which are typically larger (>500-nm structures) and depend on integrin force-induced activation, vinculin engagement, and/or overexpression of GPI-anchored proteins.[15,88,89] Nor does GEM conform to classical scaffold models composed of a small number of adaptor proteins or solid-like assemblies.[75,90] Instead, GEM operates as a nano-liquid reactor, in which rapid molecular exchanges and high encounter frequencies dramatically accelerate reaction kinetics.

The physiological relevance of GEM-based signal integration is supported by our *in vivo* data. Consistent with the IDR2-dependent nano-liquid organization characterized *in silico* and in cultured cells, restoration of GEM through the zyxin IDR2 rescues tumor growth in multiple mouse models and human cancer cell lines (Figures 7 and S7). GEM is required for tumor growth even without CD59, whereas CD59 further enhances this effect via immune evasion (CDC resistance) and CD59-dependent growth signaling (Figures 7F-7H and S7G). Importantly, zyxin-KO MEFs still formed tumors, albeit slowly (Figures 7B-7D), indicating that GEM is not an exclusive driver of proliferation in a redundant pro-survival network. Together, these observations support that GEM acts as a quantitative amplifier that confers a substantial fitness advantage *in vivo*, where complement remains active.

Many GEM components, including CD59, integrin, talin, VASP, and zyxin, are overexpressed in diverse cancers,[91–99] suggesting that the up-regulation of a nano-liquid signaling infrastructure might be a general strategy for tumor survival under immune pressure. With the growing recognition of LLPS in cancer biology,[100,101] GEM highlights a previously unappreciated dimension: liquid condensates operating at the nanoscale, rather than micron-scale, can dominate signaling outcomes *in vivo*.

In summary, this work establishes GEM as a nano-liquid signaling hub that integrates the growth and CD59-mediated immune-evasion pathway through confinement-enhanced, cooperative kinase activation. By extending LLPS concepts from large micron-scale condensates to metastable nanoscale hubs, our findings reveal a previously unappreciated layer of cellular organization that governs cell survival signaling *in vivo*. Similar structures may operate across many signaling systems, and uncovering them will require single-molecule approaches capable of resolving dynamics at the molecular scale.

LIMITATIONS OF THE STUDY

Our data support GEM as a nano-liquid signaling platform at the PM that integrates growth signaling and CD59-associated immune evasion at the PM. We focused on CD59-mediated

670 resistance to CDC as a tractable and physiologically relevant immune pressure; whether GEM similarly contributes to other immune-evasion signaling pathways remains to be determined.

Several mechanistic issues remain. These include how receptors are recruited and transiently retained at GEMs, how integrin/talin activation states are configured, and how 675 GEMs relate to adhesion structures on the basal membrane.

First, the molecular mechanisms underlying receptor recruitment and transient immobilization at GEMs remain unresolved. Because CD59, as a GPI-anchored protein, cannot directly bind cytoplasmic GEM components, it might couple indirectly via integrins[12–15,102,103] and other GEM-localized transmembrane proteins and/or via raft-mediated 680 transbilayer coupling.[6,104,105] Likewise, RTKs might be recruited through integrin-mediated interactions[9,10,106] and/or by preferential partitioning of their IDR-rich cytoplasmic domains into the nano-liquid GEM environment.

Second, we have not resolved the activation states of the integrin[83] or talin[107] in GEMs. Although our data indicate that GEM formation is independent of force-induced adhesion 685 maturation, integrin's conformational states and talin autoinhibition may still modulate GEM assembly or signaling efficiency. Future studies combining tension sensors with single-molecule tracking will be required to map integrin conformation/talin autoinhibition and determine how force-free versus force-bearing regimes intersect at the level of GEMs.

Third, because many GEM components also participate in IACs, the GEMs on the basal 690 PM might, in principle, transition into IACs and/or IAC-protein islands,[108] potentially under mechanical stress.[15,109,110] Although multiple studies have suggested LLPS involvement in IAC formation,[53,55,57,63,87,111–118] we found that zyxin's IDR is selectively excluded from mature IACs, implying that GEM's role in adhesion, if any, may be restricted to early, force-independent stages. How GEMs transition, dissolve, or remain segregated during adhesion 695 maturation therefore remains an important open question.

Finally, although our *in vivo* data demonstrate a critical role for GEMs in tumor growth, the extent to which nano-liquid GEM operates in other physiological or pathological contexts remains to be explored. By addressing these issues, we could clarify the generality of nano-liquid signaling hubs and for assessing their potential therapeutic relevance.

RESOURCE AVAILABILITY

Lead contact

Further information and requests for resources and reagents should be directed to and will be fulfilled by the Lead Contact Akihiro Kusumi (akihiro.kusumi@oist.jp)

Materials availability

Plasmids generated in this study are available by request from the Lead Contact.

Data and code availability

Data and codes generated in this study are available by request from the Lead Contact.

ACKNOWLEDGMENTS

We thank the researchers who kindly provided us with the cell lines and cDNAs used in this research (details are given in the STAR Methods). We also thank Drs. P. Kanchanawong, S. Liu, and M. Kham of the National University of Singapore for technical help with the mouse embryonic stem cell culture, Drs. P. Barzaghi and B. Humbel of the OIST Imaging Section (IMG) for their help with FRAP experiments, Ms. F. Koja of the OIST Instrumental Analysis Section (IAS) for supporting FACS experiments, the OIST Sequencing Section (SQC) for their help in performing DNA sequencing, the OIST Animal Resource Section (ARS) for their help in animal care, and Dr. K. Simons of Lipotype GmbH, Dr. S. Mayor of National Centre for Biological Sciences, and all members of the Kusumi laboratory for valuable discussions. This work was supported in part by Japan Society for the Promotion of Science (JSPS) Grants-in-Aid for Scientific Research (Kiban A to A.K. [21H04772], Kiban S to A.K. [16H06386], Kiban B to T.K.F. [20H02585 and 24K01310], Kiban C to R.S.K. [17K07333], Wakate B to R.S.K. [26870292], Wakate to T.A.T. [21K15058 and 25K18434], Kiban B to H.I. [23K27326], and Challenging Exploratory Research to T.K.F. [18K19001]), a Grant-in-Aid for Innovative Areas to K.G.N.S. [18H04671] and Grants-in-Aid for Transformative Research Areas (A) to T.K.F. [21H05252] and R.S.K. [23H04414] from the Ministry of Education, Culture, Sports, Science and Technology of the Japanese Government (MEXT), a Japan Science and Technology Agency (JST) grant in the program of the Core Research for Evolutional Science and Technology (CREST) in the field of "Biodynamics" to A.K. and that in the field of

"Extracellular Fine Particles" and "Cell Control" to K.G.N.S. [JPMJCR18H2 and JPMJCR24B3], and a JST grant ACT-X to T.A.T. [JPMJAX211B]. WPI-iCeMS of Kyoto University is supported by the World Premiere Research Center Initiative (WPI) of MEXT. D.M. is supported by start-up funds from DZNE, grants from the German Research Foundation [SFB 1286/B10 and MI 2104], an ERC Grant [101078172], and the Human Frontier Science Organization [RGEC32/2023]. C.H. is supported by a fellowship of the Innovative Minds Program of the German Dementia Association.

AUTHOR CONTRIBUTIONS

T.A.T. performed large majorities of the single-fluorescent-molecule imaging, biochemical, and molecular biology experiments and analyses. T.A.T., T.K.F., and A.K. developed the single-molecule imaging camera system, set up single-molecule imaging stations, and developed the analysis software. T.A.T., K.G.N.S., and A.K. established single-molecule observation conditions for CD59 and PDGFR signaling cascades. C.H. and D.M. purified zyxin and VASP and, together with T.A.T., performed LLPS and FRAP experiments. B.T. generated protein probes for cholesterol and sphingomyelin. T.A.T., D.S., and H.I. designed and performed the animal experiments and analyzed the data. C.T. and Y.S. performed coarse-grained molecular dynamics simulations. T.A.T., C.H., D.S., Y.L.N., K.M.H., R.S.K., T.K.F., K.G.N.S., H.I., D.M., and A.K. participated in discussions throughout the course of this research. T.A.T. and A.K. conceived and formulated this project, and evaluated and discussed the data. T.A.T. and A.K. wrote the manuscript and all authors participated in its revision.

DECLARATION OF INTERESTS

The authors declare no competing interests.

DECLARATION OF GENERATIVE AI AND AI-ASSISTED TECHNOLOGIES IN THE WRITING PROCESS

The authors used ChatGPT 5.2 (OpenAI) to improve the manuscript's clarity and grammar. The authors reviewed all text to ensure accuracy and take full responsibility for the content of the publication.

MAIN FIGURE TITLES AND LEGENDS

Figure 1. Single-molecule imaging reveals a nanoscale liquid-like signaling hub that recruits CD59 and engaged PDGFR (growth and evasion metastable hub=GEM).

(**A**) Single-molecule visualization of fluorescently labeled talin clusters located on the apical PM.

(**B**) Distributions of talin cluster lifetimes.

(**C and D**) Intermittent, transient recruitment of engaged PDGFR and CD59 (trajectories) to talin clusters (white spots; **C**) and their dwell lifetimes at talin clusters (τ_2; **D**).

(**E**) Single-molecule colocalization indexes of various receptors with talin clusters.

(**F**) Typical images of talin clusters (overexpressed Halo7-talin) in various cell lines.

(**G-I**) Immediately following the recruitment of engaged CD59 clusters to talin clusters, PLCγ1(-Halo7) is recruited to the same talin clusters. (**G**) Representative talin cluster image and trajectories of a PLCγ1 molecule and a CD59 cluster. (**H**) Distribution of the dwell durations of PLCγ1 on talin clusters. (**I**) Timing of PLCγ1 recruitment relative to CD59-cluster recruitment (>3-frame colocalizations).

(**J and K**) Transient recruitment of MAC precursors (trajectory; **J**) to talin clusters (white puncta) and their dwell lifetimes at talin clusters (**K**).

(**L**) Schematic model illustrating that CD59, MAC precursors, and PDGFR are recruited to GEM (growth and evasion metastable hub).

Throughout this study (unless otherwise noted), bars, boxes, and whiskers indicate mean values, interquartile ranges (25–75%), and 10–90% ranges, respectively, and NS, not significant; *, $P < 0.05$; and **, $P < 0.01$.

Brunner-Munzel test for (**D**), two-tailed Welch's t-test for (**E**), Steel-Dwass' test for (**H and K**).

Figure 2. Single molecule tracking and PALM define GEM as a ≈34 nm, nanoscale, liquid-like assembly associated with PI(4,5)P_2 and raft nanodomains.

(**A and B)** Typical dual color images of talin and zyxin clusters (circles, **A**) and their colocalized fractions (**B**).

(**C**) Distributions of the cluster lifetimes.

(**D**) Distributions of the numbers of talin and zyxin molecules residing in GEM.

(**E**) Stoichiometries of talin and zyxin in GEM.

(**F**) Dwell time distributions of single talin molecules in zyxin-containing GEM.

(**G**) Cluster number densities for GEMs on the apical PM (dots for individual cells; bars for mean ± SEM).

(**H**) Single-molecule colocalization indexes of various FA proteins with GEM.

(**I**) Single-molecule colocalization indexes of protein probes for various lipids (Halo7-tagged) with GEM (see Figure S3C for other probes).

(**J and K**) GEM number densities (**J**) and mean talin copy numbers per GEM (**K**; see Figures S3C and S3J for distributions) on the apical PM after the indicated treatments (talin clusters; mean ± SEM).

(**L**) Conventional and PALM super-resolution images (Voronoï diagram) of GEM, visualized by mEos3.2-talin on the apical and basal PMs. The areas surrounded by the green curve (middle image) indicate regions with good focus (top; apical PM, which is tilted) or without obvious focal adhesions (bottom; basal PM) and were used for further analysis. The cyan lines in the right images indicate the smallest polygon enclosing each clustered region.

(**M**) Schematic diagram showing the molecular composition of GEM and the association of GEM with PI(4,5)P_2, raft nanodomains, and cortical actin filaments.

Steel-Dwass' test for (**D** (vs. talin cluster) **and K**), Games-Howell's test for (**G, I, and J**), Two-tailed Welch's t-test for (**H and I**).

820 **Figure 3. Zyxin and VASP can undergo LLPS.**

(**A**) Typical confocal images of *in vitro* co-condensation of purified mCherry-zyxin and mGFP-VASP in the presence of 1% PEG8K.

(**B and C**) Micron-scale co-condensates of mCherry-zyxin and mGFP-VASP formed *in vitro* (**top**; 1% PEG8K) and in cells under overexpression conditions (**bottom**; T24), with FRAP
825 indicating liquid-to-hydrogel-like behavior.

(**D-F**) Coarse-grained MD simulations. (**D**) Domain structure of zyxin. (**E**) Modeling and MD simulations of a single chain and a 200-chain condensate of zyxin IDR2 at 210 K. (**F**) Inter-chain contact analysis of zyxin IDR2 condensates. (**Left**) Inter-chain residue-residue contact probability. (**Top-left**) Number of inter-chain contacts per residue. (**Right**) Type-type
830 contact heatmap normalized by amino acid frequency.

(**G**) Cytoplasmic concentrations of endogenous and tagged zyxin and VASP (mean ± SEM).

(**H**) RIAM does not form detectable micron-scale condensates even at concentrations much higher than endogenous levels (confocal image).

(**I**) *In vitro*, zyxin and VASP form micron-scale co-condensates even at physiological
835 endogenous concentrations in the presence of 1% PEG8K.

(**J**) mGFP-zyxin expressed at endogenous levels in zyxin-KO MEFs does not form detectable micron-scale condensates in cells.

(**K**) Typical images of nanoscale zyxin clusters (GEMs) undergoing dynamic merging and splitting.

840

Figure 4. Zyxin's IDRs facilitate GEM formation.

(**A**) Domain structures of zyxin, VASP, and their mutants employed in this study.

(**B**) Zyxin's IDR2, but not ΔIDR2, forms liquid-like micron-scale condensates *in vitro*.

845 (**C**) Single-molecule colocalization indexes of full-length and partial sequences of zyxin and VASP (± IDRs, Halo7-tagged) with GEM (talin-identified clusters) in T24-T cells.

(**D**) Establishment of rescued zyxin-KO MEF lines expressing full-length and partial sequences of zyxin (± IDRs, mGFP-tagged) at comparable expression levels (mean ± SEM).

(**E**) Typical confocal micrographs near the basal PMs of the rescued zyxin-KO MEF lines

850 shown in **D**.

(**F**) Typical images of nanoscale IDR2 clusters (IDR2-rescued GEM-like assemblies) undergoing merging and splitting.

(**G**) Distributions of the copy numbers of zyxin (WT and mutants) per GEM cluster, determined for the rescued zyxin-KO MEF lines shown in **D**.

855 Two-tailed Welch's t-test and Games-Howell's test for (**C**), one-way ANOVA for (**D**), and Steel-Dwass' test for (**G**).

Figure 5. GEM functions as a signaling platform for both RTK and GPI-anchored receptor signaling pathways.

(**A**) Single-molecule colocalization indexes of the PDGFR downstream signaling molecules (Halo7-tagged) with GEM.

(**B and C**) Typical image showing transient colocalization of Halo7-FAK (trajectories) with GEM (white puncta) after PDGF stimulation (**B**). Distributions of the dwell durations of FAK at GEM before and after PDGF stimulation (**C**).

(**D**) Schematic summarizing receptors and downstream signaling molecules recruited to GEM.

(**E**) Stimulations of RTKs and GPI-anchored receptors induce PLCγ1 recruitment to GEM.

(**F**) Inhibition of either FAK or SFK suppresses PLCγ1 recruitment to GEM after PDGFR stimulation.

(**G**) Fraction of PLCγ1 recruited to GEM vs. non-GEM regions of the apical PM after PDGF stimulation (mean ± SEM).

(**H and I**) IDR expression restores PDGF-induced Ca^{2+} mobilization (fold increase at the peak, **H**) and Akt activation (S473 phosphorylation; mean ± SEM; **I**).

(**J**) Sh-CD59-mediated CD59 knockdown in zyxin-KO MEFs, reducing the CD59 expression to ≈15%. Typical western blot pattern (**top**) and quantification (**bottom**, mean ± SEM).

(**K and L**) Transient recruitment of MAC precursors (trajectory; **K**) to GEM (white puncta) and their dwell lifetime at GEM (**L**).

(**M-O**) CDC assay as a function of serum concentration (mean ± SEM, **M**). The 1.6% normal serum condition (yellow line in **M**) was used for the comparison in **N** and **O** (mean ± SEM) to maximize the dynamic range.

(**P**) Cell growth after stimulation with C9-depleted serum (mean ± SEM).

Two-tailed Welch's t-test for (**A, H**), Games-Howell's test for (**E, F, H, I, and N-P**), one-way ANOVA for (**J and N**), and Brunner-Munzel test for (**L**).

Figure 6. GEM cooperatively integrates CD59 and PDGFR signaling, generating supralinearly amplified outputs.

(**A**) Percent increases in PLCγ1 recruitment frequency to GEM (**left**) and to non-GEM regions of the PM (**right**) after mild individual stimulations and co-stimulation of CD59 and PDGFR, in zyxin-KO MEFs rescued with full-length zyxin, IDR2, and ΔIDR2 (mean ± SEM). Mild stimulation conditions were 20 pM PDGF and 20 nM αCD59-coated beads. Twenty pM PDGF approximates physiological serum levels,[119] and corresponds to 1/1,000 of our standard PDGF stimulation; 20 nM αCD59 beads corresponds to 1/100 of the standard stimulation.

(**B**) Typical Ca^{2+} mobilization time courses in individual cells after mild individual and simultaneous stimulations.

(**C**) Total Ca^{2+} signal (areas under the curve; AUC) (mean ± SEM).

(**D**) Percent increases of the PI3K recruitment frequency to GEM (mean ± SEM).

(**E**) Single-molecule colocalization indexes of Halo7-tagged β3 integrin, FAK, Lyn, and PLCγ1 with GEM (SNAPf-talin clusters) after mild single stimulations and co-stimulations of PDGFR and CD59.

(**F**) Schematic illustrating the kinase spiral model, in which reciprocal FAK-SFK chain activation drives cooperative and supralinear amplification of the GEM outputs upon CD59+PDGFR co-stimulations.

Games-Howell's test for (**A, C, D, and E**) and two-tailed Welch's *t*-test for (**E**).

Figure 7. GEM promotes tumor growth in mice.

(**A**) Schematic of the xenograft workflow.

(**B-D**) Tumor growth of transformed zyxin-KO MEFs is enhanced by GEM restoration. (**B**) Images of excised tumors. (**C**) Tumor growth curves (mean ± SEM). (**D**) Weights of excised tumors at day 29 after cell injection (mean ± SEM).

(**E**) Western blot analysis of FAK, Akt, and JAK1 phosphorylation (pY397, pS473, and pY1034/1035, respectively) in excised tumors (mean ± SEM).

(**F-H**) CD59 dependence of GEM-supported tumor growth. (**F**) Images of excised tumors. (**G**) Tumor growth curves (mean ± SEM). (**H**) Weights of excised tumors.

Games-Howell's test for (**C, D, E, G, and H**), one-way ANOVA for (**E**), and two-tailed Welch's *t*-test for (**H**).

(**I**) Model summarizing GEM organization and function.

(**Top**) GEM (Growth and Evasion Metastable hub) assemblies, mainly consisting of integrins, talin, RIAM, VASP, and zyxin (Figure 2H), existing at a number density of ≈0.26 clusters/μm^2 (Figure 2G). Given that the cortical-actin-induced PM compartment size is ≈100 nm in T24 cells,[120] approximately one GEM is expected per ≈400 compartments. GEMs are ≈34 nm nanoscale, liquid-like protein assemblies (Figure S4F) that constitutively form and disperse with a lifetime of ≈8.5 s on both the apical and basal PMs (outside the IACs) (Figure 2C). Constituent molecules are exchanging rapidly (<2 s; Figures 2H, 5C, and S2C). Liquid-like behavior is consistent with multiple observations, including broad stoichiometries (Figures 2E and S2B), rapid exchange rates (Figures 2H, 5C, and S2C), merging and splitting (Figures 3K and S5M), and the requirement of zyxin's IDR for formation and function (Figures 4 and 5H-P). GEM assembly is enabled by a permissive, prewet membrane environment provided by the actin-based membrane-skeleton meshwork[23,121,122] (Figures 2D and 2G) and PI(4,5)P_2-containing raft nanodomains (Figures 2I-2K, and S3), which together furnish a nanoscale surface that supports condensation and co-assembly.

(**Bottom**) Upon stimulation, engaged GPI-anchored receptors and RTKs are transiently recruited to GEM, which in turn induces further recruitment of receptors' downstream signaling molecules (Figures 1C-1E and 5). Nano-liquid confinement within GEM increases the encounter frequency among recruited molecules within GEM, and interactions would occur extremely efficiently. GEM serves as a hub for CD59-driven proliferative signaling (Figure 5P), consistent with prior work,[4–6] and for CD59-mediated immune evasion by recruiting both CD59 and MAC precursors (C5b-8, Figures 1K and 5L).

Upon co-stimulation of CD59 and RTK, FAK (CD59 pathway) and SFKs (RTK pathway) are co-recruited (Figure 6E), promoting reciprocal chain phosphorylation (kinase spiral; Figures 6F and S6), which induces the supralinear recruitment of PLCγ and PI3K to GEM (Figure 6A and D). Thus, GEM functions as an AND gate (coincidence detector) for CD59 and RTK inputs (Figure 6F). *In vivo*, GEM competence correlates with the elevated activation of FAK and Akt, critical molecules for cell survival and growth (Figure 7E), and is required for robust tumor growth (Figures 7A-7D and 7F-7H).

SUPPLEMENTAL FIGURE TITLES AND LEGENDS

955 **Figure S1. Establishment of talin- and zyxin-rescued MEF lines, detection of talin/zyxin clusters, calculation of single-molecule colocalization index, and establishment of the T24-T cell line, related to Figure 1.**

(**A**) Establishing talin1/2-dKO MEF lines rescued with various tagged talin1 constructs expressed at levels comparable to endogenous talin1 in talin2-KO MEFs (parental cell line
960 for generating talin1/2-dKO MEFs). Western blot quantification of talin1/tagged talin1 expression (mean ± SEM, n = 4 replicates). Since talin1 is the main isoform in most tissues,[123] we employed talin1 rather than talin2. Unless otherwise specified, "talin" refers to talin1 throughout. Because the talin-dKO MEF lines were generated from talin2-KO MEFs (as the parental cell line),[19] the parental talin2-KO line was used as a control; control MEF
965 lines 1-4 are independent immortalized MEF controls.

(**B**) Tagged-talin constructs are functional in fibronectin-dependent attachment (5 min after plating; mean ± SEM, n = 6 dishes).[19]

(**C**) Tagged-talin constructs incorporate into IACs. Confocal immunofluorescence microscopy of rescued dKO MEFs using an anti-talin1 monoclonal antibody (confocal section near the
970 basal PM). The contour of a non-rescued cell is shown in yellow.

(**D-F**) Establishing zyxin-KO MEF lines rescued with various tagged zyxin constructs, expressed at levels comparable to the mean endogenous zyxin level in four control MEF lines. The same validation workflow as in (**A-C**) was applied.

(**D**) Because the zyxin-KO MEF line was derived from a zyxin-KO mouse,[22] no parental
975 cell line is available; control MEF lines 1-4 were therefore used as references for expression matching.

(**E**) Tagged-zyxin constructs are functional, as shown by the *lower* ability of the zyxin-KO MEFs rescued with tagged zyxin constructs to attach to fibronectin-coated plastic dishes (mean ± SEM, n = 6 dishes), in agreement with the previous report.[22]

980 (**F**) Tagged-zyxin constructs incorporate into IACs (basal confocal section). The contour of a non-rescued cell is shown in yellow (these cells spread more than rescued MEFs).

(**G**) Related to Figure 1A. Single-molecule visualization of fluorescent talin and zyxin clusters located on the apical PM (**left and middle**). Clusters were detected after 30-frame rolling averaging (1 s) and background subtraction using an in-house Gaussian-spot detection
985 routine (yellow circles; **bottom**). The result of Halo7-far [Farnesylated Halo7] is shown as

a monomeric control (**right column**). See Video S1.

(**H**) Related to Fig. 1E. Method for evaluating the colocalization index based on the pair cross-correlation function (PCCF).[20,21,124] For details, see STAR Methods.

(**I-M**) Establishment of the T24-T cell line (T24 stably expressing SNAPf-talin; "T" denotes talin), used for testing the recruitment of FA proteins and signaling molecules to talin/zyxin clusters. T24 cells were selected because single-molecule imaging on the apical PM is facilitated by their flatter apical surfaces. The Halo7 tag was used to label signaling molecules, whereas the SNAPf tag was used for talin. Labeling efficiencies were ≈88% (Halo7) and ≈66% (SNAPf) (STAR Methods).

(**I**) Western blot quantification of total talin1 (endogenous + SNAPf-talin1; bands not resolved and thus quantified together) in T24-T cells (mean ± SEM, n = 4 replicates). Total talin1 is ≈1.7× higher than in parental T24 cells.

(**J**) Typical image of SNAPf-talin located on the apical PM of a T24-T cell.

(**K**) The number density of talin clusters found on the apical PM of T24-T cells (containing SNAPf-talin) is 0.18/μm^2, slightly lower than in talin-dKO MEFs rescued with Halo7-talin (0.26/μm^2, n = 15 cells).

(**L and M**) In T24-T cells, as found in MEFs, engaged CD59 and PDGFR (trajectories in **L**) are transiently recruited to talin clusters (white puncta in **L**), confirming the consistency between the two cell types in terms of receptor recruitment (Figures 1C and 1D). Their dwell lifetimes are 0.39 ± 0.070 and 0.15 ± 0.012 s, respectively (**L**), consistent with the findings in MEFs (0.32 ± 0.061 and 0.22 ± 0.035 s, respectively; Figure 1D). n = 20 cells, n = 3,209, 2,471, 1,485, and 3,261 events for CD59 monomer, CD59 cluster, without PDGF, and PDGF addition, respectively.

Games-Howell's test for (**A, B, and E**), one-way ANOVA for (**D**), and Brunner-Munzel's test for (**M**).

Figure S2. Molecular stoichiometry, dynamics, and signaling functions of GEMs, related to Figure 2.

(**A**) Two-component lifetime analysis distinguishes talin–zyxin co-clusters from incomplete clusters. The plots show lifetime distributions of Halo7-talin clusters in zyxin-KO MEFs with or without zyxin re-expression at endogenous levels (**left**) and Halo7-zyxin clusters in talin-dKO MEFs with or without talin re-expression at endogenous levels (**right**). Distributions were fitted with a sum of two exponentials (providing decay times; SEM = fitting error, n = 10 cells, n = 2,148 ~ 7,273 clusters). In the absence of the partner protein (talin or zyxin), the long-lived component (τ_2) is largely lost, leaving a short-lived component ($\tau_1 \approx 1$ s). In contrast, talin-zyxin co-clusters exhibit a prominent long-lived component ($\tau_2 \approx 7.7$ - 9.5 s).

(**B**) Related to Figure 2E. Broad and uncorrelated talin/zyxin copy numbers in individual GEMs, indicating flexible stoichiometries (zyxin-KO MEFs; n = 15 cells, n = 7,729 clusters). Figure 2E shows the corresponding analysis performed in rescued talin-dKO MEFs.

(**C**) Related to Figure 2D. Distributions of talin copy numbers per GEM after CD59 and PDGF stimulation.

(**D**) Related to Figure 2F. The dwell lifetime of zyxin in GEMs is 1.4 s (n = 10 cells, n = 581 events), which was obtained from single-molecule dwell time distributions. For talin, the corresponding dwell lifetime is 2.1 s (Figure 2F).

(**E**) Schematic overview of reported interactions among IAC-associated proteins and their links to actin filaments, actin binding proteins, and PI(4,5)P_2.

Brunner-Munzel's test for (**A**) and Steel-Dwass' test for (**C**; vs. talin cluster).

Figure S3. PI(4,5)P_2 and raft domains are colocalized with GEM, related to Figure 2.

(**A**) Single-molecule colocalization indexes of protein probes for various lipids, MARCKS, and PI kinases (Halo7-tagged) with GEMs (PI3K data are the same as those shown in Figure 5A;
1040 *n* = 20 cells).

PI(4,5)P_2 is enriched at GEMs relative to the bulk PM, consistent with the enrichment of MARCKS, a PI(4,5)P_2-binding protein. PIP5K, which produces PI(4,5)P_2 from PI(4)P and binds talin,[125] and PI(4) are also recruited to GEMs. Their colocalization indexes are not detectably altered by PDGF stimulation. Because PLCγ can hydrolyze PI(4,5)P_2 to generate
1045 PI(4)P, these localizations are consistent with local PI(4,5)P_2 turnover at GEMs.

PI(3,4,5)P_3 was detected at GEMs only after PDGF stimulation, and PI3K showed increased colocalization with GEMs only after PDGF stimulation, consistent with PDGF-dependent PI(3,4,5)P_3 production from PI(4,5)P_2 at GEMs. We did not detect PI(3)P or PI(3,4)P_2 at GEMs under these conditions.

1050 (**B**) Typical trajectories of PIP5K and MARCKS diffusing on the PM cytoplasmic surface, showing transient colocalization with GEMs (talin clusters, white puncta) (Video S4).

(**C**) Partial cholesterol depletion reduces the GEM cluster size (talin copy number per cluster). Distributions of the number of Halo7-talin molecules in a GEM cluster (*n* = 15 cells, *n* = 3,159 ~ 8,281 clusters), before and after cholesterol depletion (basic data for Figure 2K).

1055 (**D-H**) Optogenetic partial depletion of PI(4,5)P_2 reduces GEM size (talin copy number per cluster) and GEM # density on the PM.

(**D**) Schema for optogenetic partial depletion of PI(4,5)P_2 from the PM using the CIBN-CRY2 system, where phosphoinositide 5-phosphatase (5PT) is linked to CRY2.[33]

(**E**) Representative confocal micrographs of mScar-CRY2-5PT and SiR:SNAPf-2xPH
1060 (PI(4,5)P_2 probe), recorded before, 1 min after, and 15 min after the blue light irradiation (Before, After, and Recovery, respectively). Both mScar-CRY2 conjugates (WT-5PT and catalytically inactive D523G-5PT) were recruited to the PM after irradiation, whereas a decrease in the PI(4,5)P_2 probe signal was observed only in cells expressing (mScar-CRY2-)WT-5PT.

1065 (**F**) Time courses of the PI(4,5)P_2 level in the PM (mean ± SEM, *n* = 10 cells).

(**G**) Typical images of GEMs (Halo7-talin clusters) showing that GEM number density in the apical PM and GEM cluster size decrease immediately after irradiation in cells expressing (mScar-CRY2-)5PT, with D523G-5PT as the control.

(**H**) Mean talin copy number per GEM (cluster size) and mean GEM number density on
1070 the apical PM (*n* = 10 cells). The GEM cluster size and number density decrease after light-induced PI(4,5)P_2 reduction and recover after illumination stops.

(**I and J**) Drugs that reduce PI(4,5)P_2 levels decrease GEM cluster size (talin copy number).

(**I**) Representative confocal micrographs of the PI(4,5)P_2 probe, SNAPf-2xPH, showing reduced PI(4,5)P_2 levels in the PM after drug treatments.[34] The Ca^{2+} ionophore ionomycin
1075 induces PI(4,5)P_2 hydrolysis by activating the Ca^{2+}-dependent PLC. Phenylarsine oxide and quercetin inhibit phosphatidylinositol 4-kinase, reducing PI(4)P production, the main substrate for PI(4,5)P_2 generation.

(**J**) Distributions of the number of Halo7-talin molecules in a GEM cluster (*n* = 15 cells, *n* = 3,159 ~ 8,281 clusters) before and after drug-induced partial depletion of PI(4,5)P_2
1080 (basic data for Figure 2K).

Games-Howell's test for (**C and I**), two-tailed Welch's t-test for (**C**), and Steel-Dwass' test for (**C and J**).

1085 **Figure S4. PALM-based detection and analysis of talin and zyxin clusters, related to Figure 2.**

(**A**) Conventional and PALM super-resolution images (Voronoï diagram) of GEM, visualized by mEos3.2-zyxin on the apical and basal PMs. The areas surrounded by the green curve (middle image) indicate regions with good focus (top; apical PM, which is tilted) or without
1090 obvious focal adhesions (bottom; basal PM) and were used for further analysis. The cyan lines in the right images indicate the smallest polygon enclosing each clustered region.

(**B-E**) Evaluation of the true cluster diameter from the PALM data by correcting for localization errors using simulations.[108]

(**B**) Distributions of the localization errors of mEos3.2 on the apical and basal PMs.[108]

1095 (**C**) Representative simulation workflow and typical results: Cluster centers were regularly placed at the average density observed by PALM experiments (D_{clus}, clusters/μm^2). Circular boundaries with various diameters (10 – 300 nm) were drawn around the cluster centers, and localized-molecule coordinates (dots) were generated at experimentally matched densities inside and outside the boundary (D_{in} and D_{out} spots/μm^2, respectively,
1100 determined from experiments; **C, two left panels**). Localization errors were then applied to each coordinate by sampling from the distributions in (**B**) (**C, two right panels**).

(**D**) Calibration curves relating the cluster diameter estimated by the tessellation analysis (x axis) to the true cluster diameter (y axis). Simulated PALM datasets were processed identically to experimental data, and the resulting estimated diameters were plotted
1105 against the true input diameters. Each curve was fitted with a cubic polynomial and used for calibration.

(**E**) Distributions of raw (uncorrected) and calibrated (localization-error–corrected) cluster diameters.

(**F and G**) Distributions of the calibrated GEM diameters (**F**) and the number of molecules
1110 per GEM (**G**).

(**H**) Number densities of GEMs on the apical and basal PMs (mean ± SEM).

Figure S5. *In vitro* formation of micron-scale liquid-like condensates of zyxin alone and VASP alone, coarse-grained MD simulations of zyxin IDR2, quantification of endogenous and tagged zyxin/VASP concentrations, overexpression-induced micron-scale co-condensates of zyxin and VASP in cells, and GEM fusion/fission, related to Figure 3.

(**A-C**) Related to Figures 3A-3C. Zyxin (mCherry-zyxin) alone and VASP (mGFP-VASP) alone form liquid-like micron-scale condensates *in vitro* upon the addition of PEG8K (final 1%) (**A**). FRAP data were obtained 10 min after PEG8K addition (**B and C**; mean ± SEM, n = 10 condensates). Condensates of zyxin-VASP mixture exhibited intermediate FRAP recovery between VASP-only and zyxin-only condensates (**C**).

(**D-F**) Related to Figures 3E and 3F. Coarse-grained (CG) molecular dynamics (MD) simulations of zyxin IDR2. Throughout (**D–F**), 'temperature' denotes the CG-MD simulation (thermostat) temperature, a model control parameter, and is not directly comparable to experimental temperature.

(**D and E**) Single-chain conformational analysis of zyxin (IDR2) across temperatures. (**D**) Pairwise residue distance R_{ij} plotted as a function of sequence separation $|i-j|$ for simulations performed from 210 K to 440 K (10-K intervals; CG simulation temperatures; see above). The results were fitted with a function, $R_{ij} \sim K|i-j|^{\nu}$, where K and ν are fitting parameters (ν is the Flory scaling exponent). (**E**) Temperature dependence of ν extracted from the fits in (**D**). The red dashed line marks ν = 0.5, corresponding to the θ-condition. The simulation temperature at which ν approaches 0.5 is used as an estimate of the critical temperature (T_c) for phase separation.

(**F**) Temperature-dependent condensate density evolution of zyxin (IDR2) in CG MD simulations. (**Left**) Local density profiles along the z-axis for simulations at 210–290 K, shown as time-evolving traces. At lower simulation temperatures (210-230 K), densities remain localized, indicating a stable, compact condensate. With increasing simulation temperature, the density profile broadens, consistent with partial or complete dissolution of the condensate. (**Right**) Representative final snapshots at the corresponding temperatures. At low temperatures, chains form a compact droplet-like assembly; at higher temperatures, chains adopt a more dispersed state. Individual chains are colored from green to blue for visualization.

(**G-I**) Related to Figures 3B, 3C, and 3H. In cells (T24 cells), overexpression of zyxin alone (mCherry-zyxin), VASP alone (mGFP-VASP), or both molecules induces micron-scale liquid-

hydrogel-like condensates.

(**G**) Cytoplasmic concentrations of highly overexpressed mCherry-zyxin, mGFP-VASP, and mGFP-RIAM used for FRAP assays shown in (**H**) and (**I**), as well as in Figures 3B, 3C, and
1150 3H (mean ± SEM, n = 15 cells). Concentrations were estimated by confocal microscopy, using purified mCherry-zyxin and mGFP-VASP in PBS as standards. Relative to the endogenous levels in Figure 3G, zyxin and VASP are overexpressed by ≈19× and ≈24×, respectively.

(**H**) Typical FRAP image series for condensates of mCherry-zyxin alone (**top**) and mGFP-
1155 VASP alone (**bottom**).

(**I**) FRAP recovery curves (mean ± SEM, n = 15 condensates). Condensates of the zyxin-VASP mixture exhibited intermediate recovery between VASP-only and zyxin-only condensates, consistent with the observations made *in vitro* (see **C**).

(**J-L**) Related to Figure 3G. Quantification of cytoplasmic concentrations of endogenous and
1160 tagged zyxin and VASP.

(**J**) Typical western blots used to estimate endogenous and tagged zyxin/VASP amounts. Absolute protein amounts were calibrated using purified mCherry-zyxin and mGFP-VASP standards.

(**K**) Total copy numbers per cell determined from the western blots (see **J**; mean ± SEM,
1165 n = 4 replicates). Endogenous VASP concentrations are consistent with a previous report.[126]

(**L**) Cytoplasmic volume (cell volume minus nuclear volume) determined by confocal microscopy (mean ± SEM, n = 4 replicates).

(**M**) Related to Figure 3K (GEMs visualized as zyxin clusters). Typical time series showing
1170 GEM merging and splitting.

Figure S6. Mild PDGF stimulation leads to enhanced Ca^{2+} mobilization under conditions where the mutual activation of FAK and SFK (Lyn) is optogenetically induced, related to Figure 6.

(**A-E**) OptoDroplet-induced liquid-like co-assembly[68,69] of FAK and Lyn enhances Ca^{2+} mobilization under mild PDGF stimulation, beyond simple additivity.

(**A**) Schematic of the optoDroplet experiments.[68,69] OptoFAK and optoLyn (FAK and Lyn fused to a membrane-targeted optoDroplet cassette consisting of Src myristoylation signal peptide, FUS N-terminal IDR, a fluorescent tag protein, and the light-sensitive protein CRY2) were expressed in zyxin-KO MEFs rescued with mGFP-zyxin, and cytoplasmic Ca^{2+} concentrations were monitored before and during blue light illumination with or without 20 pM PDGF (mild stimulation).

(**B**) Representative confocal micrographs of optoFAK (Halo7) and optoLyn (SNAPf) on the basal PM.

(**C**) Typical images of GEMs (talin clusters) and light-induced optoDroplets of optoFAK (Halo7) and optoLyn (SNAPf), showing partial colocalization (13.6 ± 1.3% of optoDroplets colocalized with GEMs, and 19.0 ± 2.4% of GEMs colocalized with optoDroplets).

(**D**) Typical Ca^{2+} mobilization time course upon the addition of 20 pM PDGF.

(**E**) OptoDroplet formation (co-condensation) of optoFAK and optoLyn markedly enhances Ca^{2+} responses upon mild PDGF stimulation. The graph shows the total Ca^{2+} signal (AUC of traces as in **D**) (mean ± SEM, n = 196 ~ 278 cells).

(**F-H**) FAK activation assay using a binder-tag readout. Enhancement of FAK activity via the formation of optoDroplets of optoFAK and optoLyn.

(**F**) Schematic of the binder-tag system to report FAK activation before and after optoDroplet induction with or without mild PDGF stimulation. In this binder-tag system, an SsrA peptide is inserted into the central region of FAK so that it can become accessible in the open/active conformation, enabling the binding of SNAPf-tagged SspB.[67]

(**G**) Representative two-color image of opto-SsrA-FAK (green) and optoLyn (magenta) overlaid with trajectories of SspB after blue-light illumination and mild PDGF stimulation, indicating SspB recruitment to the optoDroplets.

(**H**) FAK activity increases ≈4-fold when both optoFAK and optoLyn are present in the same optoDroplet under mild PDGF stimulation, quantified by SspB recruitment normalized by the expression level (mean ± SEM, n = 15 cells).

Games-Howell's test for **E and H**.

The mild PDGF condition activates Lyn downstream of PDGFR but does not measurably activate FAK under these conditions (Figure 6E). However, when light illumination induces the co-assembly of optoFAK and optoLyn into liquid-like optoDroplets, FAK becomes responsive to the mild PDGF input. Using a previously developed binder assay for the open, active conformation of FAK,[67] we detected the robust recruitment of the SspB binder to the optoDroplets after mild PDGF stimulation (Figures S6F-S6H). These observations suggest that, under the nanoscale co-confinement of Lyn and FAK in a liquid state, the Lyn initially activated by PDGFR can phosphorylate/activate FAK (which is not generally activated by the mild PDGF stimulation), which in turn can phosphorylate Lyn, inducing a chain (spiral-like) mutual activation reaction.

Meanwhile, without light activation, mild PDGF stimulation elicited only a slight Ca^{2+} response, but upon the formation of a light-induced optoDroplet containing *both* optoFAK and optoLyn, the Ca^{2+} response was enhanced by ≈6-fold relative to the dark state (Figure S6D and S6E). Because Ca^{2+} mobilization in this setting is downstream of PLCγ1–IP_3 signaling, these results are consistent with the idea that cooperative Lyn–FAK co-activation within the liquid-like optoDroplet promotes PLCγ1 recruitment/activation, thereby potentiating the IP_3–Ca^{2+} output under otherwise subthreshold PDGF stimulation conditions.

1225 **Figure S7. Cell proliferation comparison between *in vivo* and in culture with and without CD59 knockdown, examination using human cancer cell lines, and Akt recruitment to GEMs in cultured cells, related to Figure 7.**

(**A**) Related to Figure 7A-7D, and particularly to Figure 7C. *In vitro* proliferation of zyxin-KO MEFs rescued with WT-zyxin or IDR2 is faster than that rescued with ΔIDR2 (mean ± SEM,
1230 *n* = 3 replicates).

(**B**) Generation of zyxin-KO cell lines from human colon (RKO) and breast (MDA-MB231) cancer cell lines using CRISPR/Cas9 and re-expression of WT-zyxin, IDR2, or ΔIDR2 at levels comparable to endogenous zyxin in the respective parental lines. Typical western blot pattern (**top**) and band quantification results (**bottom**; normalized by the GAPDH band
1235 intensities; mean ± SEM, *n* = 4 replicates) are shown.

(**C**) *In vitro* proliferation of zyxin-KO human cancer cell lines rescued with WT-zyxin or IDR2 is faster than when rescued with ΔIDR2 (mean ± SEM, *n* = 3 replicates).

(**D-F**) Results obtained in mice showing that the presence of zyxin's IDR2 is critical for the growth of solid tumors of RKO cells in mice.

1240 (**D**) Representative images of excised tumors.

(**E**) Tumor growth curves (mean ± SEM, *n* = 10 mice).

(**F**) Weight of excised tumors (RKO cells) 29 days after injection (mean ± SEM, *n* = 10 tumors).

(**G**) Related to Figure 7E. Single-molecule colocalization index of Akt with GEMs (*n* = 20
1245 cells).

(**H**) Related to Figure 7F-7H. *In vitro* growth curves show that CD59 knockdown does not detectably affect proliferation under standard culture conditions, in contrast to the *in vivo* requirement for CD59 in tumor growth (mean ± SEM, *n* = 3 replicates).

Games-Howell's test for (**A, C, E, F - H**) and one-way ANOVA for (**B and G**).

1250

SUPPLEMENTAL ITEM TITLES AND LEGENDS

Video S1. Visualizing the talin and zyxin clusters on the apical PM by rolling averaging, related to Figure 1A.

Movies recorded at video rate (**top**) and those after rolling averaging over 30 frames and background subtraction (**bottom**) are replayed at video rate. Halo7-talin expressed in a talin1/2-dKO MEF, Halo7-zyxin in a zyxin-KO MEF, and Halo7-farnesyl expressed in a talin2 KO MEF were labeled with the SaraFluor650-conjugated Halo-ligand and observed on the apical PM. After rolling averaging, the signals from the fast-diffusing molecules in the cytoplasm and on the PM, like Halo7-farnesyl, became averaged out. Meanwhile, immobile and slowly diffusing molecules and molecular clusters bound to the PM were visible even after rolling averaging (marked by circles in the bottom movies). The original data for Figures 1A and S1G. Representative movies among 20 movies.

Video S2. Transient recruitment of a CD59 cluster and a PDGF molecule to a GEM, related to Figure 1C.

(Left) Real-time movie of PDGFR molecules (magenta, with a trajectory; SaraFluor650 label) superimposed on the rolling-averaged movie of GEMs (observed as SNAPf-talin clusters in a Talin1/2-dKO MEF; green; TMR label) observed on the apical PM (recorded at video rate) after PDGF stimulation. PDGFR spots might represent PDGFR monomers or oligomers, but due to the presence of endogenous non-labeled PDGFR molecules, we could not differentiate these two possibilities. The original data for Figure 1C, left. A representative movie among 20 movies.

(Right) Real-time movie of CD59 clusters formed by the addition of anti-CD59 mAb-coated fluorescent beads (magenta, with a trajectory), superimposed on the rolling-averaged movie of GEMs (observed as SNAPf-talin clusters in a Talin1/2-dKO MEF; green; TMR label) observed on the apical PM (recorded at video rate). The original data for Figure 1C, right. A representative movie among 20 movies.

Video S3. Simultaneous triple-color single fluorescent particle/molecule tracking of GEMs, CD59 clusters, and PLCγ1 molecules, related to Figures 3A-3C.

Real-time movie of engaged CD59 clusters (magenta, anti-CD59 mAb-coated fluorescent beads, with a trajectory) and single PLCγ1-Halo7 molecules (cyan; SaraFluor650 label)

1285 superimposed on the rolling-averaged movie of GEMs (observed as SNAPf-talin clusters; green; TMR label) on the apical PM of a T24-T cell, recorded at video rate. The original data for Figure 3A. A representative movie among 30 movies.

Video S4. Transient recruitment of a FAK molecule and a PIP5K molecule to a
1290 **GEM upon PDGF stimulation, related to Figure 3.**

Real-time movies of Halo7-PIP5K without stimulation (**left**) and Halo7-FAK after PDGF stimulation (**right**) (magenta, with a trajectory; SaraFluor650 label) superimposed on a rolling-averaged movie of GEMs (observed as SNAPf-talin clusters; green; TMR label) on the apical PM of a T24-T cell, recorded at video rate. The original data for Figure 3E and Figure
1295 S4D bottom, respectively. A representative movie among 20 movies.

Video S5. Coarse-grained MD simulation of a zyxin IDR2 condensate, related to Figure 3.

Movie of a coarse-grained MD simulation of a 200-chain zyxin IDR2 condensate at 210 K.
1300 The simulation time step was 0.1 ns, and the total simulated time was 1 ms (10^7 steps). The first 2×10^6 steps are shown.

Table S1. Detailed experimental conditions and results including all statistical parameters.

1305 Detailed experimental conditions (including the employed tag proteins, fluorescent dyes, and cells) and results (including the raw data, the number of replicates, fitting results, and statistical test results).

Data S1. Plasmids used in this study and their complete sequences, related to
1310 **STAR Methods.**

List of plasmids used in this study in an Excel table and plasmid sequence files in GenBank format with annotations.

Note S1. IDRs of the examined proteins, related to Figure 5.

1315 Summary of the IDRs of proteins (human) employed in this research, predicted by MobiDB 3.0.

STAR★METHODS

1320 ## KEY RESOURCES TABLE

REAGENT or RESOURCE	SOURCE	IDENTIFIER
Antibodies		
Mouse anti-talin1 (clone 93E12)	Abcam	Cat# ab104913, Lot# GR24449-3, RRID:AB_10858284
Mouse anti-talin1 (clone 97H6)	Bio-Rad	Cat# MCA4770, Lot# 1803 RRID:AB_10671591
Rabbit anti-zyxin (B71)	Merck	Cat# ABC1463, Lot# Q3027780
Rabbit anti-GFP	ProteinTech	Cat# 50430-2-AP, Lot# 78456, RRID:AB_11042881
Rabbit anti-VASP (clone 9A2)	Cell Signaling Technology	Cat# 3132, Lot# 5, RRID:AB_2213393
Rabbit anti-Akt	Cell Signaling Technology	Cat# 9272, Lot# 5, RRID:AB_329827
Rabbit anti-phospho-Akt (pS473, clone D9E)	Cell Signaling Technology	Ca# 4060, Lot#: 25, RRID:AB_2315049
Rabbit anti-FAK	Cell Signaling Technology	Ca# 3285, Lot# 9, RRID:AB_2269034
Rabbit anti-pFAK (pY397, clone D20B1)	Cell Signaling Technology	Ca# 8556, Lot# 5, RRID: AB_10891442
Rabbit anti-JAK1	Cell Signaling Technology	Ca# 3332, Lot# 6, RRID: AB_2128499
Rabbit anti-pJAK1 (pY1034/1035)	Cell Signaling Technology	Ca# 3331, Lot# 7, RRID: AB_2265057
Mouse anti-CD59a (clone mCD59.3), PE-conjugated	BioLegend	Ca# 143104, Lot# B369667, RRID: AB_10962439
Mouse anti-GAPDH	ProteinTech	Cat# 60004-1-Ig, Lot# 10008047, RRID:AB_2107436
Goat anti-mouse IgG HRP-conjugated	Thermo Fisher Scientific	Cat# G21040, Lot# 2122350, RRID:AB_2536527
Goat anti-rabbit IgG HRP-conjugated	Thermo Fisher Scientific	Cat# G21234, Lot# 2087715, RRID:AB_2536530
Donkey anti-mouse IgG RhodamineRedX-conjugated	Jackson ImmunoResearch Labs	Cat# 715-295-150, Lot# 145566, RRID:AB_2340831

Donkey anti-rabbit IgG RhodamineRedX-conjugated	Jackson ImmunoResearch Labs	Cat# 711-295-152, Lot# 145693, RRID:AB_2340613
Mouse anti-CD59 (clone MEM43/5)	This paper	N/A
Mouse anti-Thy1 (clone OX7)	This paper	N/A
Rabbit anti-CHO	ProteinTech	Cat# 27803-1-AP, RRID:AB_2880976
Bacterial and virus strains		
E. coli HST08 Premium Competent Cells	Takara	Cat# 9128
BL21 (DE3) *E. coli* competent cells	New England BioLabs	Cat# C2527
KRas_G12V (RFP-Bsd) Lentivirus	GenTarget	Cat# LVP1139-RB
Chemicals, peptides, and recombinant proteins		
Fibronectin	Sigma Aldrich	Cat# F1141
Mouse leukemia inhibitory factor	Millipore	Cat# ESG1106
Epidermal growth factor	Wako	Cat# 053-07871
Platelet-derived growth factor	Pepro Tech	Cat# 100-14B
Uridine triphosphate	Invitrogen	Cat# R0471
Carboxylate-modified yellow-green fluorescent 40-nm polystyrene beads	Molecular Probes	Cat# F8795
Carboxylate-modified dark-red fluorescent 40-nm polystyrene beads	Molecular Probes	Cat# F8789
EDC	Pierce	Cat# 22980
sulfo-NHS	Pierce	Cat# 24525
Polyethylene glycol, 20,000 kDa	Sigma Aldrich	Cat# P5413
Bovine serum albumin	Sigma Aldrich	Cat# A3059
PP2	Selleckchem	Cat# S7008
PF573228	Cayman Chemical	Cat# 14924
Latrunculin A	Wako	Cat# 125-04363
Cytochalasin D	Cayman Chemical	Cat# 11330
Y27632	ChemScene	Cat# CS-0878
Methyl-β-cyclodextrin	Sigma Aldrich	Cat# 332615
Methyl-β-cyclodextrin-cholesterol complex	Sigma Aldrich	Cat# C3045
Saponin	Nacalai Tesque	Cat# 30502-42
Ionomycin	Wako	Cat# 093-04531
Phenylarsine oxide	Tokyo Chemical Industry	Cat# P0140
Quercetin	Sigma Aldrich	Cat# Q4951
1,6-hexanediol	Wako	Cat# 081-00435
Protease inhibitor cocktail	Nacalai Tesque	Cat# 25955-24
Phosphatase inhibitor cocktail	Nacalai Tesque	Cat# 07574-61
Protease inhibitor cocktail (cOmplete)	Roche	Cat# 11873580001
Blocking One	Nacalai Tesque	Cat# 03953-95
precast 4-20% gradient polyacrylamide gel	Bio-Rad	Cat# 4561096
PVDF membrane (FluoroTransW)	Pall	Cat# BSP0161
PVDF membrane (Immobilon-P)	Millipore	Cat# IPVH00010
WB Stripping Solution	Nacalai Tesque	Cat# 05364-55
SNAP-tetramethylrhodamine (TMR) star	New England BioLabs	Cat# S9105S
TMR-Halo linker	Promega	Cat# G8251
SaraFluor650T Halo linker	Goryo Chemical	Cat# A308-02
JF646 Halo linker	Promega	Cat# GA1120
SeTau647-Halo linker	Tsunoyama et al.[127]	N/A
isopropyl-β-D-thiogalactopyranoside	Amresco	Cat# MFCD00063273
D4H	This paper	N/A
OlyA(E69A)	This paper	N/A

TrueCut Cas9 Protein v2	Invitrogen	Cat# A36498
Standardized human serum	Sigma Aldrich	Cat# C9473
Human complement C8	Sigma Aldrich	Cat# C3535
C8-depleted human serum	Sigma Aldrich	Cat# C1538
C9-depleted human serum	Calbiochem	Cat# 234409
CF640R SE/TFP ester	Biotium	Cat# 92108
Critical commercial assays		
Gibson Assembly Master Mix	New England BioLabs	Cat# E2611L
Zero Blunt TOPO PCR Cloning Kit for Sequencing	Invitrogen	Cat# 450159
Mycoplasma PCR Detection Kit	Beyotime Biotechnology	Cat# C0301S
VenorGeM Mycoplasma Detection Kit	Minerva Biolabs	Cat# MNV11-1100
SF Cell Line 4D-Nucleofector X Kit L	Lonza	Cat# V4XC-2012
SE Cell Line 4D-Nucleofector X Kit L	Lonza	Cat# V4XC-1012
PVDF transfer pack	Bio-Rad	Cat# 1704156
Western BLoT Hyper HRP Substrate	Takara	Cat# T7103B
NucSpot Live 650	Biotium	Cat# 40082
CalBryte 590	AAT Bioquest	Cat# 20700
Ni-NTA agarose beads	Sangon Biotech	Cat# C600332-0001
Millex filter (0.45 μm pore)	Millipore	Cat# SLFH05010
Amicon Ultra concentrator (10 kDa cutoff)	Millipore	Cat# UFC501008
Expi293 Expression System Kit	Thermo Fisher Scientific	Cat# A14635
MBP-binding dextrin Sepharose column (MPBTrap)	GE Healthcare	Cat# 28-9187-78
Ni-NTA Resin (HisPur)	Thermo Fisher Scientific	Cat# 88222
Poly-Prep Chromatography Column	Bio-Rad	Cat# 731-1550
Protein Concentrator (30 kDa MWCO)	Thermo Fisher Scientific	Cat# 88502
Micro-dialyzer units (10 kDa MWCO)	Thermo Fisher Scientific	Cat# 69576
InstantBlue Coomassie Protein Stain	Abcam	Cat# ab119211
VitroGel	TheWell Bioscience	Cat# VHM01
TransIT-293	Mirus	Cat# MIR2700
Lentiviral High Titer Packing Mix	Takara	Cat# 6194
Lenti-X Concentrator	Takara	Cat# 631232
Blue DCS1	AAT Bioquest	Cat# 17548
NucRed Live 647	Invitrogen	Cat# R37106
Experimental models: Cell lines		
Human: T24	Generous gift from Masahiro Sokabe (Nagoya University)[128]	N/A
Human: HeLa	RIKEN Cell Bank	Cat# RCB0007
Human: RKO	ATCC	CRL-2577
Human: MDA-MB231	ATCC	CRM-HTB-26
Chinese Hamster: CHO-K1	Dainippon Pharma Co., Ltd.	Cat# 03-402
Mouse: talin1 and 2 double knockout mouse embryonic fibroblast	Generous gift from Reinhard Fässler (Max Planck Institute of Biochemistry)[19]	N/A
Mouse: talin 2 knockout mouse embryonic fibroblast	Generous gift from Reinhard Fässler (Max Planck Institute of Biochemistry)[19]	N/A

Mouse: zyxin knockout mouse embryonic fibroblast	Generous gift from Mary C. Beckerle (University of Utah)[22]	N/A
Mouse: control mouse embryonic fibroblast, lines 1-3	Generous gift from Noboru Mizushima (University of Tokyo)	N/A
Mouse: control mouse embryonic fibroblast, line 4	Generous gift from Ryusuke Kuwahara (Okinawa Institute of Science and Technology Graduate University)	N/A
Mouse: NIH3T3	Generous gift from Makoto Kinoshita (Nagoya University)[129]	N/A
Mouse: mouse embryonic stem cell (clone E14tg2a)	RIKEN Cell Bank	Cat# AES0135 Lot# 2
Mouse: hybridoma (clone MEM43/5)	Generous gift from Vaclav Horejsi (Institute of Molecular Genetics of the Czech Academy of Sciences)[130]	N/A
Mouse: hybridoma (clone OX7)	European Collection of Cell Cultures[131,132]	Cat# 84112008
Lenti-X 293T	Takara	Cat# 632180
Experimental models: Organisms/strains		
BALB/cAJcl-*Foxn1*^{nu} (nude) female mice	CLEA Japan, Inc.	BALB/cAJcl-*nu/nu*
Recombinant DNA		
Plasmid: pEGFP	Clontech	Cat# Z2370N
Plasmid: pmCherry	Clontech	Cat# Z2522N
Plasmid: pcDNA3.1(+)-Hygro	Invitrogen	Cat# V87020
Plasmid: pcDNA3.1(+)-Zeo	Invitrogen	Cat# V86020
Plasmid: pET26B	Novagen	Cat# 69862
Plasmid: pCR4Blunt-TOPO	Invitrogen	Cat# 450159
Plasmid: pPBpuro	Generous gift from Michiyuki Matsuda (Kyoto University)[133]	N/A
Plasmid: pCMV-mPBase	Generous gift from Michiyuki Matsuda (Kyoto University)[133]	N/A
Plasmid: pLKO1hygro	Generous gift from Robert A. Weinberg (Massachusetts Institute of Technology)	Addgene plasmid# 24150
SNAPf	New England Biolabs	Cat# N9172S
Halo7	Promega	Cat# G9651
mEGFP	Clontech	Cat# Z2370N
mCherry	Clontech	Cat# Z2522N
mEos3.2	Fujiwara et al. and McKinney et al.[134–136]	Addgene plasmid# 20341
mScarlet-I	[137]	N/A
Talin1	Kazusa DNA Research Institute	Cat# ORK01622
Zyxin	Kazusa DNA Research Institute	Cat# ORS08391

VASP	Kazusa DNA Research Institute	Cat# FHC28647
α-Actinin	Allele Biotechnology	Cat# Aact-138
Paxillin	Tsunoyama et al.[127]	N/A
Vinculin	Kazusa DNA Research Institute	Cat# FXC01835
FAK	Generous gift from Caroline H. Damsky (University of California San Francisco) [138]	N/A
Filamin A	Allele Biotechnology	Cat# FILA-106
RIAM	Lee et al.[139]	Addgene plasmid# 80028
β3 integrin	Generous gift from Jonathan C. Jones (Northwestern University)[140]	N/A
N-WASP	Generous gift from Jack Taunton (University of California, San Francisco)[141]	N/A
PIP5KIγ	Generous gift from Richard A. Anderson (University of Wisconsin)[142]	N/A
PIK3CA	Kazusa DNA Research Institute	Cat# FXC01204
MARCKS	Kazusa DNA Research Institute	Cat# FXC03149
CD59	Generous gift from Masahide Tone (Oxford University)[143]	N/A
Thy1	Nemoto et al.[144]	N/A
PDGFR-β	Johannessen et al.[145]	Addgene plasmid# 23893
PLCγ1	Generous gift from Dr. Matilda Katan (University College London)[146]	N/A
PLCβ1	Generous gift from Katsuhiko Mikoshiba (ShanghaiTech University)[147]	N/A
Lyn	Suzuki et al.[4,5]	N/A
Akt	Kazusa DNA Research Institute	Cat# FXC02215
JAK1	Kazusa DNA Research Institute	Cat# FXC01306
CD47	Generous gift from Eric C. Brown (Genentech)[148]	N/A
PI(3)P probe	Generous gift from Toshiki Itoh (Kobe University)[32]	N/A
PI(4)P probe	Generous gift from Toshiki Itoh (Kobe University)[32]	N/A

PI(3,4)P_2 probe	Generous gift from Toshiki Itoh (Kobe University)[32]	N/A
PI(4,5)P_2 probe	Generous gift from Toshiki Itoh (Kobe University)[32]	N/A
PI(3,4,5)P_3 probe	Generous gift from Toshiki Itoh (Kobe University)[32]	N/A
Phosphatidylserine probe	Generous gift from Tomohiko Taguchi (Tohoku University)[30,31]	N/A
Cholesterol probe (D4H)	Johnson et al.[149,150]	N/A
Sphingomyelin probe (OlyA(E69A))	Endapally et al.[29]	N/A
CIBN-CAAX	Idevall-Hagren et al.[33]	Addgene plasmid# 79574
CRY2-5ptase	Idevall-Hagren et al.[33]	Addgene plasmid# 66836
CRY2-5ptase(D523G)	Idevall-Hagren et al.[33]	Addgene plasmid# 66837
Membrane-optoDroplet	Dine et al.[69]	Addgene plasmid# 111509
Membrane-optoDroplet	Generous gift from Klaus M. Hahn, (University of North Carolina)[67]	
Binder	Generous gift from Klaus M. Hahn, (University of North Carolina)[67]	Addgene plasmid# 179142
Oligonucleotides		
sh-CD59a-F: 5'-CCGGCGGTGGTTTCTTCATGCAATACTCGAGTATTGCATGAAGAAACCACCGTTTTTG-3'	Fasmac Co., Ltd.	N/A
sh-CD59a-R: 5'-AATTCAAAAACGGTGGTTTCTTCATGCAATACTCGAGTATTGCATGAAGAAACCACCG-3'	Fasmac Co., Ltd.	N/A
sh-CD59a-control-F: 5'-CCGGGATGACTAGTCGTTATGCTCTCTCGAGAGAGCATAACGACTAGTCATCTTTTTG-3'	Fasmac Co., Ltd.	N/A
sh-CD59a-control-R: 5'-AATTCAAAAAGATGACTAGTCGTTATGCTCTCTCGAGAGAGCATAACGACTAGTCATC-3'	Fasmac Co., Ltd.	N/A
sgRNA for CRISPR/Cas9 mediated zyxin KO (targeting sequence: 5' TACGCCCCGCAGAAGAAGTT 3')	Invitrogen	Cat# CRISPR865844_SGM
Forward primer for genome sequencing of zyxin: 5' CCGCTCCTTGTATGGTCTGG 3'	Fasmac Co., Ltd.	N/A
Reverse primer for genome sequencing of zyxin: 5' CAAATTCCCGAAACGACTGC 3'	Fasmac Co., Ltd.	N/A
Software and algorithms		
HSR v2.3.1.0	Hamamatsu Photonics	https://www.hamamatsu.com/jp/en.html
MCR v1.2.0.0	Hamamatsu Photonics	N/A
PFV v3.6.6.0	Photron	https://www.photron.co.jp

LabVIEW 2018 v18.0.1f4	National Instruments	RRID:SCR_014325 (https://www.ni.com/en-us.html)
MetaMorph v7.10.1.161	Molecular Devices	RRID:SCR_002368 (https://www.moleculardevices.com)
NIS elements AR v5.20.2	Nikon	https://www.microscope.healthcare.nikon.com/products/software/nis-elements
ImageReader	Fuji Film	N/A
iBright Imaging Systems v1.5.0	Themo Fisher Scientific	RRID:SCR_017632
Visual Studio Community 2019 v.16.1.4	Microsoft	https://visualstudio.microsoft.com
MatLab 2019a v9.6.0	MathWorks	RRID:SCR_001622 (https://www.mathworks.com)
ImageJ (Fiji) v2.1.0	Schindelin et al.[151]	RRID:SCR_002285 (https://imagej.net/software/fiji/)
ThunderSTORM (ImageJ plug-in)	Ovesný et al.[152]	RRID:SCR_016897 (https://zitmen.github.io/thunderstorm/)
ilastik v1.3.3	Berg et al.[153]	RRID:SCR_015246 (https://www.ilastik.org)
SR-Tesseler v1.0.0.1	Levet et al.[40]	https://github.com/flevet/SR-Tesseler
Photoshop CC 2021 v22.4.2	Adobe	RRID:SCR_014199 (https://www.adobe.com)
Illustrator CC 2021 v.24.3	Adobe	RRID:SCR_010279 (https://www.adobe.com)
Origin 2017 v.b9.490.220	Origin Lab	RRID:SCR_014212 (https://www.originlab.com)
R studio v1.2.1335	R studio	RRID:SCR_000432 (https://www.rstudio.com)
BioRender	BioRender corp.	https://help.biorender.com/hc/en-gb
Excel v16.51	Microsoft	https://www.microsoft.com/en-us/microsoft-365/excel
Other		
Mini Protean Tetra Cell	Bio-Rad	Cat# 1658000JA

EXPERIMENTAL MODEL AND SUBJECT DETAILS

Mice

Female BALB/cAJcl-*Foxn1*^{nu} (nude) mice (6–8 weeks old) were purchased from CLEA Japan,

Inc. (BALB/cAJcl-*nu/nu*). All mice were maintained under specific pathogen-free conditions. All animal procedures were approved by the Animal Care and Use Committee at Okinawa
1330 Institute of Science and Technology Graduate University (OIST; approval no. 2022-362-2).

Cells

T24 cells (a kind gift from Masahiro Sokabe, Nagoya University),[128] HeLa cells (RIKEN Cell Bank), and CHO-K1 cells (Dainippon Pharma Co., Ltd.) were cultured in Ham's nutrient
1335 mixture F12 (Sigma-Aldrich, N6658) supplemented with 10% (vol/vol) fetal bovine serum (FBS; Gibco, 10270-106, Lot#: 42G7281K), 100 U/ml penicillin, and 100 μg/ml streptomycin (Nacalai Tesque, 26253-84). The talin1 and 2 double knockout mouse embryonic fibroblasts (talin-dKO MEFs) and talin2-KO MEFs (kind gifts from Reinhard Fässler, Max Planck Institute of Biochemistry),[19] the zyxin-KO MEF line (a kind gift from
1340 Mary C. Beckerle, University of Utah),[22] control MEF lines 1-3 (kind gifts from Noboru Mizushima, University of Tokyo), control MEF line 4 (a kind gift from Ryusuke Kuwahara, OIST), NIH3T3 cells (a kind gift from Makoto Kinoshita, Nagoya University),[129] and MDA-MB231 cells (American Type Culture Collection, ATCC) were cultured in Dulbecco's modified Eagle's minimum essential medium (DMEM; Sigma-Aldrich, D0822) supplemented
1345 with 10% (vol/vol) FBS, 100 U/ml penicillin, and 100 μg/ml streptomycin. RKO cells (ATCC) were cultured in Eagle's minimum essential medium (MEM; Gibco, 11095080) supplemented with 10% (vol/vol) FBS, 100 U/ml penicillin, and 100 μg/ml streptomycin. Mouse embryonic stem cells (mESCs; clone E14tg2a; RIKEN Cell Bank)[154] were cultured on gelatin-coated dishes in DMEM supplemented with 15% (vol/vol) embryonic stem-cell
1350 qualified FBS (Gibco, 16141079), 1x MEM non-essential amino acids solution (Gibco, 11140050), 1 mM sodium pyruvate (Gibco, 11360070), 55 μM 2-mercaptoethanol (Gibco, 21985023), 100 U/ml penicillin, 100 μg/ml streptomycin, and 10^3 U/ml mouse leukemia inhibitory factor (LIF; Millipore), without feeder cells.[155] The identities of the T24 and HeLa cell lines were authenticated by PowerPlex16 STR (contracted to Promega). All cells were
1355 confirmed to be mycoplasma-free using a Mycoplasma PCR Detection Kit (Beyotime Biotechnology) and VenorGeM Mycoplasma Detection Kit (Minerva Biolabs).

METHOD DETAILS

1360

cDNA construction

Plasmids were constructed using standard molecular biology techniques and verified by Sanger sequencing. All plasmids used in this study are listed, and the complete sequence information in GenBank format is available in Data S1. The cDNAs encoding SNAPf, Halo7, mGFP, and mCherry were obtained from New England Biolabs, Promega, and Clontech, respectively. The cDNA encoding mEos3.2 was generated by introducing three point mutations, I102N, H158E, and Y189A, into the mEos2 plasmid, a kind gift from Loren L. Looger (Janelia Research Campus).[108,134,156] The cDNAs encoding deletion mutants of RIAM, VASP, and zyxin were generated by PCR using designed primers. To construct cDNAs encoding phosphomimetic and phosphodeficient mutants of zyxin and VASP, all possible phosphorylation sites were identified by PhosphoSitePlus (https://www.phosphosite.org, 34 sites for zyxin and 27 sites for VASP). All phosphorylatable serine, threonine, and tyrosine residues were replaced with glutamic acid for phosphomimetic mutations, and with alanine, alanine, and phenylalanine, respectively, for phosphodeficient mutations. The mutated cDNAs were custom synthesized by Gene Universal. The cDNAs encoding mScarlet-I,[137] domain 4 from perfringolysin O with the D434S mutation (D4H),[149,150] and ostreolysin A with the E69A mutation (OlyA [E69A])[29] were custom synthesized by Sangon Biotech (Shanghai, PRC).

The cDNAs encoding human talin1, human zyxin, human VASP, human vinculin, human PIK3CA, human MARCKS, human Akt, and human JAK1 were purchased from Kazusa DNA Research Institute. The cDNAs encoding human α-actinin and human filamin A were purchased from Allele Biotechnology. The cDNAs encoding human paxillin isoform alpha[127] and rat Thy1[144] were cloned from the WI38 cell line and the rat brain, respectively.

The following cDNAs were kind gifts: mouse FAK from Caroline H. Damsky (University of California, San Francisco);[138] human RIAM from Chinten J. Lim (University of California, San Diego, Addgene);[139] human β3 integrin from Jonathan C. Jones (Northwestern University);[140] rat N-WASP from Jack Taunton (University of California, San Francisco);[141] mouse PIP5KIγ from Richard A. Anderson (University of Wisconsin);[142] human CD59 from Masahide Tone (University of Oxford);[143] human PDGFR-β from Addgene (originated from William Hahn (Broad Institute of MIT) and David Root (Harvard University));[145] rat PLCγ1 from Matilda Katan (Cancer Research UK Centre);[146] mouse PLCβ1 from Katsuhiko Mikoshiba (ShanghaiTech University);[147] and human CD47 from Eric

C. Brown (Genentech);[148] probes for PI(4)P, PI(3,4)P_2, PI(4,5)P_2, and PI(3,4,5)P_3 from
1395 Toshiki Itoh (Kobe University);[32] a probe for phosphatidylserine from Tomohiko Taguchi (Tohoku University);[30,31] CIBN and CRY2-5ptase from Pietro de Camilli (Yale University, Addgene);[33] membrane-optoDroplet from Jared E. Toettcher (Princeton University, Addgene);[69] tag-FAK-B and binder from Klaus M. Hahn (University of North Carolina).[67]

A five-amino acid linker sequence (Ser-Gly-Gly-Gly-Gly) was inserted between the
1400 target protein and mGFP, mCherry, and mScarlet-I, and a 15-amino acid linker ((Ser-Gly-Gly-Gly-Gly)$_3$) was inserted between the target protein and SNAPf, Halo7, and mEos3.2.

The sequences encoding these proteins were subcloned into the following vectors: pEGFP and pmCherry (Clontech), pcDNA3.1(+)-Hygro and pcDNA3.1(+)-Zeo (Invitrogen), pET26B (Novagen), pOStet15T3 (an episomal Epstein–Barr virus-based vector carrying
1405 tetracycline-regulated expression units, including the transactivator (rtTA2-M2) and the tetO sequence [Tet-on vector]) from Yoshihiro Miwa (University of Tsukuba);[157] and pPBpuro (a PiggyBac-based custom vector containing the terminal repeat sequence and a strong composite promoter consisting of chicken β-actin promoter, CAG promoter with an artificial intron, and CMV immediate early promoter) and pCMV-mPBase from Michiyuki
1410 Matsuda (Kyoto University).[133]

Cell transfection

Cells were transfected with plasmid vectors by electroporation, using a Lonza 4D-Nucleofector according to the manufacturer's instructions. The following solutions and
1415 programs were used: for T24 and NIH3T3 cells, SF solution and program EN138; for HeLa cells, SE and CN114; for CHO-K1 cells, SF and DT133; for MDA-MB231 cells, SE and EW113; for RKO cells, SE and DN100; for talin-dKO MEFs, SE and DS150; for other MEFs, SF and CZ167; and for mESCs, SF and CG104.

For the generation of stable cell lines expressing selected proteins, cells were
1420 transfected with an expression plasmid. When using the pPBpuro expression vector (PiggyBac-based vector), pCMV-mPBase was co-transfected. Two days after transfection, selection was initiated using appropriate antibiotics. G418 was used at 800 μg/mL for T24 cells, 1,000 μg/mL for MEFs, 5,000 μg/mL for MDA-MB231 cells, and 2,000 μg/mL for RKO cells. Puromycin was used at 0.5 μg/mL for T24, RKO, and MDA-MB231 cells, and at 1
1425 μg/mL for MEFs. Hygromycin B was used at either 500 or 1,000 μg/mL for MEFs, and zeocin was used at 500 μg/mL for MEFs. After one week of selection, cell clones were

established either by limiting dilution using 96-well plates or by fluorescence-activated cell sorting (FACS) using an Aria II (BD Biosciences) to isolate populations with appropriate expression levels. Expression levels of the introduced constructs were examined by western blotting and immunofluorescence microscopy. The established stable cell lines were subsequently maintained in culture medium containing the corresponding selection antibiotics.

For the expression of CRY2-fused proteins, transfected talin1/2-dKO MEFs were first incubated in complete growth medium at 37°C for 2 h for post-transfection recovery and then cultured at 33°C for 2 days to promote protein folding, followed by an incubation at 37°C for 3 h immediately prior to microscope observations.

To generate malignantly transformed MEF lines for xenograft studies, zyxin-KO MEFs (2×10^4 cells) were transfected with a lentivirus vector encoding the human K-Ras G12V mutant (GenTarget, 5×10^5 inclusion-forming unit). Two days after infection, cells were selected with 5 μg/ml blasticidin and continuously cultured under selection for one month to ensure complete transformation.[158] Because RFP is fused to the blasticidin resistance gene, K-Ras (G12V) expression levels could be monitored by RFP fluorescence. To normalize Kras (G12V) expression, we selected the clones exhibiting comparable RFP fluorescence intensities.

Cell culture for microscope observations

Cells were plated on glass-bottom dishes (12-mm diameter glass window; No.1S; Iwaki, 3971-035) pre-coated with fibronectin (FN; Sigma-Aldrich). For coating, 100 μL of FN (10 μg/mL in phosphate buffered saline; PBS) was placed onto the glass surface and incubated at room temperature for 30 min. PBS contained 137 mM NaCl, 8.1 mM $NaHPO_4$, 2.7 mM KCl, and 1.5 mM KH_2PO_4 (pH 7.4). After seeding, cells were cultured in the complete growth medium for 24–48 h before microscopy.

Lentiviral production and infection for shRNA gene knockdown

Mice possess two homologous CD59 genes, CD59a and CD59b. Since CD59a is broadly expressed in most tissues, whereas CD59b is restricted to germ cells,[159] gene knockdown was performed against CD59a for transformed MEFs in this study.

The oligonucleotide pair targeting mouse CD59a mRNA (5′-CCGGCGGTGGTTTCTTCATGCAATACTCGAGTATTGCATGAAGAAACCACCGTTTTTG-3′ and 5′-

1460 AATTCAAAAACGGTGGTTTCTTCATGCAATACTCGAGTATTGCATGAAGAAACCACCG-3′) and its scrambled control pair (5′-CCGGGATGACTAGTCGTTATGCTCTCTCGAGAGAGCATAACGACTAGTCATCTTTTTG-3′ and 5′-AATTCAAAAAGATGACTAGTCGTTATGCTCTCTCGAGAGAGCATAACGACTAGTCATC-3′) were cloned into the pLKO1-hygro vector (Addgene; deposited by Robert A. Weinberg, MIT) at
1465 the AgeI – EcoRI site. The shRNA constructs were co-transfected with packaging plasmids (Lentiviral High Titer Packing Mix; Takara) into Lenti-X 293T cells (Takara), using TransIT-293 (Mirus). At 24 h after transfection, the medium was replaced with fresh complete growth medium (DMEM + 10%FBS). At 48 h after transfection, the lentiviral supernatant was harvested and filtered through a 0.45-µm Millex filter (Millipore). The lentiviral
1470 supernatant was concentrated 50x in complete growth medium, using a Lenti-X Concentrator (Takara), and the concentrated lentiviral solution was stored at -80ºC until use.

One day before infection, zyxin KO transformed MEFs were plated in 12-well plastic plates at 2.5 x 10^4 cells per well in 1 mL medium. The concentrated lentiviral solution (4
1475 µL) was added to each well, and the cells were incubated for 24 h. The medium was then replaced with fresh complete growth medium, and the cells were further incubated for 48 h. After selection in medium containing 1 mg/mL hygromycin for one week, FACS was used to isolate a cell population with low CD59a expression. For sorting, a mouse anti-CD59a antibody (clone mCD59.3; BioLegend) was used at 10 µg/ml. The CD59a
1480 expression levels were quantified by western blotting.

CRISPR/Cas9-mediated knockout of zyxin in MDA-MB231 and RKO cells

The synthetic guide RNA (sgRNA) targeting ZYX (Invitrogen, targeting sequence: 5′ TACGCCCCGCAGAAGAAGTT 3′) and Cas9 protein (Invitrogen, A36498), 38 pmol each, were
1485 mixed in 20 µL of SE solution (Lonza) and incubated for 30 min at RT. Approximately 2 x 10^5 cells were resuspended in this solution, and the sgRNA/Cas9 complex was delivered by electroporation using a Lonza 4D-Nucleofector (program EW113 for MDA-MB231 cells and program DN100 for RKO cells). Two days after electroporation, clones were isolated by limiting dilution in 96-well plates. Clones were validated by western blotting and amplicon
1490 sequencing of the target genomic locus, using the primers 5′ CCGCTCCTTGTATGGTCTGG 3′ (forward) and 5′ CAAATTCCCGAAACGACTGC 3′ (reverse) with a minimum of 24 sequencing reads per clone.

Cell stimulation

1495 CD59 and Thy1 were activated by polystyrene beads coated with the respective monoclonal antibodies. Mouse anti-CD59 and mouse anti-Thy1 monoclonal antibodies were purified from the culture media of hybridoma MEM43/5 cells (a kind gift from Vaclav Horejsi, Institute of Molecular Genetics, Czech Academy of Sciences)[130] and hybridoma OX7 cells (European Collection of Cell Cultures),[131,132] respectively. The carboxylate-modified yellow-green or 1500 dark-red fluorescent 40-nm polystyrene beads (Molecular Probes, final concentration, 0.4 μM) were functionalized by an incubation at RT for 10 min in activation solution, containing 2 mM 1-ethyl-3-(3-dimethylaminopropyl)carbodiimide (EDC, Pierce), 4 mM sulfo-N-hydroxysuccinimide (sulfo-NHS, Pierce), and 150 mM NaCl, buffered with 0.1 M 2-(N-morpholino)ethanesulfonic acid (MES; pH 5.5). A 9 μL aliquot of antibody solution (1 mg/ml 1505 in PBS) was mixed with 3 μL of activated beads, 3 μL of borate-buffered saline (150 mM NaCl buffered with 0.5 M borate, pH 8.0), and 1 μL of 0.4 M NaOH. After an incubation at RT for 1 h, the coupling reaction was stopped by adding 7.5 μL of 300 mM glycine and 1 μL of 5% polyethylene glycol (mean molecular weight 20,000, PEG20K; Sigma-Aldrich) in PBS, followed by further incubation at RT for 5 min. The mixture was ultracentrifuged at 50,000 1510 rpm for 15 min. The antibody-coated beads were resuspended in 1 mL PBS containing 0.1% PEG20K, ultracentrifuged again, and finally resuspended in Hanks' balanced salt solution (HBSS; Nissui, 05905) buffered with 2 mM TES (Dojindo, 348-08371) at pH 7.4 (observation medium; T-HBSS) containing 2% bovine serum albumin (BSA, Sigma-Aldrich) and 0.1% PEG20K. Immediately before use, the bead suspension was sonicated for 5 min and 1515 centrifuged at 15,000 rpm for 10 min. Cells were first incubated in T-HBSS containing 0.5% BSA and 0.1% PEG20K, after which the bead suspension was added at a final concentration of 2 μM or 20 nM. All observations were completed within 10 min after bead addition to minimize the effects of internalization.

For cell stimulation experiments using epidermal growth factor (EGF) and platelet-1520 derived growth factor (PDGF), cells were serum-starved in FBS-free medium for 3-12 h. Prior to cell stimulation and microscopy, the culture medium was replaced with T-HBSS, and cells were stimulated with 20 nM human recombinant EGF (Wako), and 20 nM or 20 pM human recombinant PDGF-BB (Pepro Tech). All microscopy observations were completed within 5 min after stimulation. When simultaneous stimulations with anti-CD59

1525 beads and PDGF were performed, the bead buffer (T-HBSS containing BSA and PEG20K) was used, and all observations were completed within 10 min after stimulation.

Cell treatments with various reagents

Kinase activities were inhibited by incubating cells in T-HBSS containing 10 μM PP2 1530 (Selleckchem; Src family kinase inhibitor)[160] or 10 μM PF573228 (Cayman Chemical; focal adhesion kinase inhibitor)[161] at 37°C for 10 min.

Partial actin depolymerization was performed by incubating cells in T-HBSS containing 100 nM latrunculin A (Wako), 500 nM cytochalasin D (Cayman Chemical), or 10 μM Y27632 (ChemScene) at 37°C for 10 min. Partial depletion of cholesterol was achieved by incubating 1535 cells in 4 mM methyl-β-cyclodextrin (MβCD; Sigma-Aldrich) in T-HBSS at 37°C for 30 min or in 60 μg/ml saponin (Nacalai Tesque) in T-HBSS on ice for 15 min.[157] Replenishment of cholesterol was performed by incubating cholesterol-depleted cells in 10 mM MβCD-cholesterol complex (1:1 mol/mol; Sigma-Aldrich) in T-HBSS at 37°C for 30 min.[157] Partial depletion of PI(4,5)P_2 from the PM was performed by incubating cells with either 10 μM 1540 ionomycin (Wako) in T-HBSS at 37°C for 5 min,[162] 1 μM phenylarsine oxide (Tokyo Chemical Industry) at 37°C for 3 h, or 50 μM quercetin (Sigma-Aldrich) at 37°C for 3 h.[34,163]

To inhibit interactions mediated by intrinsically disordered regions (IDRs), cells were first mildly permeabilized with 1% Tween 20 in T-HBSS at RT for 10 min, and then treated with T-HBSS containing 5% 1,6-hexanediol (Wako) on the microscope stage during 1545 imaging.[164] All imaging experiments were completed within 10 min. For *in vitro* experiments, 1,6-hexanediol was added to a final concentration of 10%.

Western blotting

For cultured cell samples, ice-cold radio immunoprecipitation assay (RIPA) buffer was used 1550 (350 μL for 60-mm plastic dish). The RIPA buffer consisted of 150 mM NaCl, 5 mM ethylenediaminetetraacetic acid (EDTA; Dojindo, 345-01865), 1% NP-40 (Wako, 141-08321), 1% sodium deoxycholate (Nacalai Tesque, 08805-72), 0.1% sodium dodecyl sulfate (SDS; Wako, 191-07145), and 1x protease inhibitor cocktail (Nacalai Tesque), buffered with 50 mM tris(hydroxymethyl)aminomethane (Tris)-HCl (pH 7.4). For the Akt phosphorylation 1555 assay, 1x phosphatase inhibitor cocktail (Nacalai Tesque) was included. The RIPA buffer was added to cells at ≈80% confluency in a 60-mm plastic dish, and cells were kept on ice for 5 min. Lysates were collected using a cell scraper and centrifuged at 15,000 rpm for 20 min.

For tumor tissue samples, homogenization was performed by two cycles of freezing and thawing, pestle grinding, and sonication (50% duty for 5 min on ice) in RIPA buffer. Insoluble fractions were removed by centrifugation at 15,000 rpm for 1 h.

The supernatant (300 μL) was mixed with 100 μL of 4x Laemmli sample buffer (8% SDS, 0.12% bromophenol blue, 40% glycerol, and 400 mM dithiothreitol (DTT), buffered with 200 mM Tris-HCl, pH 6.8) and boiled for 5 min. For CD59 detection, samples were prepared under non-reducing conditions (without DTT and boiling), because the anti-CD59 antibody only binds to non-reduced proteins.

Samples (2-10 μL; 1-2 μg of total protein per lane) were loaded onto precast 4-20% gradient polyacrylamide gels (Bio-Rad) and electrophoresed at a constant voltage of 200 V for 25 min (CD59) or 35 min (others) using a Mini Protean Tetra Cell (Bio-Rad), in Tris-glycine running buffer (25 mM Tris-HCl, 190 mM glycine, and 0.1% SDS). Direct addition of 4x Laemmli buffer to the specimens yielded comparable results but increased the background; therefore, the specimens were first solubilized with RIPA buffer.

Proteins were transferred to polyvinylidene fluoride (PVDF) membranes (0.45 μm pore size) by semi-dry transfer using a Trans-Blot Turbo (Bio-Rad, mixed MW protocol) with the PVDF transfer pack (Bio-Rad) for zyxin, VASP, Akt, FAK, and JAK1. For CD59, proteins were transferred to PVDF membranes (0.2 μm pore size; FluoroTransW, Pall) using the transfer buffer (25 mM Tris-HCl, 190 mM glycine, and 20% methanol) at RT at a constant voltage of 50 V for 10 min (Trans-Blot Turbo). For talin, wet transfer to the PVDF membrane (Immobilon-P, Millipore) was performed using the same transfer buffer at 4ºC at a constant voltage of 100 V for 1 h (Mini Protean Tetra Cell).

Membranes were blocked with Blocking One (Nacalai Tesque) for 30 min at RT and washed with Tris-buffered saline (TBS; 137 mM NaCl and 2.7 mM KCl buffered with 25 mM Tris-HCl, pH 7.4) containing 0.1% Tween 20 (TBS-T). The blocked membranes were incubated with primary antibodies at RT for 60 min: mouse anti-talin1 (clone 93E12, Abcam, 0.5 μg/mL), rabbit anti-zyxin (B71, Millipore, 1:4,000), rabbit anti-GFP (ProteinTech, 0.5 μg/mL), rabbit anti-VASP (clone 9A2, Cell Signaling Technology, 21 ng/mL), rabbit anti-Akt (Cell Signaling Technology, 17 ng/mL), rabbit anti-phospho-Akt (pS473, clone D9E, Cell Signaling Technology, 48 ng/mL), rabbit anti-FAK (Cell Signaling Technology, 31 ng/mL), rabbit anti-phospho-FAK (pY397, clone D20B1, Cell Signaling Technology, 8 ng/mL), rabbit anti-JAK1 (Cell Signaling Technology, 1:1,000), rabbit anti-phospho-JAK1 (pY1034/1035, Cell Signaling Technology, 82 ng/mL), mouse anti-CD59a (clone mCD59.3, BioLegend:, 1 μg/mL)

and mouse anti-GAPDH (ProteinTech, 10-500 ng/mL). Membranes were then incubated with secondary antibodies at RT for 30 min: horseradish peroxidase (HRP)-conjugated goat anti-mouse immunoglobulin G (IgG; Invitrogen, 0.5 μg/mL) and HRP-conjugated goat anti-rabbit IgG (Invitrogen, 0.5 μg/mL).

Membranes were incubated with Western BLoT Hyper HRP Substrate (Takara) for chemiluminescence detection and imaged using an LAS-3000 (Fuji Film, high sensitivity mode) or iBright FL1500 (Thermo Fischer Scientific; 2x2 binning, 2.0x zoom). Quantification was performed using ImageJ, with signal intensities normalized to GAPDH. For tumor tissues, where GAPDH intensities varied, normalization was based on total protein amounts measured from Coomassie Brilliant Blue R-250 (CBB R-250)-stained gels. For CD59 detection under non-reducing conditions, GAPDH could not be used (the anti-GAPDH antibody binds only to reduced proteins); therefore, normalization was performed using CBB R-250–stained gels.

For phosphorylation analysis, membranes were first probed and imaged for phosphorylated proteins, and then stripped and reprobed with antibodies against total protein. For Akt and JAK1, stripping was performed in buffer consisting of 2% SDS, 100 mM 2-mercaptoethanol, and 62.5 mM Tris-HCl (pH 6.7) at 50°C for 20 min. For FAK, stripping was performed with WB Stripping Solution (Nacalai Tesque) at RT for 30 min.

Cell attachment assay

Cells at ≈80% confluency in 100-mm plastic dishes were detached with freshly prepared trypsin solution (0.25% trypsin and 1 mM EDTA in PBS) at RT for 3 min. After brief centrifugation (1,000 rpm for 3 min), cells were resuspended in the complete growth medium, and cell numbers were determined using a hemocytometer. The cell concentration was adjusted to 3 x 10^4 cells/mL, and cells were incubated at 37ºC, 5% CO_2 for 30 min to allow recovery after detachment. Subsequently, 1 mL of the cell suspension was dispensed into each FN-coated well of a 12-well plastic plate, and the plate was incubated at 37ºC, 5% CO_2 for 5 min. Wells were gently washed twice with T-HBSS, and the attached cells were imaged using a Zeiss Primovert Photo inverted phase-contrast microscope. The number of attached cells was quantified using ImageJ.

Immunofluorescence labeling

Cultured cells on FN-coated glass-base dishes were fixed with cold methanol (-20ºC) for 5

min for talin staining or with 4% paraformaldehyde at RT for 1 h for zyxin staining. Fixed
1625 cells were treated sequentially at RT with 100 mM glycine for 15 min, 0.1% Triton X-100 for 5 min, and 1% BSA for 1 h. All solutions were prepared in PBS containing 0.1% Tween 20 (PBS-T). Cells were immunostained by sequential 1-h incubations with primary and secondary antibodies at RT, with three PBS-T washes after each incubation.

The antibodies used were: mouse anti-talin1 (clone 97H6, Bio-Rad, 1 μg/mL), rabbit
1630 anti-zyxin (B71, Millipore, 1:600), Rhodamine Red-X-conjugated donkey anti-mouse IgG (Jackson ImmunoResearch, 1 μg/mL), and Rhodamine Red-X-conjugated donkey anti-rabbit IgG (Jackson ImmunoResearch, 1 μg/mL).

Fluorescence labeling of molecules

1635 To fluorescently label the SNAPf and Halo7 tags conjugated to target proteins expressed in cells, the cells were incubated at 37ºC in complete growth medium containing membrane-permeable fluorescent ligands. For SNAPf, cells were incubated for 60 min with 50 nM SNAP-tetramethylrhodamine (TMR) star (New England BioLabs). For Halo7, cells were incubated for 30 min with 20 nM TMR-Halo linker (Promega), 20 nM SaraFluor650T Halo linker (SF650;
1640 Goryo Chemical), or 100 nM JF646 Halo linker (Promega). Labeling efficiencies were estimated to be 66 ± 1.8% for SNAPf, 88 ± 2.2% for Halo7, and 76 ± 2.3% for mGFP, using the monomer reference proteins mGFP-CD47-SNAPf and mGFP-CD47-Halo7 (SNAPf and Halo7 tags located in the cytoplasm). Using the 15-amino acid linker ((Ser-Gly-Gly-Gly-Gly)$_3$) employed here, the labeling efficiencies were generally independent of the host target
1645 proteins.[20,165] Unless otherwise noted, the Halo7 and SNAPf tags were labeled with SaraFluor650 Halo-ligand and SNAP-TMR star, respectively.

Single fluorescent-molecule imaging and analysis

All single-molecule observations were performed at 37°C, using microscopes enclosed in
1650 home-built environmental chambers. Fluorescently labeled molecules in cells were excited by total internal reflection (TIR) illumination for those on the basal PM or by oblique-angle illumination for those on the apical PM, using an objective-lens-type TIR illumination system constructed on Olympus IX83 and Nikon TiE inverted microscopes equipped with 100x/1.49 NA objective lenses (UApoN100XTIRF and ApoTIRF100XC, respectively). Multi-color
1655 fluorescence images were separated into the three detection arms of the microscope by a dichroic mirror (Chroma, ZT561rdc-UF3 and ZT640rdc-UF3). Each detection arm was

equipped with band-pass filters (Chroma, ET525/50m, ET600/50m, or ET700/75m), and images were recorded using a two-stage microchannel plate intensifier (Hamamatsu Photonics, C9016-02MLP24) lens-coupled to a scientific complementary metal oxide semiconductor (sCMOS) camera (ORCA-Flash ver4.0 V2 plus; Hamamatsu Photonics, C11440-22CU). The final magnifications were 133x (50 nm/pixel) and 100x (65 nm/pixel). All instruments in the microscope station were controlled by in-house LabVIEW-based software.

For single molecule observations with oblique illumination, the incident excitation laser powers at the sample plane were 0.29 μW/μm^2 for 488 nm (mGFP; Coherent, OBIS 488-100 LS), 0.21 μW/μm^2 for 561 nm (TMR; Coherent, OBIS 561-100 LS), and 0.37 μW/μm^2 for 642 nm (SF650 and JF646; Omicron, LuuXPlus 640-140). For TIR illumination, very shallow angles and twice the incident laser powers were used. Under these conditions, the photobleaching lifetimes for fluorophores on the apical PM with oblique illumination (and the basal PM with TIR illumination) were: mGFP, 0.61 ± 0.02 s (0.74 ± 0.02 s); SNAPf-TMR, 3.65 ± 0.15 s (3.68 ± 0.18 s); Halo7-TMR, 8.87 ± 0.47 s (9.50 ± 0.48 s); Halo7-SaraFluor650, 12.69 ± 0.57 s (14.38 ± 0.53 s); and Halo7-JF646, 11.12 ± 0.62 s (12.01 ± 0.54 s). For GEM cluster observations, the laser powers were reduced by a factor of three compared to those used for single-molecule observations.

Individual fluorescent spots were identified and tracked using an in-house computer program, as described previously.[23,108,121,156] Multi-color image superimposition was performed as described previously.[166]

For visualization of GEM, fluorescently labeled talin or zyxin was imaged at single-molecule sensitivity (with laser power reduced by a factor of three compared to standard single-molecule observations) at 30 frames/s. Images were rolling-averaged over 30 frames and background-subtracted using a rolling-ball algorithm with a 30-pixel (1.5-μm) radius. Talin and zyxin clusters were identified using an in-house computer program originally developed for detecting single-molecule Gaussian spots.[23,108,121,156] Copy number per cluster (GEM size) was determined by comparing cluster spot intensities with those of a monomer control molecule, the tag protein fused to a C-terminal K-Ras CAAX motif (farnesylated tag proteins).

Transient-immobilization events, termed Temporary Arrest of LateraL diffusion (TALL[127,167]), were detected in single-molecule trajectories using a previously described algorithm[168], as modified in subsequent studies.[127,167] The detection circle radius was set to

200 nm, and the residency-time threshold was set to 5 frames (0.167 s). Cluster lifetimes and molecular dwell lifetimes at GEM were not corrected for photobleaching, because the photobleaching lifetimes of the probes were much longer than the observed cluster lifetimes and molecular dwell lifetimes under the employed imaging conditions.

Colocalization duration analysis

Colocalization of two fluorescent molecules was defined as an event in which two molecules are localized within 200 nm of each other, as described previously.[166,169] The duration of each colocalization event was measured, and the distribution of colocalization durations was obtained from all detected events. We found that the distributions were best fitted by the sum of two exponentials, based on both the Akaike and Bayesian information criteria. The shorter decay component represents the incidental colocalization lifetime (τ_1; colocalization without molecular binding), whereas the longer decay component represents the molecular binding duration (τ_2).[6,169]

Colocalization index analysis

To quantitatively measure the colocalization of single molecules with GEM (talin and zyxin clusters), whose apparent sizes were close to the diffraction limit and therefore indistinguishable from single-molecule spots, we employed a "colocalization index" based on a pair cross-correlation analysis of two-color single-molecule movies (e.g., green and red),[21,124,169] as illustrated in Figure S1H. Briefly, (1) a region of interest (ROI) was selected, and the distances between all pairs of green and red fluorescent spots in the ROI were measured in each video frame; this procedure was repeated for all frames. (2) The distribution of pair counts, $R(r)$, was plotted as a function of the distance, r. The normalization factor, $N(r)$, was computed using the fast Fourier transform and the inverse fast Fourier transform.[21,124] (3) The cross-correlation function was calculated as $C(r) = R(r)/N(r)$. (4) The colocalization index was defined as the ratio of the $C(r)$ between 0 and 50 nm to the $C(r)$ between 450 and 500 nm. In the absence of significant colocalization, the index equals 1, whereas increasing colocalization yields higher values. Control data without correlations between green and red spots were generated by shifting each track in the image by 1 μm in random directions.

PALM observation and analysis

Cells expressing the proteins fused to mEos3.2 were chemically fixed prior to PALM observations. Briefly, cells were initially fixed with 0.3% (vol/vol) glutaraldehyde in
1725 cytoskeleton buffer (150 mM NaCl, 5 mM EGTA, 5 mM glucose and 5 mM $MgCl_2$, buffered with 10 mM MES, pH 6.1) containing 0.25% (v/v) Triton X-100 for 1 min, followed by post-fixation with 2% (vol/vol) glutaraldehyde in the same solution for 15 min.[170,171] Cells were then incubated with freshly prepared 0.1% (wt/vol) sodium borohydride for 7 min, to quench unreacted aldehydes. After replacing the cytoskeleton buffer with T-HBSS, the fixed cells
1730 were imaged at 37°C using a home-built PALM station,[108,156] built on an Olympus IX83 microscope.

Samples were illuminated in the TIR or oblique-angle mode, using a 405-nm activation laser (Cobolt, 06-MLD 405-100; increased from 1.5 to 78 nW/μm^2 at the sample plane following the Fermi photoactivation scheme [t_F = 162, T = 16.2 s]),[172] a 561-nm excitation
1735 laser (MPB Communications, Fiber 560-20000; 12.4 μW/μm^2), and an additional weak 488-nm laser to suppress the long-lived dark state[173] (Coherent, Sapphire 488-300 CW; 0.164 μW/μm^2). PALM data were acquired at 60 Hz for 14,560 frames with an image size of 512 x 512 pixels, using a high-speed camera system (Photron, mini AX200-II) as described previously.[108,156] The final magnification was 250x (80 nm/pixel).

1740 Spot detection was performed using the ThunderSTORM plugin in ImageJ[152] with Wavelet filtering (B-spline order = 3; scale = 2.0) and the local maximum method (peak intensity threshold = 30-50; connectivity = 8-neighborhood). Post-processing included removing duplicates (distance threshold = uncertainty) and drift correction (cross-correlation with 5 bins). Processed datasets were imported into the SR-Tesseler[40] for cluster
1745 analysis and image reconstruction. ROIs were selected in apical PM regions with good focus, and for the basal PM analyses, ROIs were selected from the regions without obvious IACs. Blinking and multi-ON frame detections were corrected using the detection cleaner function (photon/background size = 0.3; fixed maximal dark time = 200; intensity-to-photon ratio = 0.039; background value = 0.3).[173] Cluster contour detection was then performed using a
1750 Voronoï polygon density factor of 3.5 applied across the entire ROI.

Optogenetics

For the partial depletion of PI(4,5)P_2, CRY2 fused to mScarlet and 5-phosphatase-OCRL (mScarlet-CRY2-5PT) and CIBN fused to farnesylated mGFP (CIBN-mGFP-far; farnesylation
1755 for the localization on the PM cytoplasmic surface) were expressed in talin-rescued dKO

MEFs (used to determine the copy number of talin per GEM; Figure 2D). In the dark, CRY2 does not bind to CIBN. Upon blue light irradiation (488-nm laser epi-illumination of the entire cell; train of 200-ms pulses at 0.5 Hz for 30 s; 0.64 nW/μm^2; at the sample plane), light-activated CRY2 bound to CIBN on the PM, recruiting mScarletI-CRY2-5PT to the PM, and inducing PI(4,5)P_2 hydrolysis (Figure S3D). The PI(4,5)P_2 levels in the PM were monitored using a fluorescent probe consisting of two tandem PH domains of PLCδ fused to SNAPf (SNAPf-2xPH). After the blue light was turned off, CRY2 was slowly deactivated, leading to the dissociation of mScarlet-CRY2-5PT from the PM (Figure S3D). The phosphatase-dead D523G mutant of 5PT fused to mScarlet-CRY2-5PT served as a control.

To quantify PI(4,5)P_2 levels at the PM, cell boundaries were determined from the SNAPf-2xPH images using ilastik.[153] The outer and inner contours of the cell were then set at ± 1 μm from the cell boundary to define the PM region. Mean pixel intensities in the PM region (F_{PM}) and in the cytoplasm (F_{cyto}) were measured (Figure S3F). PI(4,5)P_2 levels decreased rapidly after blue light irradiation, and returned to baseline within 10 min after the 30-s irradiation was terminated. Single-molecule observations of talin clusters (GEMs) were performed before, immediately after, and 15 min after the blue light irradiation (Before, After, and Recovery in Figure S3H).

For artificial droplet formation,[68,69] cDNAs of optoFAK and optoLyn were generated by combining the sequences encoding the Src myristoylation signal peptide, the N-terminal IDR of FUS, fluorescent tag proteins (mGFP, Halo7, or SNAPf), CRY2, and either FAK or Lyn (with mutations in the N-terminal myristoyl/palmitoyl modification signals), and expressed in the cell (Figure S6A). In the dark, CRY2 does not form clusters. Upon blue light irradiation, light-activated CRY2 formed clusters via homotypic interactions (Figure S6B). The blue light intensity and pulse train were identical to those used for PI(4,5)P_2 depletion. Irradiation started 2 min before PDGF stimulation and continued during recording.

To detect FAK activation within droplets, the binder-tag system was used.[67] The SsrA peptide is inserted into the central region of FAK, where it becomes exposed in the active open conformation, allowing specific binding by the SNAPf-tagged SspB binder peptide (Figure S6F).

Confocal microscopy and FRAP

For live-cell confocal fluorescence imaging at 37ºC, we used a home-built spinning-disk confocal microscope based on an Olympus IX83 enclosed in a home-built environmental

chamber, equipped with a 60x or 100x objective (Olympus, PLXApo60XO or UApoN100XTIR),
1790 a confocal unit (Yokogawa CSU-W1), and an sCMOS camera (Hamamatsu Photonics, ORCA-Flash 4.0 V2 plus).

For in-cell FRAP, a Nikon A1R confocal microscope equipped with a stage-top incubator (Tokai-Hit, STXG-TIZWX-SET) was used at 37ºC with a recording rate of 0.5 Hz. The photobleached ROI was circular (≈1 μm diameter), and photobleaching was performed by
1795 illuminating the area with a 488- or 561-nm laser at 30% of the full laser power for 1 s.

For *in vitro* FRAP, purified proteins were diluted with observation buffer (150 mM NaCl and 0.5 mM tris(2-carboxyethyl)phosphine) [TCEP], buffered with 25 mM Tris–HCl, pH 7.4). After the addition of a final concentration of 1% PEG8K (Sigma-Aldrich, P5413), the solution was placed on the glass-bottom slide (Ibidi, 81507) and observed at 37ºC and 1 Hz using a
1800 Nikon spinning-disk confocal microscope, consisting of a Nikon TiE inverted microscope with a PlanApo 60x/1.40 objective lens (Nikon), a confocal unit (Yokogawa, CSU-X), an Andor Revolution SD System, an EM-CCD camera (Andor, iXon 888-U3ultra), and a stage top incubator (OkoLab). The bleached ROI was circular (≈1.5 μm diameter), and photobleaching was performed with a 488-nm laser (3.9 mW) for 0.5 s. Fluorescence recovery curves were
1805 background-corrected and normalized using ImageJ and analyzed as described previously.[174]

Cell volume measurement

Cells were transfected with a plasmid encoding SNAPf alone (without fusion proteins) and
1810 plated on FN-coated glass-bottom dishes. After 48 h, the expressed SNAPf proteins were labeled with SNAP-TMR Star, and the medium was replaced with 1:1,000 diluted NucSpot Live 650 (Biotium, 40082) in T-HBSS for nuclear staining. Without washing, whole-cell 3D images were acquired by Z-stack scanning (250-nm step size) using the home-built Olympus spinning-disk confocal microscope.

1815 Images were binarized in ImageJ, using Otsu's algorithm.[175] Whole-cell and nuclear volumes were determined from the binarized images of SNAPf and NucSpot Live 650, respectively, by counting the total voxels. Cytoplasmic volume was calculated as the whole-cell volume minus the nucleus volume.

1820 Measurements of intracellular Ca^{2+} concentrations

Cells were incubated with 20 μM CalBryte 590 (AAT Bioquest, 20700) in T-HBSS at 37ºC for

30 min, followed by three washes with T-HBSS. Cells were imaged at 37ºC using a home-built objective-lens-type TIRF microscope (Nikon TiE-based) equipped with a Plan Fluor 20x/0.50 objective lens (Nikon), with epi-illumination using a 561-nm laser (0.22 nW/μm^2 at the sample plane). Recordings were performed at 1 or 2 Hz. All observations were completed within 1 h after labeling.

Purification of protein probes for cholesterol and sphingomyelin

For the production of cholesterol and sphingomyelin probes, BL21 (DE3) *E. coli* competent cells (New England BioLabs, C2527) were transformed by heat shock with expression plasmids encoding Halo7-tag fused to D4H[149,150] and Halo7-tag fused to OlyA (E69A)[29]. Transformed cells were cultured at 37˚C in Luria-Bertani (LB) medium containing 50 μg/mL kanamycin with shaking until the optical density at 600 nm reached 0.4-0.6, and protein expression was induced with 0.6 mM isopropyl-β-D-thiogalactopyranoside (IPTG; Amresco) at 24ºC for 12 h. Cells were harvested by centrifugation at 7,000 rpm for 3 min, resuspended in lysis buffer (1% Triton X-100 and 300 mM NaCl, buffered with 20 mM Tris-HCl, pH 8.0, and supplemented with protease inhibitor cocktail; Nacalai Tesque), and lysed by agitation on ice for 20 min. Lysates were centrifuged at 12,000 rpm for 10 min, and the supernatants were filtered through a 0.45-μm Millex filter (Millipore). Proteins were purified by Ni-NTA agarose chromatography (1 mL bed volume; Sangon Biotech). Bound proteins were eluted sequentially with 10, 20, and 30 mM imidazole (10, 10, and 5 mL, respectively) in 150 mM NaCl buffered with 20 mM Tris-HCl (pH 8.0), followed by a final elution with 100 mM imidazole in 250 mM NaCl, 20 mM Tris-HCl, pH 8.0 (10 ml).

Eluted fractions were desalted and concentrated with an Amicon Ultra concentrator (10 kDa cutoff, Millipore) into 150 mM NaCl buffered with 20 mM 4-(2-hydroxyethyl)-1-piperazine ethanesulfonic acid (HEPES; pH 7.4). Protein concentrations were determined by the absorbance at 280 nm, using extinction coefficients of 1.02 and 0.977 x 10^5 (M/cm) for Halo7-D4H and Halo7-OlyA(E69A), respectively (calculated from amino acid composition data).[176]

For fluorescence labeling, purified proteins were incubated with 1.5 molar equivalents of SeTau647-Halo ligand[127] at 37ºC for 3 h. Unreacted ligand was removed by Ni-NTA affinity column chromatography and reconcentration. Purities were 71% (Halo7-D4H) and 90% (Halo7-OlyA[E69A]), as determined by SDS-PAGE with Coomassie Brilliant Blue R-250 (CBBR-250; Fluka, 27816) staining. Aliquots (30 μL) of the labeled protein solutions were

1855 snap-frozen in liquid nitrogen and stored at -80ºC.

Purification of zyxin and VASP

For the preparation of zyxin (WT and mutants) and VASP, proteins were expressed in Expi293F cells (Thermo Fisher Scientific) for three days as fusion constructs containing a
1860 6xHis tag, maltose binding protein (MBP), Tobacco Etch Virus (TEV) protease digestion sequence, and mCherry-zyxin or EGFP-VASP. Cells were harvested and lysed by freeze-thaw cycles in buffer A (200 mM NaCl, 1 mM EDTA, and 0.5 mM TCEP, buffered with 25 mM Tris-HCl, pH 7.4, and supplemented with protease inhibitor cocktail; Roche). Lysates were centrifuged at 21,000 x g at 4ºC for 1 h, and the proteins were purified in two steps. First,
1865 lysates were loaded onto an MBP-binding dextrin Sepharose column (MPBTrap; GE Healthcare) twice at 0.5 mL/min and eluted with 10 mM maltose in buffer A at RT. Eluates were digested with His-tagged TEV protease (1:10 enzyme:protein ratio by weight) at 16ºC for 18 h. Second, digests were processed by Ni-NTA chromatography (HisPur™ Ni-NTA Resin; Thermo Scientific) to separate mCherry-zyxin or EGFP-VASP from 6xHis-MBP and His-
1870 tagged TEV protease. For this step, NaCl and imidazole were added to the digested solutions to final concentrations of 400 and 25 mM, respectively, and the solution was passed twice over a pre-equilibrated Ni-NTA Sepharose slurry (5 mL bed volume) in a Poly-Prep Chromatography Column (Bio-Rad), equilibrated with a buffer solution (300 mM NaCl, 25 mM imidazole, and 0.5 mM TCEP, buffered with 25 mM Tris-HCl, pH 7.4). The flow-through
1875 fractions were concentrated using a Pierce Protein Concentrator (30 kDa MWCO, PES-membrane; Thermo Scientific, 88502) to ≈150 µL and dialyzed into buffer B (150 mM NaCl and 0.5 mM TCEP, buffered with 25 mM Tris-HCl, pH 7.4) at 4ºC overnight using micro-dialyzer units (10 kDa MWCO; Slide-A-Lyzer MINI, Thermo Scientific).

Protein concentrations were determined by the absorbance at 280 nm, using extinction
1880 coefficients of 6.11, 6.15, 5.30, 5.18, and 4.84 x 10^4 (M/cm) for GFP-VASP, mCherry-zyxin (WT), mCherry-zyxin (ΔPr), mCherry-zyxin (ΔIDR), and mCherry-zyxin (ΔNC), respectively (calculated from amino acid composition).[176] Purities were 84, 72, 69, 89, and 71%, respectively, as determined by SDS-PAGE stained with InstantBlue Coomassie Protein Stain (Abcam). Aliquots (10 µL) were snap-frozen in liquid nitrogen and stored at -80ºC.

1885

In vitro phase separation assay

Purified zyxin and VASP were diluted in buffer B to the desired concentrations. After the

addition of 1% PEG8K, mixtures were transferred to glass-bottom slides (Ibidi, 81507) for imaging. All reactions and imaging were performed at 37ºC.

1890

In vitro cell growth assay

For growth assays, 1 x10^4 MEFs or 5 x10^4 transformed MEFs, RKO, and MDA-MB231 cells were seeded per well in six-well plates in triplicate. Cells were counted every 2 days using an automated cell counter (Invitrogen, Countess), and proliferation curves were plotted
1895 based on cell numbers per well.

Complement-dependent cytotoxicity assay

Transformed zyxin-KO MEFs were plated on a polystyrene-bottom 96-well plate (Corning, 3603) at 2.5 x 10^3 cells/well and cultured overnight. The culture medium was replaced with
1900 50 µL T-HBSS containing 20 µg/mL rabbit anti-CHO polyclonal antibodies (ProteinTech), 1 µM Blue DCS1 (AAT Bioquest; membrane-impermeable nuclear staining dye for dead cells), and 1:20 diluted NucRed Live 647 (Invitrogen; membrane-permeable nuclear staining dye for total cells). After an incubation at 37ºC for 30 min, the cells were washed and imaged by epi-fluorescence microscopy (4x objective lens). The culture medium was then replaced
1905 with 50 µL T-HBSS containing 1 µM Blue DCS1, 1:20 diluted NucRed Live 647, and varying concentrations of standardized human serum (Sigma-Aldrich). After an incubation at 37ºC for 2 h, the cells were washed and re-imaged. Floating dead cells were removed during washing. Acquired images were binarized by ilastik, and the NucRed Live 647-positive and Blue DCS1-negative cells were counted as live cells. Total and live cell numbers were
1910 calculated from the first and second images, respectively. Negative controls used heat-inactivated standard serum (56ºC for 30 min).

Cell growth assay after complement stimulation

Transformed zyxin-KO MEFs were plated on a polystyrene-bottom 384-well plate (Corning,
1915 4514) at 5 x 10^2 cells/well and cultured for 24 h. The culture medium was replaced with complete growth medium containing 20 µg/mL rabbit anti-CHO polyclonal antibodies and 10% C9-depleted human serum (Calbiochem), followed by an incubation for 12 h. Since C9-depleted serum cannot form a complete membrane attack complex (MAC), this system specifically assesses CD59 activation by the C5-8 complex (MAC precursor). After the
1920 incubation, the cells were fixed with 4% PFA, and nuclei were stained with Blue DCS1. Cell

numbers were counted from fluorescence images.

Single-molecule imaging of MAC precursor

For fluorescence labeling of complement C8, human complement C8 (Sigma-Aldrich) was labeled with CF640R-succinimidyl ester according to the manufacturer's instructions. The labeled C8 protein was purified with an Amicon Ultra spin filter (10 kDa cutoff; Millipore). The dye/protein ratio was calculated to be 3.4.

For single-molecule imaging of MAC precursor, transformed zyxin-KO MEFs expressing mGFP-zyxin, cultured on glass-bottom dishes, were incubated in T-HBSS containing 20 μg/mL rabbit anti-CHO polyclonal antibodies for 10 min at 37ºC. Cells were washed and further incubated with T-HBSS containing 10% C8-depleted human serum (Sigma-Aldrich), 1% BSA, and 100 nM C8-CF640R for 10 min at 37ºC. After washing, the cells were imaged, and the imaging was completed within 10 min.

Tumor xenograft assays

Cells were trypsinized and resuspended in DMEM supplemented with 30% FBS, and then mixed with VitroGel (TheWell Bioscience) at a 1:2 ratio (vol/vol). A total of 100 μL of the cell-gel mixture, containing either 5 x 10^6 transformed MEFs or 2 x 10^6 RKO cells, was injected subcutaneously into the right flank of 6- to 8-week-old female nude mice (BALB/cAJcl-*nu/nu*). Tumor growth was monitored every ≈3 days starting ≈7 days after implantation. Tumor volume (V) was estimated using the formula, V = 0.5 x length x width^2,[177] where length and width represent the longest and shortest dimensions, respectively, measured with calipers. Measurements were performed by multiple investigators blinded to group identity. At ≈30 days after implantation, mice were euthanized in a CO_2 chamber, and the tumors were excised, weighed, and photographed. Small tumor pieces (≈2 x 2 x 2 mm) were collected for downstream analysis, including western blotting. Tumor implantation experiments were independently performed twice, using 6 and 4 mice per group in the two replicates.

Coarse-grained models for Zyxin (IDR2)

We modeled the zyxin IDR2 using a residue-resolution coarse-grained (CG) representation, where each amino acid is represented by a single interaction site. Simulations were performed using the Mpipi model.[52] The total potential energy is written as:

$$V_{\mathrm{MPIPI}} = \sum_{(i,j)\in\mathrm{bonds}} E_{\mathrm{bond}}(b_{ij}) + \sum_{(i,j)\in\mathrm{nonbonded\ particles}} E_{\mathrm{WF}}(r_{ij}) + \sum_{(i,j)\in\mathrm{charged\ particles}} E_{\mathrm{ele}}(r_{ij}) \ .$$

Here, $E_{bond}(b_{ij})$ constrains chain connectivity through a harmonic bonded interaction with bond length (b_{ij}). Nonbonded contacts between residue pairs are treated using the Wang-Frenkel potential,

$$E_{\mathrm{WF}}(r_{ij}) = \varepsilon_{ij}\,\alpha_{ij}\left[\left(\frac{\sigma_{ij}}{r_{ij}}\right)^{2\mu_{ij}} - 1\right]\left[\left(\frac{R_{ij}}{r_{ij}}\right)^{2\mu_{ij}} - 1\right]^{2\nu_{ij}} \ ,$$

where ε_{ij}, σ_{ij}, $R_{ij}(= 3\sigma_{ij})$, μ_{ij}, ν_{ij}, and α_{ij} depend on the types of residues i and j.

Electrostatic interactions between charged residues are modeled using a Debye-Hückel formulation:

$$E_{\mathrm{ele}}(r_{ij}) = \frac{q_i q_j}{4\pi\epsilon_0\epsilon_r(T,C)}\frac{\exp\left(-r_{ij}/\lambda_D\right)}{r_{ij}} \ ,$$

where q_i and q_j are particle charges, λ_D is the Debye screening length, and $\epsilon_r(T,C)$ denotes the dielectric constant of the solution as a function of temperature (T) and ionic strength (C). The temperature and salt dependencies follow:

$$\epsilon_r(T,C) = e(T)a(C) \ ,$$

where $e(T) = 249.4 - 0.788\,T + 7.20\times10^{-4}T^2$, and $a(C) = 1 - 0.2551C + 5.151\times10^{-2}C^2 - 6.889\times10^{-3}C^3$.

Finally, the Debye length is computed as:

$$\lambda_D = \sqrt{\frac{\epsilon_0\epsilon_r(T,C)k_BT}{2N_Ae_c^2I}} \ ,$$

where N_A is Avogadro's number, e_c the elementary charge, and I the ionic strength.

Molecular dynamics simulations of Zyxin IDR2

Zyxin IDR2 (Figure 4D) was used as the model system in molecular dynamics simulations. CG topologies and initial coordinates were generated using GENESIS-cg-tool.[178] To characterize the temperature-dependent behavior, we first simulated a single chain over a temperature range of 210-440 K in 10 K increments, with each trajectory run for 10^7 MD steps. These simulations were used to identify the approximate temperature window associated with phase transitions (Figures S5D and S5E). Structures sampled from these

single-chain trajectories were subsequently used as templates for constructing multi-chain systems.

To directly probe the phase behavior, we built condensate-scale systems composed of 200 zyxin IDR2 chains. Initial configurations were generated by placing structures sampled from the single-chain simulations onto a 2 x 4 x 25 spatial grid. The simulation cell was then gradually reduced in size using the box-shrink protocol in GENESIS ATDYN until a compact size of 250 x 250 x 400 Å^3 was achieved. After equilibration, the periodic boundary conditions were elongated along the z-axis to 250 x 250 x 2000 Å^3, and these structures served as starting points for production simulations. Each condensate system was simulated for 10^7 steps at 210, 230, 250, 270, and 290K.

All simulations employed the GENESIS MD software: ATDYN (v2.1.5)[179] for single-chain simulations and multi-chain box-shrink procedures, and CGDYN (v2.1.0-beta)[180]for condensate production runs. A time step of 10 fs was used. Nonbonded electrostatics were calculated with a 35-Å cutoff, and the time integration used a Langevin thermostat with a friction coefficient of 0.01 ps^{-1}.

Molecular dynamics simulation data analysis

To identify the dominant interactions stabilizing zyxin IDR2 condensates, we performed contact analysis. For each snapshot, a smoothed contact score was computed for every pair of residues with indices i and j across different chains:

$$n(i,j) = \frac{1}{n_{chain}} \sum_{\text{chain } I} \sum_{\text{chain } J \neq I} \sum_{\text{res}_i \in I} \sum_{\text{res}_j \in J} n_c(\text{res}_i, \text{res}_j) \quad ,$$

where the pairwise term n_c was defined using a sigmoidal switching function:

$$n_c = \frac{1}{1 + e^{(r_{ij} - r_0)/r_w}} \quad .$$

Here, r_{ij} is the distance between residues res_i and res_i, with $r_0 = 10$ Å as the characteristic length and $r_w = 1$ Å controlling the smoothing width. Time-averaged values of $n(i,j)$ were used to construct the two-dimensional contact probability map (Figure 3D, left). The total number of contacts made by the i-th residue was then obtained by summing over all partners:

$$N(i) = \sum_j n(i,j) \quad .$$

To quantify interaction preferences between residue types, we calculated type-type normalized contact scores (Figure 3D, right):

$$p(a,b) = \frac{\sum_{i \mid \mathrm{type}_i = a} \sum_{j \mid \mathrm{type}_j = b} n(i,j)}{o_a \, o_b} \quad ,$$

where o_a and o_b denote the total occurrences of residue types a and b in zyxin IDR2, respectively.

QUANTIFICATION AND STATISTICAL ANALYSIS

Superimposition of dual-color image sequences and single-molecule tracking were performed using in-house C++-based computer programs, as previously described.[121,166] Conventional TIRF images were analyzed using Fiji (imageJ),[151] MatLab 2019a (MathWorks), and ilastik.[153] Curve fitting was performed using Origin 2017 (OriginLab). Statistical analyses were performed using OriginPro 2017, Rstudio, and Microsoft Excel. Statistical significance was defined as $P<0.05$. Other image and data analyses were performed using imageJ (Fiji) and MatLab 2019a. Figures and videos were edited using Photoshop CC 2021 (Adobe) and Illustrator CC 2021 (Adobe).

REFERENCES

2030 1. Lemmon, M.A., and Schlessinger, J. (2010). Cell signaling by receptor tyrosine kinases. Cell *141*, 1117–1134. https://doi.org/10.1016/j.cell.2010.06.011.

2. Tomuleasa, C., Tigu, A.-B., Munteanu, R., Moldovan, C.-S., Kegyes, D., Onaciu, A., Gulei, D., Ghiaur, G., Einsele, H., and Croce, C.M. (2024). Therapeutic advances of targeting receptor tyrosine kinases in cancer. Signal Transduct. Target. Ther. *9*, 201.
2035 https://doi.org/10.1038/s41392-024-01899-w.

3. Couves, E.C., Gardner, S., Voisin, T.B., Bickel, J.K., Stansfeld, P.J., Tate, E.W., and Bubeck, D. (2023). Structural basis for membrane attack complex inhibition by CD59. Nat. Commun. *14*, 890. https://doi.org/10.1038/s41467-023-36441-z.

4. Suzuki, K.G., Fujiwara, T.K., Sanematsu, F., Iino, R., Edidin, M., and Kusumi, A. (2007).
2040 GPI-anchored receptor clusters transiently recruit Lyn and G alpha for temporary cluster immobilization and Lyn activation: single-molecule tracking study 1. J. Cell Biol. *177*, 717–730. https://doi.org/10.1083/jcb.200609174.

5. Suzuki, K.G., Fujiwara, T.K., Edidin, M., and Kusumi, A. (2007). Dynamic recruitment of phospholipase C gamma at transiently immobilized GPI-anchored receptor clusters induces
2045 IP3-Ca2+ signaling: single-molecule tracking study 2. J. Cell Biol. *177*, 731–742. https://doi.org/10.1083/jcb.200609175.

6. Koyama-Honda, I., Fujiwara, T.K., Kasai, R.S., Suzuki, K.G.N., Kajikawa, E., Tsuboi, H., Tsunoyama, T.A., and Kusumi, A. (2020). High-speed single-molecule imaging reveals signal transduction by induced transbilayer raft phases. J. Cell Biol. *219*, e202006125.
2050 https://doi.org/10.1083/jcb.202006125.

7. Humeau, J., Pedro, J.M.B.-S., Vitale, I., Nuñez, L., Villalobos, C., Kroemer, G., and Senovilla, L. (2018). Calcium signaling and cell cycle: Progression or death. Cell Calcium *70*, 3–15. https://doi.org/10.1016/j.ceca.2017.07.006.

8. Guo, W., and Giancotti, F.G. (2004). Integrin signalling during tumour progression. Nat.
2055 Rev. Mol. Cell Biol. *5*, 816–826. https://doi.org/10.1038/nrm1490.

9. Chen, Z., Oh, D., Dubey, A.K., Yao, M., Yang, B., Groves, J.T., and Sheetz, M. (2018). EGFR family and Src family kinase interactions: mechanics matters? Curr. Opin. Cell Biol. *51*, 97–102. https://doi.org/10.1016/j.ceb.2017.12.003.

10. Alfonzo-Méndez, M.A., Sochacki, K.A., Strub, M.-P., and Taraska, J.W. (2022). Dual clathrin and integrin signaling systems regulate growth factor receptor activation. Nat. Commun. *13*, 905. https://doi.org/10.1038/s41467-022-28373-x.

11. Zanten, T.S. van, Cambi, A., Koopman, M., Joosten, B., Figdor, C.G., and Garcia-Parajo, M.F. (2009). Hotspots of GPI-anchored proteins and integrin nanoclusters function as nucleation sites for cell adhesion. Proc. Natl. Acad. Sci. USA *106*, 18557–18562. https://doi.org/10.1073/pnas.0905217106.

12. Fiore, V.F., Strane, P.W., Bryksin, A.V., White, E.S., Hagood, J.S., and Barker, T.H. (2015). Conformational coupling of integrin and Thy-1 regulates Fyn priming and fibroblast mechanotransduction. J. Cell Biol. *211*, 173–190. https://doi.org/10.1083/jcb.201505007.

13. Cui, X., Zhang, X., Bu, H., Liu, N., Li, H., Guan, X., Yan, H., Wang, Y., Zhang, H., Ding, Y., et al. (2017). Shear stress-mediated changes in the expression of complement regulatory protein CD59 on human endothelial progenitor cells by ECM-integrinαVβ3-F-actin pathway in vitro. Biochem. Biophys. Res. Commun. *494*, 416–421. https://doi.org/10.1016/j.bbrc.2017.09.019.

14. Strainic, M.G., Liu, J., An, F., Bailey, E., Esposito, A., Hamann, J., Heeger, P.S., and Medof, M.E. (2019). CD55 is essential for CD103^{+} dendritic cell tolerogenic responses that protect against autoimmunity. Am. J. Pathol. *189*, 1386–1401. https://doi.org/10.1016/j.ajpath.2019.04.008.

15. Kalappurakkal, J.M., Anilkumar, A.A., Patra, C., Zanten, T.S. van, Sheetz, M.P., and Mayor, S. (2019). Integrin mechano-chemical signaling generates plasma membrane nanodomains that promote cell spreading. Cell *177*, 1738-1756. e23. https://doi.org/10.1016/j.cell.2019.04.037.

16. Miao, M.Z., Lee, J.S., Yamada, K.M., and Loeser, R.F. (2024). Integrin signalling in joint development, homeostasis and osteoarthritis. Nat. Rev. Rheumatol. *20*, 492–509. https://doi.org/10.1038/s41584-024-01130-8.

17. Nishimura, R., and Kanchanawong, P. (2025). Nanoscale mechano-adaption of integrin-based cell adhesions: New tools and techniques lead the way. Curr. Opin. Cell Biol. *94*, 102509. https://doi.org/10.1016/j.ceb.2025.102509.

18. Chen, T., and Giannone, G. (2024). Single molecule imaging unveils cellular architecture, dynamics and mechanobiology. Curr. Opin. Cell Biol. *88*, 102369. https://doi.org/10.1016/j.ceb.2024.102369.

19. Theodosiou, M., Widmaier, M., Böttcher, R.T., Rognoni, E., Veelders, M., Bharadwaj, M., Lambacher, A., Austen, K., Müller, D.J., Zent, R., et al. (2016). Kindlin-2 cooperates with talin to activate integrins and induces cell spreading by directly binding paxillin. eLife *5*, e10130. https://doi.org/10.7554/elife.10130.

20. Zhou, P., Tsunoyama, T.A., Kasai, R.S., Hirosawa, K.M., Kalay, Z., Aladag, A., Fujiwara, T.K., Yokoyama, T., Sakamoto, M., Kise, R., et al. (2025). Single-molecule methods for characterizing receptor dimers reveal metastable opioid receptor homodimers that induce functional modulation. Nat. Commun. *16*, 9858. https://doi.org/10.1038/s41467-025-64694-3.

21. Stone, M.B., and Veatch, S.L. (2014). Steady-state cross-correlations for live two-colour super-resolution localization data sets. Nat. Commun. *6*, 7347. https://doi.org/10.1038/ncomms8347.

22. Hoffman, L.M., Jensen, C.C., Kloeker, S., Wang, C.-L.A., Yoshigi, M., and Beckerle, M.C. (2006). Genetic ablation of zyxin causes Mena/VASP mislocalization, increased motility, and deficits in actin remodeling. J. Cell Biol. *172*, 771–782. https://doi.org/10.1083/jcb.200512115.

23. Fujiwara, T.K., Iwasawa, K., Kalay, Z., Tsunoyama, T.A., Watanabe, Y., Umemura, Y.M., Murakoshi, H., Suzuki, K.G.N., Nemoto, Y.L., Morone, N., et al. (2016). Confined diffusion of transmembrane proteins and lipids induced by the same actin meshwork lining the plasma membrane. Mol. Biol. Cell *27*, 1101–1119. https://doi.org/10.1091/mbc.e15-04-0186.

24. Winkelmann, H., Richter, C.P., Eising, J., Piehler, J., and Kurre, R. (2024). Correlative single-molecule and structured illumination microscopy of fast dynamics at the plasma membrane. Nat. Commun. *15*, 5813. https://doi.org/10.1038/s41467-024-49876-9.

25. Lajoie, P., Goetz, J.G., Dennis, J.W., and Nabi, I.R. (2009). Lattices, rafts, and scaffolds: domain regulation of receptor signaling at the plasma membrane. J. Cell Biol. *185*, 381–385. https://doi.org/10.1083/jcb.200811059.

26. Simons, K., and Sampaio, J.L. (2011). Membrane organization and lipid rafts. Cold Spring Harb. Perspect. Biol. *3*, a004697. https://doi.org/10.1101/cshperspect.a004697.

27. Kusumi, A., Fujiwara, T.K., Tsunoyama, T.A., Kasai, R.S., Liu, A.A., Hirosawa, K.M., Kinoshita, M., Matsumori, N., Komura, N., Ando, H., et al. (2020). Defining raft domains in the plasma membrane. Traffic *21*, 106–137. https://doi.org/10.1111/tra.12718.

28. Maekawa, M. (2017). Domain 4 (D4) of perfringolysin O to visualize cholesterol in cellular membranes—the update. Sensors *17*, 504. https://doi.org/10.3390/s17030504.

29. Endapally, S., Frias, D., Grzemska, M., Gay, A., Tomchick, D.R., and Radhakrishnan, A. (2019). Molecular discrimination between two conformations of sphingomyelin in plasma membranes. Cell *176*, 1040-1053. e17. https://doi.org/10.1016/j.cell.2018.12.042.

30. Uchida, Y., Hasegawa, J., Chinnapen, D., Inoue, T., Okazaki, S., Kato, R., Wakatsuki, S., Misaki, R., Koike, M., Uchiyama, Y., et al. (2011). Intracellular phosphatidylserine is essential for retrograde membrane traffic through endosomes. Proc. Natl. Acad. Sci. USA *108*, 15846–15851. https://doi.org/10.1073/pnas.1109101108.

31. Lee, S., Uchida, Y., Wang, J., Matsudaira, T., Nakagawa, T., Kishimoto, T., Mukai, K., Inaba, T., Kobayashi, T., Molday, R.S., et al. (2015). Transport through recycling endosomes requires EHD1 recruitment by a phosphatidylserine translocase. EMBO J. *34*, 669–688. https://doi.org/10.15252/embj.201489703.

32. Furutani, M., Tsujita, K., Itoh, T., Ijuin, T., and Takenawa, T. (2006). Application of phosphoinositide-binding domains for the detection and quantification of specific phosphoinositides. Anal. Biochem. *355*, 8–18. https://doi.org/10.1016/j.ab.2006.05.014.

33. Idevall-Hagren, O., Dickson, E.J., Hille, B., Toomre, D.K., and Camilli, P.D. (2012). Optogenetic control of phosphoinositide metabolism. Proc. Natl. Acad. Sci. USA *109*, E2316–E2323. https://doi.org/10.1073/pnas.1211305109.

34. Santos, M. de S., Naal, R.M.Z.G., Baird, B., and Holowka, D. (2013). Inhibitors of PI(4,5)P_2 synthesis reveal dynamic regulation of IgE receptor signaling by phosphoinositides in RBL mast cells. Mol. Pharmacol. *83*, 793–804. https://doi.org/10.1124/mol.112.082834.

35. Rouches, M., Veatch, S.L., and Machta, B.B. (2021). Surface densities prewet a near-critical membrane. Proc. Natl. Acad. Sci. USA *118*, e2103401118. https://doi.org/10.1073/pnas.2103401118.

36. Tsunoyama, T.A., Hoffmann, C., Tang, B., Hirosawa, K.M., Nemoto, Y.L., Kasai, R.S., Fujiwara, T.K., Suzuki, K.G.N., Milovanovic, D., and Kusumi, A. (2022). iTRVZ: liquid nano-platform for signal integration on the plasma membrane. bioRxiv, 2021.12.30.474523. https://doi.org/10.1101/2021.12.30.474523.

37. Hoffmann, C., and Milovanovic, D. (2023). Dipping contacts – a novel type of contact site at the interface between membraneless organelles and membranes. J. Cell Sci. *136*, jcs261413. https://doi.org/10.1242/jcs.261413.

38. Wan, Y., Hudson, R., Smith, J., Forman-Kay, J.D., and Ditlev, J.A. (2025). Protein interactions, calcium, phosphorylation, and cholesterol modulate CFTR cluster formation

on membranes. Proc. Natl. Acad. Sci. USA *122*, e2424470122. https://doi.org/10.1073/pnas.2424470122.

39. Sengupta, P., Van Engelenburg, S., and Lippincott-Schwartz, J. (2012). Visualizing cell structure and function with point-localization superresolution imaging. Dev. Cell *23*, 1092–1102. https://doi.org/10.1016/j.devcel.2012.09.022.

40. Levet, F., Hosy, E., Kechkar, A., Butler, C., Beghin, A., Choquet, D., and Sibarita, J.-B. (2015). SR-Tesseler: a method to segment and quantify localization-based super-resolution microscopy data. Nat. Methods *12*, 1065–1071. https://doi.org/10.1038/nmeth.3579.

41. Khater, I.M., Nabi, I.R., and Hamarneh, G. (2020). A review of super-resolution single-molecule localization microscopy cluster analysis and quantification methods. Patterns *1*, 100038. https://doi.org/10.1016/j.patter.2020.100038.

42. Piovesan, D., Necci, M., Escobedo, N., Monzon, A.M., Hatos, A., Mičetić, I., Quaglia, F., Paladin, L., Ramasamy, P., Dosztányi, Z., et al. (2020). MobiDB: intrinsically disordered proteins in 2021. Nucleic Acids Res. *49*, D361–D367. https://doi.org/10.1093/nar/gkaa1058.

43. Jaqaman, K., and Ditlev, J.A. (2021). Biomolecular condensates in membrane receptor signaling. Curr. Opin. Cell Biol. *69*, 48–54. https://doi.org/10.1016/j.ceb.2020.12.006.

44. Hoffmann, C., Sansevrino, R., Morabito, G., Logan, C., Vabulas, R.M., Ulusoy, A., Ganzella, M., and Milovanovic, D. (2021). Synapsin condensates recruit alpha-synuclein. J. Mol. Biol. *433*, 166961. https://doi.org/10.1016/j.jmb.2021.166961.

45. Peng, S., Li, W., Yao, Y., Xing, W., Li, P., and Chen, C. (2020). Phase separation at the nanoscale quantified by dcFCCS. Proc. Natl. Acad. Sci. USA *117*, 27124–27131. https://doi.org/10.1073/pnas.2008447117.

46. Kar, M., Dar, F., Welsh, T.J., Vogel, L.T., Kühnemuth, R., Majumdar, A., Krainer, G., Franzmann, T.M., Alberti, S., Seidel, C.A.M., et al. (2022). Phase-separating RNA-binding proteins form heterogeneous distributions of clusters in subsaturated solutions. Proc. Natl. Acad. Sci. USA *119*, e2202222119. https://doi.org/10.1073/pnas.2202222119.

47. Lan, C., Kim, J., Ulferts, S., Aprile-Garcia, F., Weyrauch, S., Anandamurugan, A., Grosse, R., Sawarkar, R., Reinhardt, A., and Hugel, T. (2023). Quantitative real-time in-cell imaging reveals heterogeneous clusters of proteins prior to condensation. Nat. Commun. *14*, 4831. https://doi.org/10.1038/s41467-023-40540-2.

48. Kusumi, A., Tsunoyama, T.A., Suzuki, K.G.N., Fujiwara, T.K., and Aladag, A. (2024). Transient, nano-scale, liquid-like molecular assemblies coming of age. Curr. Opin. Cell Biol. *89*, 102394. https://doi.org/10.1016/j.ceb.2024.102394.

49. Ge, Y., Paul, T., Gordiychuk, M., Das, N., Zhang, Y., and Myong, S. (2025). FUS nanoclusters are a distinct state within the dilute phase. Nat. Commun. *16*, 9956. https://doi.org/10.1038/s41467-025-64909-7.

50. Shinn, M.K., Tomares, D.T., Liu, V., Pant, A., Qiu, Y., Vitalis, A., Song, Y.J., Ayala, Y., Ruff, K.M., Strout, G.W., et al. (2026). Nuclear speckle proteins form intrinsic and MALAT1-dependent microphases. Cell *189*, 832-852.e24. https://doi.org/10.1016/j.cell.2025.11.026.

51. Wiegand, T., Liu, J., Vogeley, L., LuValle-Burke, I., Geisler, J., Fritsch, A.W., Hyman, A.A., and Grill, S.W. (2024). Actin polymerization counteracts prewetting of N-WASP on supported lipid bilayers. Proc. Natl. Acad. Sci. USA *121*, e2407497121. https://doi.org/10.1073/pnas.2407497121.

52. Joseph, J.A., Reinhardt, A., Aguirre, A., Chew, P.Y., Russell, K.O., Espinosa, J.R., Garaizar, A., and Collepardo-Guevara, R. (2021). Physics-driven coarse-grained model for biomolecular phase separation with near-quantitative accuracy. Nat. Comput. Sci. *1*, 732–743. https://doi.org/10.1038/s43588-021-00155-3.

53. Graham, K., Chandrasekaran, A., Wang, L., Ladak, A., Lafer, E.M., Rangamani, P., and Stachowiak, J.C. (2023). Liquid-like VASP condensates drive actin polymerization and dynamic bundling. Nat. Phys. *19*, 574–585. https://doi.org/10.1038/s41567-022-01924-1.

54. Narayan, K.B., James, H.P., Cope, J., Mondal, S., Baeyens, L., Milano, F., Zheng, J., Krause, M., and Baumgart, T. (2024). VASP phase separation with priming proteins of fast endophilin mediated endocytosis modulates actin polymerization. bioRxiv, 2024.03.21.586200. https://doi.org/10.1101/2024.03.21.586200.

55. Hsu, C.-P., Aretz, J., Hordeichyk, A., Fässler, R., and Bausch, A.R. (2023). Surface-induced phase separation of reconstituted nascent integrin clusters on lipid membranes. Proc. Natl. Acad. Sci. USA *120*, e2301881120. https://doi.org/10.1073/pnas.2301881120.

56. Su, X., Ditlev, J.A., Hui, E., Xing, W., Banjade, S., Okrut, J., King, D.S., Taunton, J., Rosen, M.K., and Vale, R.D. (2016). Phase separation of signaling molecules promotes T cell receptor signal transduction. Science *352*, 595–599. https://doi.org/10.1126/science.aad9964.

57. Case, L.B., Zhang, X., Ditlev, J.A., and Rosen, M.K. (2019). Stoichiometry controls activity of phase-separated clusters of actin signaling proteins. Science *363*, 1093–1097. https://doi.org/10.1126/science.aau6313.

58. Huang, W.Y.C., Alvarez, S., Kondo, Y., Lee, Y.K., Chung, J.K., Lam, H.Y.M., Biswas, K.H., Kuriyan, J., and Groves, J.T. (2019). A molecular assembly phase transition and kinetic proofreading modulate Ras activation by SOS. Science *363*, 1098–1103. https://doi.org/10.1126/science.aau5721.

59. Dine, E., Reed, E.H., and Toettcher, J.E. (2021). Positive feedback between the T cell kinase Zap70 and its substrate LAT acts as a clustering-dependent signaling switch. Cell Reports *35*, 109280–109280. https://doi.org/10.1016/j.celrep.2021.109280.

60. Ryu, S.H., Cho, K.S., Lee, K.Y., Suh, P.G., and Rhee, S.G. (1987). Purification and characterization of two immunologically distinct phosphoinositide-specific phospholipases C from bovine brain. J. Biol. Chem. *262*, 12511–12518.

61. Bae, Y.S., Cantley, L.G., Chen, C.S., Kim, S.R., Kwon, K.S., and Rhee, S.G. (1998). Activation of phospholipase C-gamma by phosphatidylinositol 3,4,5-trisphosphate. J. Biol. Chem. *273*, 4465–4469. https://doi.org/10.1074/jbc.273.8.4465.

62. Glaviano, A., Foo, A.S.C., Lam, H.Y., Yap, K.C.H., Jacot, W., Jones, R.H., Eng, H., Nair, M.G., Makvandi, P., Geoerger, B., et al. (2023). PI3K/AKT/mTOR signaling transduction pathway and targeted therapies in cancer. Mol. Cancer *22*, 138. https://doi.org/10.1186/s12943-023-01827-6.

63. Lin, C.-C., Suen, K.M., Jeffrey, P.-A., Wieteska, L., Lidster, J.A., Bao, P., Curd, A.P., Stainthorp, A., Seiler, C., Koss, H., et al. (2022). Receptor tyrosine kinases regulate signal transduction through a liquid-liquid phase separated state. Mol. Cell *82*, 1089-1106. e12. https://doi.org/10.1016/j.molcel.2022.02.005.

64. Acebrón, I., Righetto, R.D., Schoenherr, C., Buhr, S., Redondo, P., Culley, J., Rodríguez, C.F., Daday, C., Biyani, N., Llorca, O., et al. (2020). Structural basis of focal adhesion kinase activation on lipid membranes. EMBO J. *39*, e104743. https://doi.org/10.15252/embj.2020104743.

65. Wei, H., Malik, M., Sheikh, A.M., Merz, G., Brown, W.T., and Li, X. (2011). Abnormal cell properties and down-regulated FAK-Src complex signaling in B lymphoblasts of autistic subjects. Am. J. Pathol. *179*, 66–74. https://doi.org/10.1016/j.ajpath.2011.03.034.

66. Wan, Q., TruongVo, T., Steele, H.E., Ozcelikkale, A., Han, B., Wang, Y., Oh, J., Yokota, H., and Na, S. (2017). Subcellular domain-dependent molecular hierarchy of SFK

and FAK in mechanotransduction and cytokine signaling. Sci. Rep. *7*, 9033. https://doi.org/10.1038/s41598-017-09495-5.

67. Liu, B., Stone, O.J., Pablo, M., Herron, J.C., Nogueira, A.T., Dagliyan, O., Grimm, J.B., Lavis, L.D., Elston, T.C., and Hahn, K.M. (2021). Biosensors based on peptide exposure show single molecule conformations in live cells. Cell *184*, 5670-5685.e23. https://doi.org/10.1016/j.cell.2021.09.026.

68. Shin, Y., Berry, J., Pannucci, N., Haataja, M.P., Toettcher, J.E., and Brangwynne, C.P. (2017). Spatiotemporal control of intracellular phase transitions using light-activated optoDroplets. Cell *168*, 159-171.e14. https://doi.org/10.1016/j.cell.2016.11.054.

69. Dine, E., Gil, A.A., Uribe, G., Brangwynne, C.P., and Toettcher, J.E. (2018). Protein phase separation provides long-term memory of transient spatial stimuli. Cell Syst. *6*, 655-663.e5. https://doi.org/10.1016/j.cels.2018.05.002.

70. Hirenallur-Shanthappa, D.K., Ramírez, J.A., and Iritani, B.M. (2017). Patient derived tumor xenograft models. Academic Press, 57–73. https://doi.org/10.1016/b978-0-12-804010-2.00005-9.

71. Dustin, M.L., and Depoil, D. (2011). New insights into the T cell synapse from single molecule techniques. Nat. Rev. Immunol. *11*, 672–684. https://doi.org/10.1038/nri3066.

72. Südhof, T.C. (2021). The cell biology of synapse formation. J. Cell Biol. *220*, e202103052. https://doi.org/10.1083/jcb.202103052.

73. Jia, B., Shen, Z., Zhu, S., Huang, J., Liao, Z., Zhao, S., Li, H., Chen, S., Xu, Y., Wang, Y., et al. (2025). Shank3 oligomerization governs material properties of the postsynaptic density condensate and synaptic plasticity. Cell *188*, 6473-6491.e21. https://doi.org/10.1016/j.cell.2025.07.047.

74. Weems, A.D., Welf, E.S., Driscoll, M.K., Zhou, F.Y., Mazloom-Farsibaf, H., Chang, B.-J., Murali, V.S., Gihana, G.M., Weiss, B.G., Chi, J., et al. (2023). Blebs promote cell survival by assembling oncogenic signalling hubs. Nature *615*, 517–525. https://doi.org/10.1038/s41586-023-05758-6.

75. DiRusso, C.J., Dashtiahangar, M., and Gilmore, T.D. (2022). Scaffold proteins as dynamic integrators of biological processes. J. Biol. Chem. *298*, 102628. https://doi.org/10.1016/j.jbc.2022.102628.

76. Bag, N., Wagenknecht-Wiesner, A., Lee, A., Shi, S.M., Holowka, D.A., and Baird, B.A. (2021). Lipid-based and protein-based interactions synergize transmembrane signaling

stimulated by antigen clustering of IgE receptors. Proc. Natl. Acad. Sci. USA *118*, e2026583118. https://doi.org/10.1073/pnas.2026583118.

77. Litschel, T., Kelley, C.F., Cheng, X., Babl, L., Mizuno, N., Case, L.B., and Schwille, P. (2024). Membrane-induced 2D phase separation of the focal adhesion protein talin. Nat. Commun. *15*, 4986. https://doi.org/10.1038/s41467-024-49222-z.

78. Lafuente, E.M., Puijenbroek, A.A.F.L. van, Krause, M., Carman, C.V., Freeman, G.J., Berezovskaya, A., Constantine, E., Springer, T.A., Gertler, F.B., and Boussiotis, V.A. (2004). RIAM, an Ena/VASP and profilin ligand, interacts with Rap1-GTP and mediates Rap1-induced adhesion. Dev. Cell *7*, 585–595. https://doi.org/10.1016/j.devcel.2004.07.021.

79. Wynne, J.P., Wu, J., Su, W., Mor, A., Patsoukis, N., Boussiotis, V.A., Hubbard, S.R., and Philips, M.R. (2012). Rap1-interacting adapter molecule (RIAM) associates with the plasma membrane via a proximity detector. J. Cell Biol. *199*, 317–329. https://doi.org/10.1083/jcb.201201157.

80. Goult, B.T., Xu, X.-P., Gingras, A.R., Swift, M., Patel, B., Bate, N., Kopp, P.M., Barsukov, I.L., Critchley, D.R., Volkmann, N., et al. (2013). Structural studies on full-length talin1 reveal a compact auto-inhibited dimer: implications for talin activation. J. Struct. Biol. *184*, 21–32. https://doi.org/10.1016/j.jsb.2013.05.014.

81. Orré, T., Joly, A., Karatas, Z., Kastberger, B., Cabriel, C., Böttcher, R.T., Lévêque-Fort, S., Sibarita, J.-B., Fässler, R., Wehrle-Haller, B., et al. (2021). Molecular motion and tridimensional nanoscale localization of kindlin control integrin activation in focal adhesions. Nat. Commun. *12*, 3104. https://doi.org/10.1038/s41467-021-23372-w.

82. Morse, E.M., Brahme, N.N., and Calderwood, D.A. (2014). Integrin cytoplasmic tail interactions. Biochemistry *53*, 810–820. https://doi.org/10.1021/bi401596q.

83. Li, J., Jo, M.H., Yan, J., Hall, T., Lee, J., López-Sánchez, U., Yan, S., Ha, T., and Springer, T.A. (2024). Ligand binding initiates single-molecule integrin conformational activation. Cell *187*, 2990-3005.e17. https://doi.org/10.1016/j.cell.2024.04.049.

84. Sebé-Pedrós, A., Roger, A.J., Lang, F.B., King, N., and Ruiz-Trillo, I. (2010). Ancient origin of the integrin-mediated adhesion and signaling machinery. Proc. Natl. Acad. Sci. USA *107*, 10142–10147. https://doi.org/10.1073/pnas.1002257107.

85. Ruiz-Trillo, I., Kin, K., and Casacuberta, E. (2023). The origin of metazoan multicellularity: a potential microbial black swan event. Annu. Rev. Microbiol. *77*, 499–516. https://doi.org/10.1146/annurev-micro-032421-120023.

86. Rangarajan, S., Espeter, L., Drexler, H.C.A., Chrostek-Grashoff, A., and Grashoff, C. (2025). Talin force coupling underlies eukaryotic cell-substrate adhesion. Nat. Commun. *16*, 10950. https://doi.org/10.1038/s41467-025-67354-8.

87. Case, L.B., Pasquale, M.D., Henry, L., and Rosen, M.K. (2022). Synergistic phase separation of two pathways promotes integrin clustering and nascent adhesion formation. eLife *11*, e72588. https://doi.org/10.7554/elife.72588.

88. Gowrishankar, K., Ghosh, S., Saha, S., Rumamol, C., Mayor, S., and Rao, M. (2012). Active remodeling of cortical actin regulates spatiotemporal organization of cell surface molecules. Cell *149*, 1353–1367. https://doi.org/10.1016/j.cell.2012.05.008.

89. Garcia-Parajo, M.F., and Mayor, S. (2024). The ubiquitous nanocluster: a molecular scale organizing principle that governs cellular information flow. Curr. Opin. Cell Biol. *86*, 102285. https://doi.org/10.1016/j.ceb.2023.102285.

90. Pawson, C.T., and Scott, J.D. (2010). Signal integration through blending, bolstering and bifurcating of intracellular information. Nat. Struct. Mol. Biol. *17*, 653–658. https://doi.org/10.1038/nsmb.1843.

91. Chaturvedi, A., Hoffman, L.M., Jensen, C.C., Lin, Y.-C., Grossmann, A.H., Randall, R.L., Lessnick, S.L., Welm, A.L., and Beckerle, M.C. (2014). Molecular dissection of the mechanism by which EWS/FLI expression compromises actin cytoskeletal integrity and cell adhesion in Ewing sarcoma. Mol. Biol. Cell *25*, 2695–2709. https://doi.org/10.1091/mbc.e14-01-0007.

92. Ma, B., Cheng, H., Gao, R., Mu, C., Chen, L., Wu, S., Chen, Q., and Zhu, Y. (2016). Zyxin-Siah2–Lats2 axis mediates cooperation between Hippo and TGF-β signalling pathways. Nat. Commun. *7*, 11123. https://doi.org/10.1038/ncomms11123.

93. Kotb, A., Hyndman, M.E., and Patel, T.R. (2018). The role of zyxin in regulation of malignancies. Heliyon *4*, e00695. https://doi.org/10.1016/j.heliyon.2018.e00695.

94. Hamidi, H., and Ivaska, J. (2018). Every step of the way: integrins in cancer progression and metastasis. Nat. Rev. Cancer *18*, 533–548. https://doi.org/10.1038/s41568-018-0038-z.

95. Zhou, J., Zeng, Y., Cui, L., Chen, X., Stauffer, S., Wang, Z., Yu, F., Lele, S.M., Talmon, G.A., Black, A.R., et al. (2018). Zyxin promotes colon cancer tumorigenesis in a mitotic phosphorylation-dependent manner and through CDK8-mediated YAP activation. Proc. Natl. Acad. Sci. USA *115*, 201800621. https://doi.org/10.1073/pnas.1800621115.

96. Xiang, X., Wang, Y., Zhang, H., Piao, J., Muthusamy, S., Wang, L., Deng, Y., Zhang, W., Kuang, R., Billadeau, D.D., et al. (2018). Vasodilator-stimulated phosphoprotein promotes liver metastasis of gastrointestinal cancer by activating a β1-integrin-FAK-YAP1/TAZ signaling pathway. npj Precis. Oncol. *2*, 2. https://doi.org/10.1038/s41698-017-0045-7.

97. Tian, Y., Xu, L., He, Y., Xu, X., Li, K., Ma, Y., Gao, Y., Wei, D., and Wei, L. (2018). Knockdown of RAC1 and VASP gene expression inhibits breast cancer cell migration. Oncol. Lett. *16*, 2151–2160. https://doi.org/10.3892/ol.2018.8930.

98. Rezaie, Y., Fattahi, F., Mashinchi, B., Hesari, K.K., Montazeri, S., Kalantari, E., Madjd, Z., and Zanjani, L.S. (2023). High expression of Talin-1 is associated with tumor progression and recurrence in melanoma skin cancer patients. BMC Cancer *23*, 302. https://doi.org/10.1186/s12885-023-10771-z.

99. Shadman, H., Gomrok, S., Litle, C., Cheng, Q., Jiang, Y., Huang, X., Ziebarth, J.D., and Wang, Y. (2025). A machine learning-based investigation of integrin expression patterns in cancer and metastasis. Sci. Rep. *15*, 5270. https://doi.org/10.1038/s41598-025-89497-w.

100. Cai, D., Liu, Z., and Lippincott-Schwartz, J. (2021). Biomolecular condensates and their links to cancer progression. Trends Biochem. Sci. *46*, 535–549. https://doi.org/10.1016/j.tibs.2021.01.002.

101. López-Palacios, T.P., and Andersen, J.L. (2023). Kinase regulation by liquid–liquid phase separation. Trends Cell Biol. *33*, 649–666. https://doi.org/10.1016/j.tcb.2022.11.009.

102. Zanten, T.S. van, Cambi, A., Koopman, M., Joosten, B., Figdor, C.G., and Garcia-Parajo, M.F. (2009). Hotspots of GPI-anchored proteins and integrin nanoclusters function as nucleation sites for cell adhesion. Proc National Acad Sci *106*, 18557–18562. https://doi.org/10.1073/pnas.0905217106.

103. Morris, R.J. (2018). Thy-1, a pathfinder protein for the post-genomic era. Front. Cell Dev. Biol. *6*, 173. https://doi.org/10.3389/fcell.2018.00173.

104. Sezgin, E., Levental, I., Mayor, S., and Eggeling, C. (2017). The mystery of membrane organization: composition, regulation and roles of lipid rafts. Nat. Rev. Mol. Cell Biol. *18*, 361–374. https://doi.org/10.1038/nrm.2017.16.

105. Bag, N., London, E., Holowka, D.A., and Baird, B.A. (2022). Transbilayer coupling of lipids in cells investigated by imaging fluorescence correlation spectroscopy. J. Phys. Chem. B *126*, 2325–2336. https://doi.org/10.1021/acs.jpcb.2c00117.

106. Guo, W., and Giancotti, F.G. (2004). Integrin signalling during tumour progression. Nat Rev Mol Cell Bio *5*, 816–826. https://doi.org/10.1038/nrm1490.

107. Aretz, J., Aziz, M., Strohmeyer, N., Sattler, M., and Fässler, R. (2023). Talin and kindlin use integrin tail allostery and direct binding to activate integrins. Nat. Struct. Mol. Biol. *30*, 1913–1924. https://doi.org/10.1038/s41594-023-01139-9.

108. Fujiwara, T.K., Tsunoyama, T.A., Takeuchi, S., Kalay, Z., Nagai, Y., Kalkbrenner, T., Nemoto, Y.L., Chen, L.H., Shibata, A.C.E., Iwasawa, K., et al. (2023). Ultrafast single-molecule imaging reveals focal adhesion nano-architecture and molecular dynamics. J. Cell Biol. *222*, e202110162. https://doi.org/10.1083/jcb.202110162.

109. Swaminathan, V., Alushin, G.M., and Waterman, C.M. (2017). Mechanosensation: a catch bond that only hooks one way. Curr. Biol. *27*, R1158–R1160. https://doi.org/10.1016/j.cub.2017.09.023.

110. Massou, S., Vicente, F.N., Wetzel, F., Mehidi, A., Strehle, D., Leduc, C., Voituriez, R., Rossier, O., Nassoy, P., and Giannone, G. (2020). Cell stretching is amplified by active actin remodelling to deform and recruit proteins in mechanosensitive structures. Nat. Cell Biol. *22*, 1011–1023. https://doi.org/10.1038/s41556-020-0548-2.

111. Sala, K., Raimondi, A., Tonoli, D., Tacchetti, C., and Curtis, I. de (2018). Identification of a membrane-less compartment regulating invadosome function and motility. Sci. Rep. *8*, 1164. https://doi.org/10.1038/s41598-018-19447-2.

112. Sala, K., Corbetta, A., Minici, C., Tonoli, D., Murray, D.H., Cammarota, E., Ribolla, L., Ramella, M., Fesce, R., Mazza, D., et al. (2019). The ERC1 scaffold protein implicated in cell motility drives the assembly of a liquid phase. Sci. Rep. *9*, 13530. https://doi.org/10.1038/s41598-019-49630-y.

113. Li, Y., Zhang, T., Li, H., Yang, H., Lin, R., Sun, K., Wang, L., Zhang, J., Wei, Z., and Yu, C. (2020). Kindlin2-mediated phase separation underlies integrin adhesion formation. BioRxiv, 2020.07.10.197400. https://doi.org/10.1101/2020.07.10.197400.

114. Zhu, J., Zhou, Q., Xia, Y., Lin, L., Li, J., Peng, M., Zhang, R., and Zhang, M. (2020). GIT/PIX condensates are modular and ideal for distinct compartmentalized cell signaling. Mol. Cell *79*, 782-796.e6. https://doi.org/10.1016/j.molcel.2020.07.004.

115. Wang, Y., Zhang, C., Yang, W., Shao, S., Xu, X., Sun, Y., Li, P., Liang, L., and Wu, C. (2021). LIMD1 phase separation contributes to cellular mechanics and durotaxis by regulating focal adhesion dynamics in response to force. Dev. Cell *56*, 1313-1325.e7. https://doi.org/10.1016/j.devcel.2021.04.002.

116. Guo, K., Zhang, J., Huang, P., Xu, Y., Pan, W., Li, K., Chen, L., Luo, L., Yu, W., Chen, S., et al. (2023). KANK1 shapes focal adhesions by orchestrating protein binding, mechanical force sensing, and phase separation. Cell Rep. *42*, 113321. https://doi.org/10.1016/j.celrep.2023.113321.

117. Litschel, T., Kelley, C.F., Cheng, X., Babl, L., Mizuno, N., Case, L.B., and Schwille, P. (2024). Membrane-induced 2D phase separation of the focal adhesion protein talin. Nat. Commun. *15*, 4986. https://doi.org/10.1038/s41467-024-49222-z.

118. Kumar, A., Tanaka, K., and Schwartz, M.A. (2024). Focal adhesion-derived liquid-liquid phase separations regulate mRNA translation. eLife. https://doi.org/10.7554/elife.96157.1.

119. Rossi, E., Casali, B., Regolisti, G., Davoli, S., Perazzoli, F., Negro, A., Sani, C., Tumiati, B., and Nicoli, D. (1998). Increased plasma levels of platelet-derived growth factor (PDGF-BB + PDGF-AB) in patients with never-treated mild essential hypertension. Am. J. Hypertens. *11*, 1239–1243. https://doi.org/10.1016/s0895-7061(98)00124-1.

120. Murase, K., Fujiwara, T., Umemura, Y., Suzuki, K., Iino, R., Yamashita, H., Saito, M., Murakoshi, H., Ritchie, K., and Kusumi, A. (2004). Ultrafine membrane compartments for molecular diffusion as revealed by single molecule techniques. Biophys. J. *86*, 4075–4093. https://doi.org/10.1529/biophysj.103.035717.

121. Fujiwara, T., Ritchie, K., Murakoshi, H., Jacobson, K., and Kusumi, A. (2002). Phospholipids undergo hop diffusion in compartmentalized cell membrane. J. Cell Biol. *157*, 1071–1082. https://doi.org/10.1083/jcb.200202050.

122. Morone, N., Fujiwara, T., Murase, K., Kasai, R.S., Ike, H., Yuasa, S., Usukura, J., and Kusumi, A. (2006). Three-dimensional reconstruction of the membrane skeleton at the plasma membrane interface by electron tomography. J. Cell Biol. *174*, 851–862. https://doi.org/10.1083/jcb.200606007.

123. Praekelt, U., Kopp, P.M., Rehm, K., Linder, S., Bate, N., Patel, B., Debrand, E., Manso, A.M., Ross, R.S., Conti, F., et al. (2012). New isoform-specific monoclonal antibodies reveal different sub-cellular localisations for talin1 and talin2. Eur. J. Cell Biol. *91*, 180–191. https://doi.org/10.1016/j.ejcb.2011.12.003.

124. Veatch, S.L., Machta, B.B., Shelby, S.A., Chiang, E.N., Holowka, D.A., and Baird, B.A. (2012). Correlation functions quantify super-resolution images and estimate apparent clustering due to over-counting. PLoS One *7*, e31457. https://doi.org/10.1371/journal.pone.0031457.

125. Paolo, G.D., Pellegrini, L., Letinic, K., Cestra, G., Zoncu, R., Voronov, S., Chang, S., Guo, J., Wenk, M.R., and Camilli, P.D. (2002). Recruitment and regulation of phosphatidylinositol phosphate kinase type 1γ by the FERM domain of talin. Nature *420*, 85–89. https://doi.org/10.1038/nature01147.

126. Guercio, J.D.-, Kurzawa, L., Mueller, J., Dimchev, G., Schaks, M., Nemethova, M., Pokrant, T., Brühmann, S., Linkner, J., Blanchoin, L., et al. (2020). Loss of Ena/VASP interferes with lamellipodium architecture, motility and integrin-dependent adhesion. eLife *9*, e55351. https://doi.org/10.7554/elife.55351.

127. Tsunoyama, T.A., Watanabe, Y., Goto, J., Naito, K., Kasai, R.S., Suzuki, K.G.N., Fujiwara, T.K., and Kusumi, A. (2018). Super-long single-molecule tracking reveals dynamic-anchorage-induced integrin function. Nat. Chem. Biol. *14*, 497–506. https://doi.org/10.1038/s41589-018-0032-5.

128. Naruse, K., Sai, X., Yokoyama, N., and Sokabe, M. (1998). Uni-axial cyclic stretch induces c-src activation and translocation in human endothelial cells via SA channel activation. FEBS Lett. *441*, 111–115.

129. Ihara, M., Tomimoto, H., Kitayama, H., Morioka, Y., Akiguchi, I., Shibasaki, H., Noda, M., and Kinoshita, M. (2003). Association of the cytoskeletal GTP-binding protein Sept4/H5 with cytoplasmic inclusions found in Parkinson's disease and other synucleinopathies. J. Biol. Chem. *278*, 24095–24102. https://doi.org/10.1074/jbc.m301352200.

130. Štefanová, I., Hilgert, I., Krištofová, H., Brown, R., Low, M.G., and Hořejši, V. (1989). Characterization of a broadly expressed human leucocyte surface antigen MEM-43 anchored in membrane through phosphatidylinositol. Mol. Immunol. *26*, 153–161. https://doi.org/10.1016/0161-5890(89)90097-7.

131. Madore, N., Smith, K.L., Graham, C.H., Jen, A., Brady, K., Hall, S., and Morris, R. (1999). Functionally different GPI proteins are organized in different domains on the neuronal surface. EMBO J. *18*, 6917–6926. https://doi.org/10.1093/emboj/18.24.6917.

132. Mason, D.W., and Williams, A.F. (1980). The kinetics of antibody binding to membrane antigens in solution and at the cell surface. Biochem. J. *187*, 1–20. https://doi.org/10.1042/bj1870001.

133. Nakamura, A., Oki, C., Kato, K., Fujinuma, S., Maryu, G., Kuwata, K., Yoshii, T., Matsuda, M., Aoki, K., and Tsukiji, S. (2020). Engineering orthogonal, plasma membrane-specific SLIPT systems for multiplexed chemical control of signaling pathways in living single cells. ACS Chem. Biol. *15*, 1004–1015. https://doi.org/10.1021/acschembio.0c00024.

134. McKinney, S.A., Murphy, C.S., Hazelwood, K.L., Davidson, M.W., and Looger, L.L. (2009). A bright and photostable photoconvertible fluorescent protein. Nat. Methods *6*, 131–133. https://doi.org/10.1038/nmeth.1296.

135. Fujiwara, T.K., Takeuchi, S., Kalay, Z., Nagai, Y., Tsunoyama, T.A., Kalkbrenner, T., Iwasawa, K., Ritchie, K.P., Suzuki, K.G.N., and Kusumi, A. (2021). Development of ultrafast camera-based imaging of single fluorescent molecules and live-cell PALM. BioRxiv, 2021.10.26.465864. https://doi.org/10.1101/2021.10.26.465864.

136. Fujiwara, T.K., Takeuchi, S., Kalay, Z., Nagai, Y., Tsunoyama, T.A., Kalkbrenner, T., Chen, L.H., Shibata, A.C.E., Iwasawa, K., Ritchie, K.P., et al. (2021). Focal adhesion membrane is dotted with protein islands and partitioned for molecular hop diffusion. BioRxiv, 2021.10.26.465868. https://doi.org/10.1101/2021.10.26.465868.

137. Bindels, D.S., Haarbosch, L., Weeren, L. van, Postma, M., Wiese, K.E., Mastop, M., Aumonier, S., Gotthard, G., Royant, A., Hink, M.A., et al. (2017). mScarlet: a bright monomeric red fluorescent protein for cellular imaging. Nat. Methods *14*, 53–56. https://doi.org/10.1038/nmeth.4074.

138. Ilić, D., Almeida, E.A.C., Schlaepfer, D.D., Dazin, P., Aizawa, S., and Damsky, C.H. (1998). Extracellular matrix survival signals transduced by focal adhesion kinase suppress p53-mediated apoptosis. J. Cell Biol. *143*, 547–560. https://doi.org/10.1083/jcb.143.2.547.

139. Lee, H.-S., Anekal, P., Lim, C.J., Liu, C.-C., and Ginsberg, M.H. (2013). Two modes of integrin activation form a binary molecular switch in adhesion maturation. Mol. Biol. Cell *24*, 1354–1362. https://doi.org/10.1091/mbc.e12-09-0695.

140. Tsuruta, D., Gonzales, M., Hopkinson, S.B., Otey, C., Khuon, S., Goldman, R.D., and Jones, J.C.R. (2002). Microfilament-dependent movement of the β3 integrin subunit within focal contacts of endothelial cells. FASEB J. *16*, 866–868. https://doi.org/10.1096/fj.01-0878fje.

141. Okrut, J., Prakash, S., Wu, Q., Kelly, M.J.S., and Taunton, J. (2015). Allosteric N-WASP activation by an inter-SH3 domain linker in Nck. Proc. Natl Acad. Sci. USA *112*, E6436–E6445. https://doi.org/10.1073/pnas.1510876112.

142. Sun, Y., Thapa, N., Hedman, A.C., and Anderson, R.A. (2013). Phosphatidylinositol 4,5-bisphosphate: targeted production and signaling. Bioessays *35*, 513–522. https://doi.org/10.1002/bies.201200171.

143. Diamond, L.E., McCurry, K.R., Oldham, E.R., Tone, M., Waldmann, H., Platt, J.L., and Logan, J.S. (1995). Human CD59 expressed in transgenic mouse hearts inhibits the

activation of complement. Transpl. Immunol. *3*, 305–312. https://doi.org/10.1016/0966-3274(95)80016-6.

144. Nemoto, Y.L., Morris, R.J., Hijikata, H., Tsunoyama, T.A., Shibata, A.C.E., Kasai, R.S., Kusumi, A., and Fujiwara, T.K. (2017). Dynamic Meso-Scale Anchorage of GPI-Anchored Receptors in the Plasma Membrane: Prion Protein vs. Thy1. Cell Biochem Biophys *75*, 399–412. https://doi.org/10.1007/s12013-017-0808-3.

145. Johannessen, C.M., Boehm, J.S., Kim, S.Y., Thomas, S.R., Wardwell, L., Johnson, L.A., Emery, C.M., Stransky, N., Cogdill, A.P., Barretina, J., et al. (2010). COT drives resistance to RAF inhibition through MAP kinase pathway reactivation. Nature *468*, 968–972. https://doi.org/10.1038/nature09627.

146. Jones, N.P., Peak, J., Brader, S., Eccles, S.A., and Katan, M. (2005). PLCγ1 is essential for early events in integrin signalling required for cell motility. J. Cell Sci. *118*, 2695–2706. https://doi.org/10.1242/jcs.02374.

147. Ishida, S., Matsu-ura, T., Fukami, K., Michikawa, T., and Mikoshiba, K. (2014). Phospholipase C-β1 and β4 contribute to non-genetic cell-to-cell variability in histamine-induced calcium signals in HeLa cells. PLoS One *9*, e86410. https://doi.org/10.1371/journal.pone.0086410.

148. Lindberg, F.P., Gresham, H.D., Schwarz, E., and Brown, E.J. (1993). Molecular cloning of integrin-associated protein: an immunoglobulin family member with multiple membrane-spanning domains implicated in alpha v beta 3-dependent ligand binding. J. Cell Biol. *123*, 485–496. https://doi.org/10.1083/jcb.123.2.485.

149. Johnson, B.B., Moe, P.C., Wang, D., Rossi, K., Trigatti, B.L., and Heuck, A.P. (2012). Modifications in perfringolysin O domain 4 alter the cholesterol concentration threshold required for binding. Biochemistry *51*, 3373–3382. https://doi.org/10.1021/bi3003132.

150. Maekawa, M., and Fairn, G.D. (2015). Complementary probes reveal that phosphatidylserine is required for the proper transbilayer distribution of cholesterol. J. Cell Sci. *128*, 1422–1433. https://doi.org/10.1242/jcs.164715.

151. Schindelin, J., Arganda-Carreras, I., Frise, E., Kaynig, V., Longair, M., Pietzsch, T., Preibisch, S., Rueden, C., Saalfeld, S., Schmid, B., et al. (2012). Fiji: an open-source platform for biological-image analysis. Nat. Methods *9*, 676–682. https://doi.org/10.1038/nmeth.2019.

152. Ovesný, M., Křížek, P., Borkovec, J., Švindrych, Z., and Hagen, G.M. (2014). ThunderSTORM: a comprehensive ImageJ plug-in for PALM and STORM data analysis and

super-resolution imaging. Bioinformatics *30*, 2389–2390. https://doi.org/10.1093/bioinformatics/btu202.

153. Berg, S., Kutra, D., Kroeger, T., Straehle, C.N., Kausler, B.X., Haubold, C., Schiegg, M., Ales, J., Beier, T., Rudy, M., et al. (2019). ilastik: interactive machine learning for (bio)image analysis. Nat. Methods *16*, 1226–1232. https://doi.org/10.1038/s41592-019-0582-9.

154. Hooper, M., Hardy, K., Handyside, A., Hunter, S., and Monk, M. (1987). HPRT-deficient (Lesch–Nyhan) mouse embryos derived from germline colonization by cultured cells. Nature *326*, 292–295. https://doi.org/10.1038/326292a0.

155. Xia, S., Lim, Y.B., Zhang, Z., Wang, Y., Zhang, S., Lim, C.T., Yim, E.K.F., and Kanchanawong, P. (2019). Nanoscale architecture of the cortical actin cytoskeleton in embryonic stem cells. Cell Rep. *28*, 1251-1267.e7. https://doi.org/10.1016/j.celrep.2019.06.089.

156. Fujiwara, T.K., Takeuchi, S., Kalay, Z., Nagai, Y., Tsunoyama, T.A., Kalkbrenner, T., Iwasawa, K., Ritchie, K.P., Suzuki, K.G.N., and Kusumi, A. (2023). Development of ultrafast camera-based single fluorescent-molecule imaging for cell biology. J. Cell Biol. *222*, e202110160. https://doi.org/10.1083/jcb.202110160.

157. Suzuki, K.G., Kasai, R.S., Hirosawa, K.M., Nemoto, Y.L., Ishibashi, M., Miwa, Y., Fujiwara, T.K., and Kusumi, A. (2012). Transient GPI-anchored protein homodimers are units for raft organization and function. Nat. Chem. Biol. *8*, 774–783. https://doi.org/10.1038/nchembio.1028.

158. Sun, H., and Taneja, R. (2007). Analysis of transformation and tumorigenicity using mouse embryonic fibroblast cells. Methods Mol. Biol. *383*, 303–310. https://doi.org/10.1007/978-1-59745-335-6_19.

159. Harris, C.L., Hanna, S.M., Mizuno, M., Holt, D.S., Marchbank, K.J., and Morgan, B.P. (2003). Characterization of the mouse analogues of CD59 using novel monoclonal antibodies: tissue distribution and functional comparison. Immunology *109*, 117–126. https://doi.org/10.1046/j.1365-2567.2003.01628.x.

160. Hanke, J.H., Gardner, J.P., Dow, R.L., Changelian, P.S., Brissette, W.H., Weringer, E.J., Pollok, B.A., and Connelly, P.A. (1996). Discovery of a novel, potent, and Src family-selective tyrosine kinase inhibitor. J. Biol. Chem. *271*, 695–701. https://doi.org/10.1074/jbc.271.2.695.

161. Slack-Davis, J.K., Martin, K.H., Tilghman, R.W., Iwanicki, M., Ung, E.J., Autry, C., Luzzio, M.J., Cooper, B., Kath, J.C., Roberts, W.G., et al. (2007). Cellular characterization

of a novel focal adhesion kinase inhibitor. J. Biol. Chem. *282*, 14845–14852. https://doi.org/10.1074/jbc.m606695200.

162. Kosenko, A., and Hoshi, N. (2013). A change in configuration of the calmodulin-KCNQ channel complex underlies Ca^{2+}-dependent modulation of KCNQ channel activity. PLoS One *8*, e82290. https://doi.org/10.1371/journal.pone.0082290.

163. Johnson, K.A., Budicini, M.R., Bhattarai, N., Sharma, T., Urata, S., Gerstman, B.S., Chapagain, P.P., Li, S., and Stahelin, R.V. (2024). PI(4,5)P2 binding sites in the Ebola virus matrix protein VP40 modulate assembly and budding. J. Lipid Res. *65*, 100512. https://doi.org/10.1016/j.jlr.2024.100512.

164. Ulianov, S.V., Velichko, A.K., Magnitov, M.D., Luzhin, A.V., Golov, A.K., Ovsyannikova, N., Kireev, I.I., Gavrikov, A.S., Mishin, A.S., Garaev, A.K., et al. (2021). Suppression of liquid–liquid phase separation by 1,6-hexanediol partially compromises the 3D genome organization in living cells. Nucleic Acids Res. *49*, 10524–10541. https://doi.org/10.1093/nar/gkab249.

165. Zhou, P., Kasai, R.S., Fujita, W., Tsunoyama, T.A., Neyama, H., Ueda, H., Yokoyama, T., Sakamoto, M., Pigolotti, S., Fujiwara, T.K., et al. (2025). Single-molecule characterization of opioid receptor heterodimers reveals soluble μ-δ dimer blocker peptide alleviates morphine tolerance. Nat. Commun. *16*, 9859. https://doi.org/10.1038/s41467-025-64695-2.

166. Koyama-Honda, I., Ritchie, K., Fujiwara, T., Iino, R., Murakoshi, H., Kasai, R.S., and Kusumi, A. (2005). Fluorescence imaging for monitoring the colocalization of two single molecules in living cells. Biophys. J. *88*, 2126–2136. https://doi.org/10.1529/biophysj.104.048967.

167. Shibata, A.C., Fujiwara, T.K., Chen, L., Suzuki, K.G., Ishikawa, Y., Nemoto, Y.L., Miwa, Y., Kalay, Z., Chadda, R., Naruse, K., et al. (2012). Archipelago architecture of the focal adhesion: membrane molecules freely enter and exit from the focal adhesion zone. Cytoskeleton *69*, 380–392. https://doi.org/10.1002/cm.21032.

168. Sahl, S.J., Leutenegger, M., Hilbert, M., Hell, S.W., and Eggeling, C. (2010). Fast molecular tracking maps nanoscale dynamics of plasma membrane lipids. Proc. Natl Acad. Sci. USA *107*, 6829–6834. https://doi.org/10.1073/pnas.0912894107.

169. Zhou, P., Tsunoyama, T.A., Kasai, R.S., Hirosawa, K.M., Kalay, Z., Aladag, A., Fujiwara, T., Pigolotti, S., and Kusumi, A. (2024). Single-molecule detection of transient dimerization of opioid receptors 1: Homodimers' effect on signaling and internalization. bioRxiv, 2024.07.25.605080. https://doi.org/10.1101/2024.07.25.605080.

170. Xu, K., Zhong, G., and Zhuang, X. (2013). Actin, spectrin, and associated proteins form a periodic cytoskeletal structure in axons. Science *339*, 452–456. https://doi.org/10.1126/science.1232251.

171. Tanaka, K.A.K., Suzuki, K.G.N., Shirai, Y.M., Shibutani, S.T., Miyahara, M.S.H., Tsuboi, H., Yahara, M., Yoshimura, A., Mayor, S., Fujiwara, T.K., et al. (2010). Membrane molecules mobile even after chemical fixation. Nat Methods *7*, 865–866. https://doi.org/10.1038/nmeth.f.314.

172. Lee, S.-H., Shin, J.Y., Lee, A., and Bustamante, C. (2012). Counting single photoactivatable fluorescent molecules by photoactivated localization microscopy (PALM). Proc. Natl Acad. Sci. USA *109*, 17436–17441. https://doi.org/10.1073/pnas.1215175109.

173. Zitter, E.D., Thédié, D., Mönkemöller, V., Hugelier, S., Beaudouin, J., Adam, V., Byrdin, M., Meervelt, L.V., Dedecker, P., and Bourgeois, D. (2019). Mechanistic investigation of mEos4b reveals a strategy to reduce track interruptions in sptPALM. Nat. Methods *16*, 707–710. https://doi.org/10.1038/s41592-019-0462-3.

174. Dundr, M., and Misteli, T. (2003). Measuring dynamics of nuclear proteins by photobleaching. Curr. Protoc. Cell Biol. *18*, 13.5.1-13.5.18. https://doi.org/10.1002/0471143030.cb1305s18.

175. Otsu, N. (1979). A threshold selection method from gray-level histograms. IEEE Trans. Syst. Man Cybern. *9*, 62–66. https://doi.org/10.1109/tsmc.1979.4310076.

176. Anthis, N.J., and Clore, G.M. (2013). Sequence-specific determination of protein and peptide concentrations by absorbance at 205 nm: sequence-specific protein concentration at 205 nm. Protein Sci. *22*, 851–858. https://doi.org/10.1002/pro.2253.

177. Tomayko, M.M., and Reynolds, C.P. (1989). Determination of subcutaneous tumor size in athymic (nude) mice. Cancer Chemother. Pharmacol. *24*, 148–154. https://doi.org/10.1007/bf00300234.

178. Tan, C., Jung, J., Kobayashi, C., Torre, D.U.L., Takada, S., and Sugita, Y. (2022). Implementation of residue-level coarse-grained models in GENESIS for large-scale molecular dynamics simulations. PLoS Comput. Biol. *18*, e1009578. https://doi.org/10.1371/journal.pcbi.1009578.

179. Jung, J., Yagi, K., Tan, C., Oshima, H., Mori, T., Yu, I., Matsunaga, Y., Kobayashi, C., Ito, S., Torre, D.U.L., et al. (2024). GENESIS 2.1: High-performance molecular dynamics software for enhanced sampling and free-energy calculations for atomistic, coarse-grained, and quantum mechanics/molecular mechanics models. J. Phys. Chem. B *128*, 6028–6048. https://doi.org/10.1021/acs.jpcb.4c02096.

2655 180. Jung, J., Tan, C., and Sugita, Y. (2024). GENESIS CGDYN: large-scale coarse-grained MD simulation with dynamic load balancing for heterogeneous biomolecular systems. Nat. Commun. *15*, 3370. https://doi.org/10.1038/s41467-024-47654-1.

Figure 1

Engaged RTKs and clustered GPI-anchored receptors are transiently recruited to talin clusters (talin-rescued dKO MEFs)

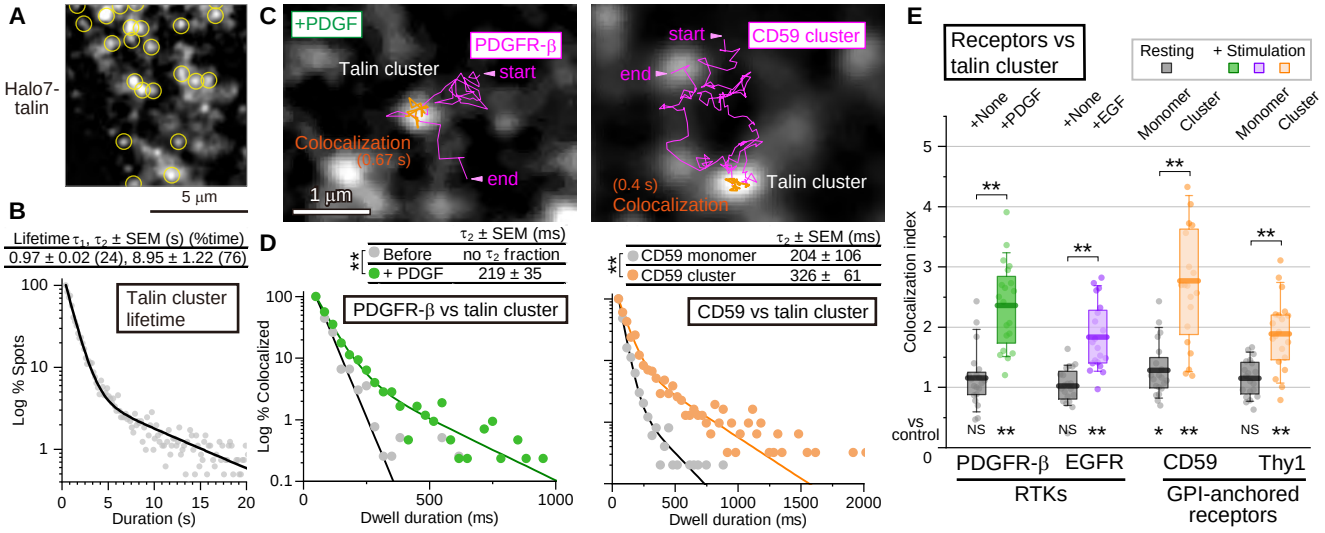

Talin clusters are broadly found across cell lines

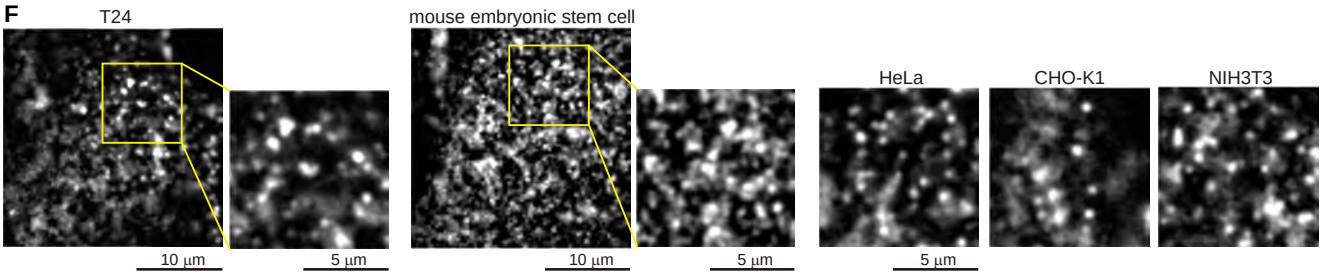

Simultaneous single-particle tracking of talin clusters, CD59 clusters, and PLCγ1 (T24-T cells)

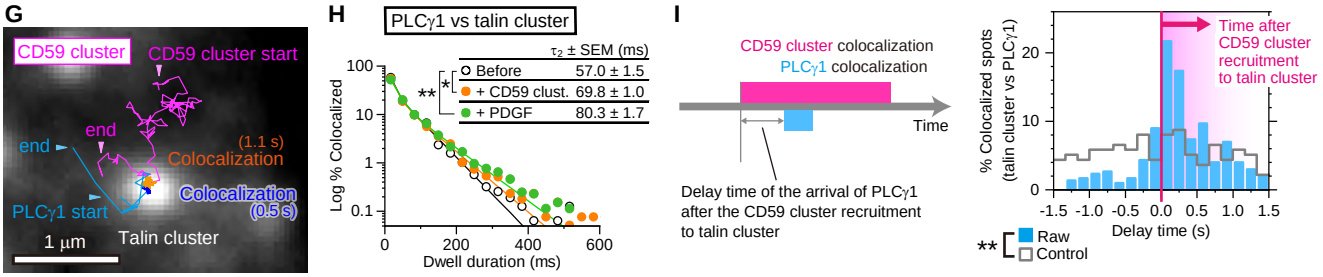

Talin clusters are sites for CD59-mediated immune evasion from CDC (T24-T cells)

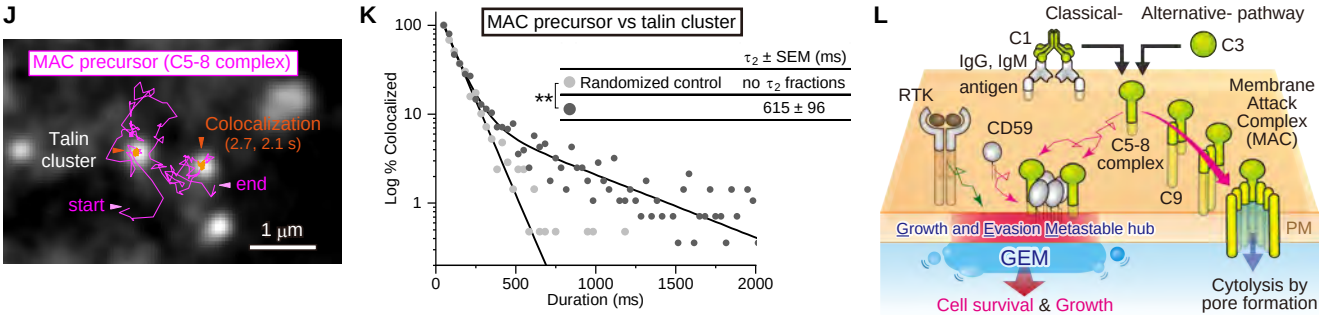

Figure 2

Talin and zyxin co-cluster (≈8.5-s lifetime)

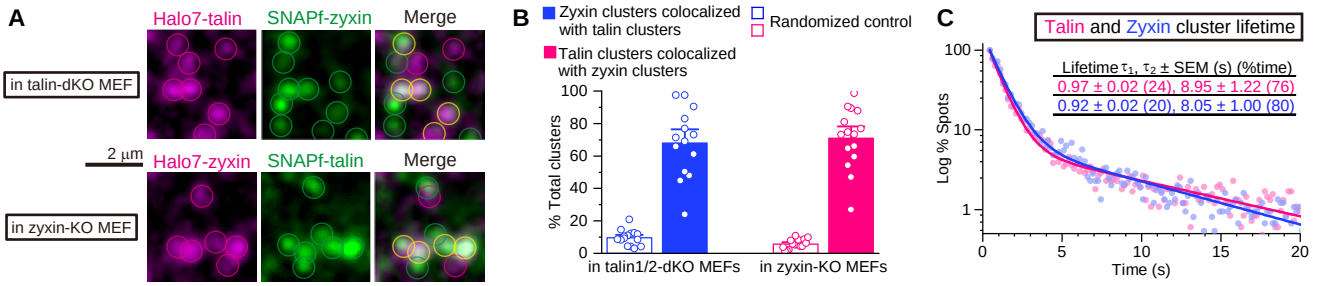

Broad talin–zyxin stoichiometries and dynamic talin residency in GEMs

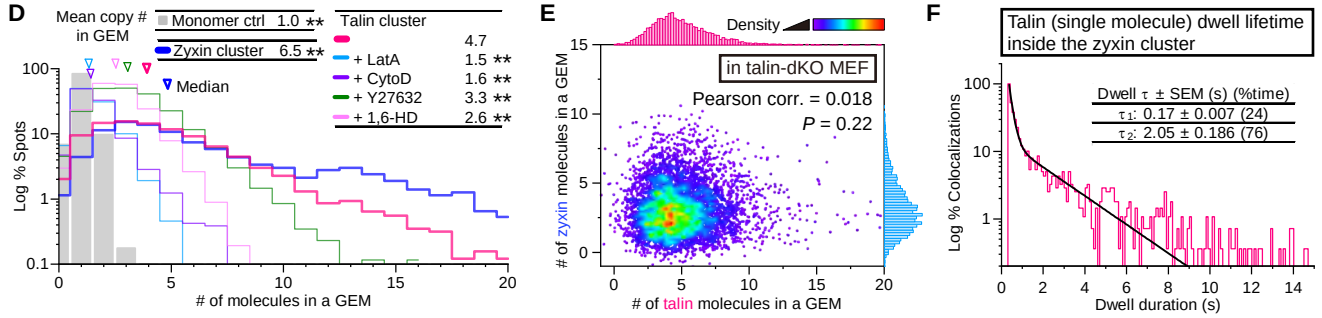

GEM density on the apical PM (KO MEFs) and GEM constituent molecules (T24-T cells)

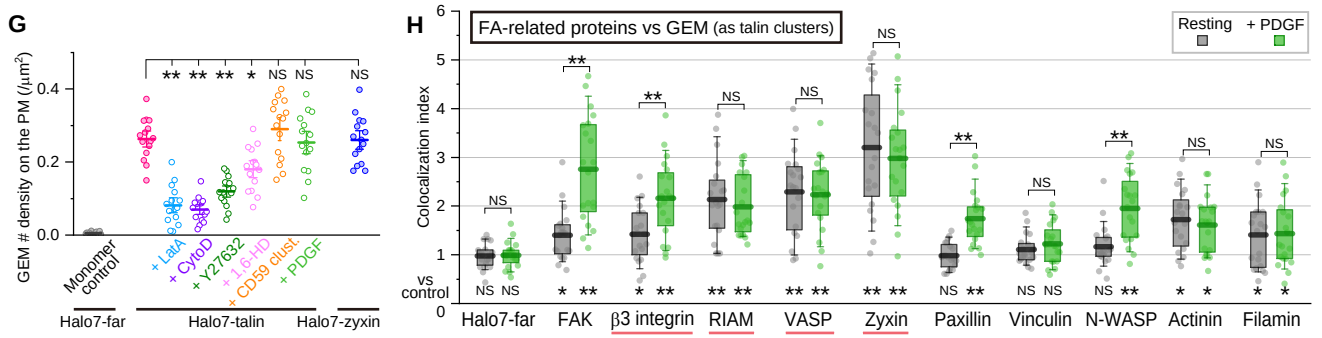

Lipid colocalizations with GEM (T24-T cells)

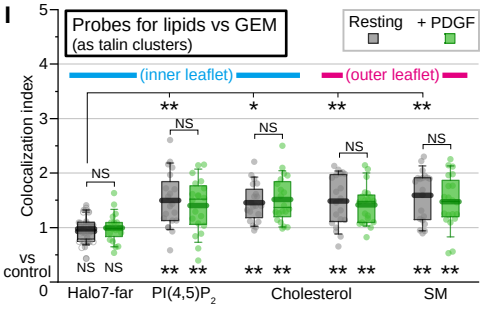

PI(4,5)P_2 or cholesterol depletion decreases GEM density in the PM and size (talin-rescued dKO MEFs)

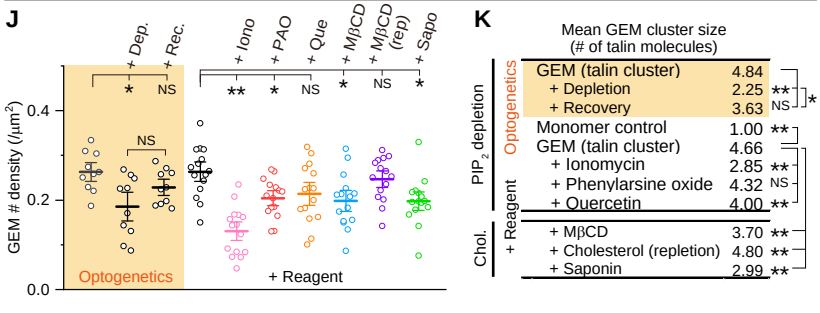

Conventional and PALM super-resolution images of mEos3.2-talin

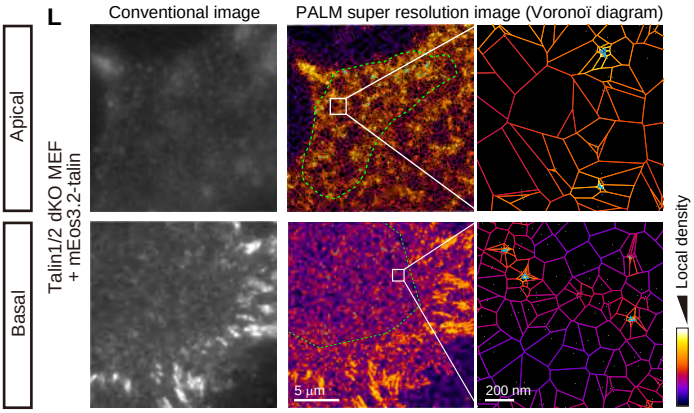

GEM's molecular composition and association with lipids and actin

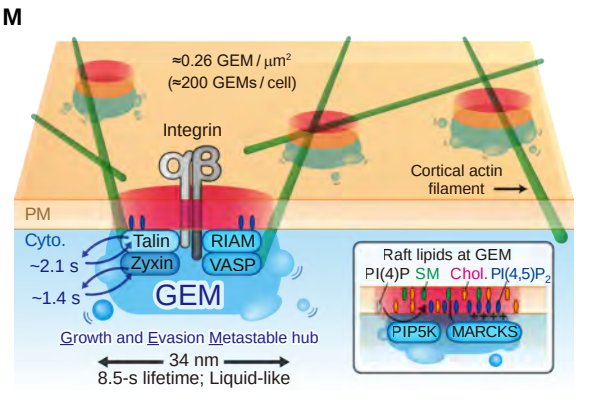

Figure 3

[*In vitro*] Co-condensation of zyxin and VASP

[*In vitro* and in cells] Micron-scale zyxin–VASP co-condensates at high concentrations

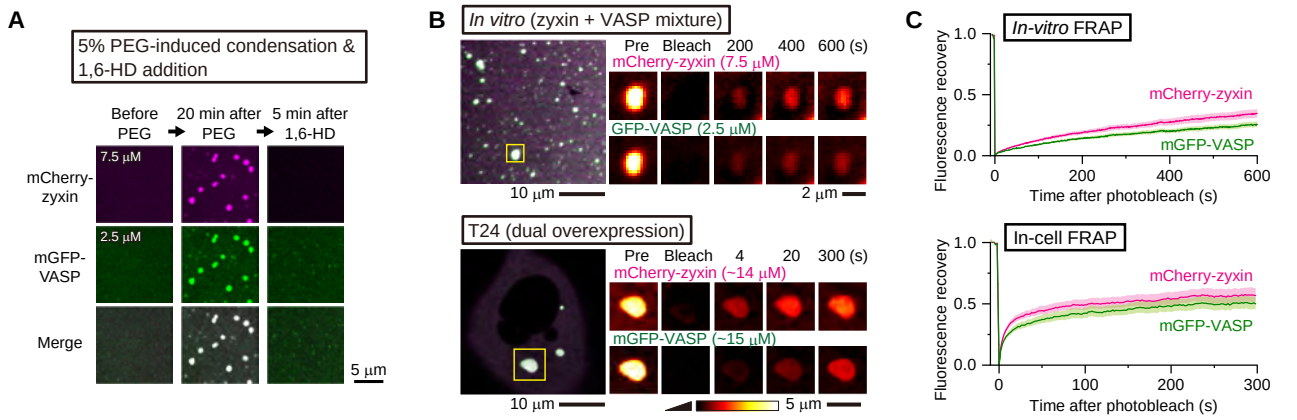

Coarse-grained MD simulations of zyxin IDR2 condensates with inter-chain contact analysis

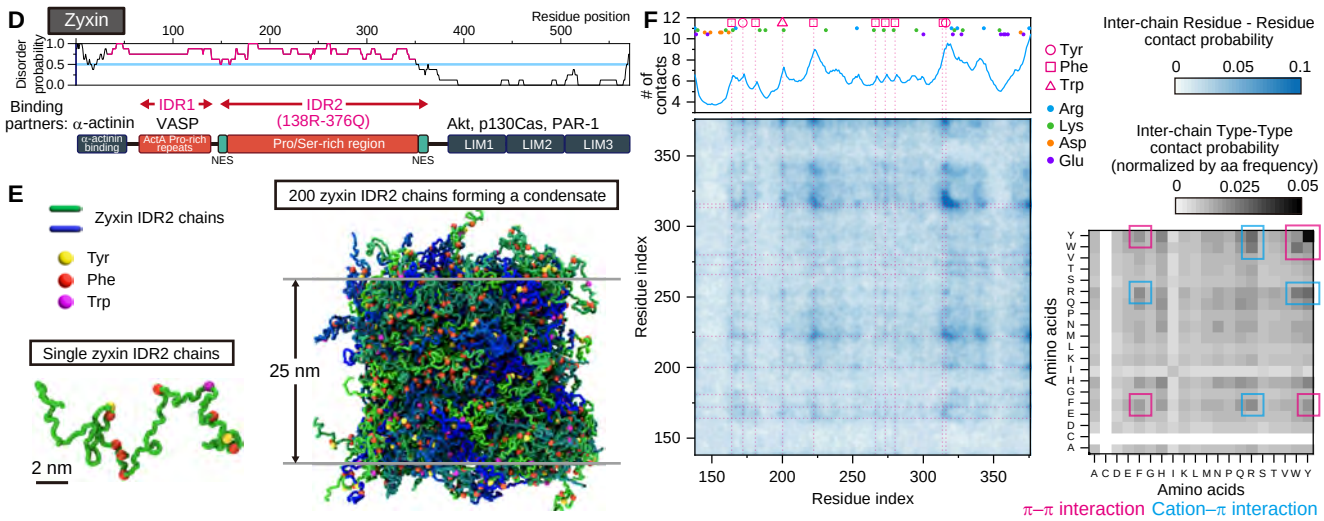

[In cells and *in vitro*] Micron-scale condensates are absent at endogenous zyxin/VASP levels; RIAM remains non-condensing even when overexpressed

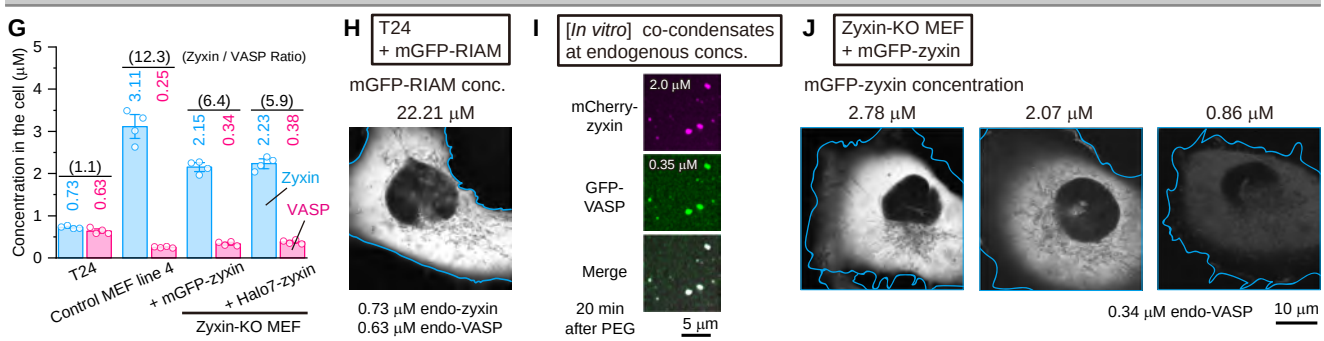

[In cells] GEM shows liquid-like dynamics with merging and splitting (zyxin-rescued KO MEFs)

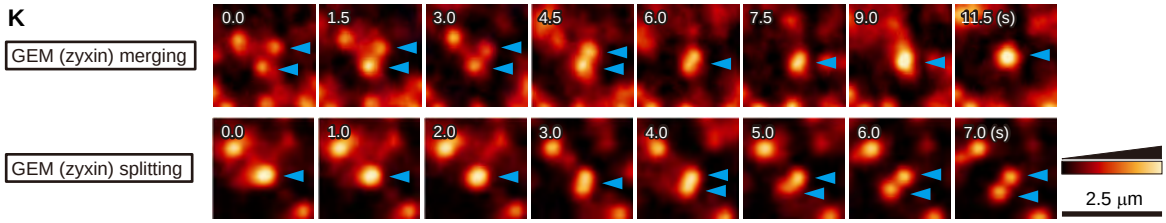

Figure 4

Domain schematics of zyxin and VASP constructs used in this study

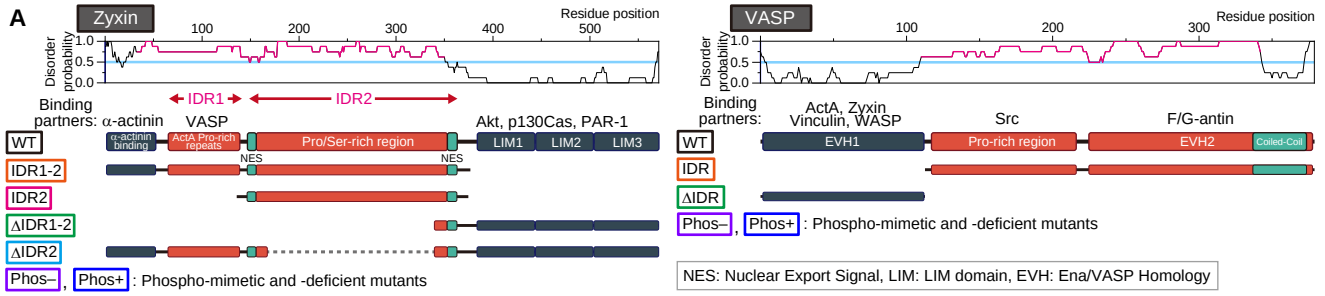

[*In vitro*] IDR2 (but not ΔIDR2) forms condensates

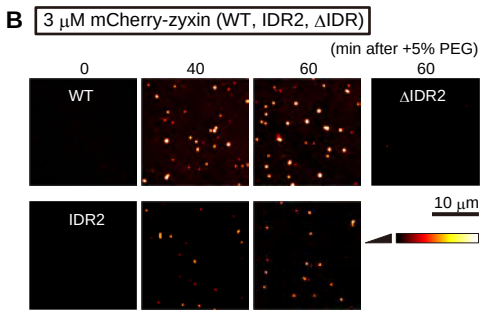

Single-molecule colocalization indexes with GEM (T24-T cells)

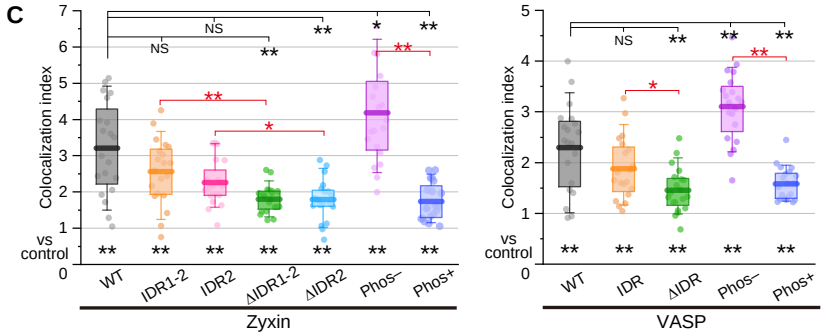

Establishing rescued zyxin-KO MEF lines and confirming cellular localization of zyxin constructs

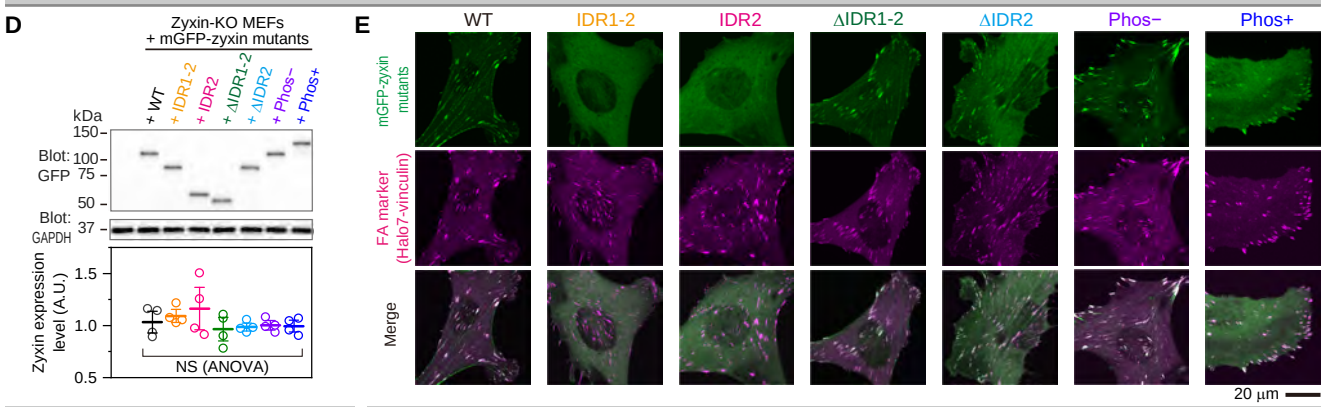

Liquid-like IDR2 clusters in the cell

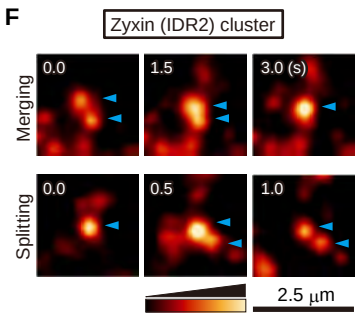

Zyxin's IDRs facilitate GEM formation (zyxin-KO MEFs rescued with zyxin constructs)

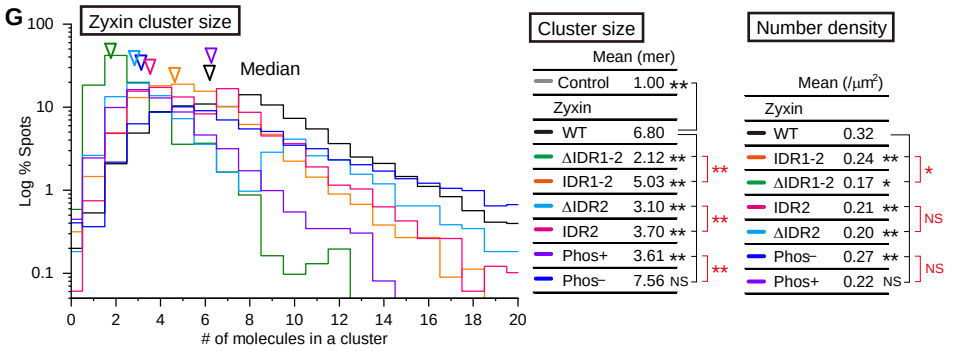

Figure 5

Various downstream signaling molecules are colocalized with GEM (T24-T cells)

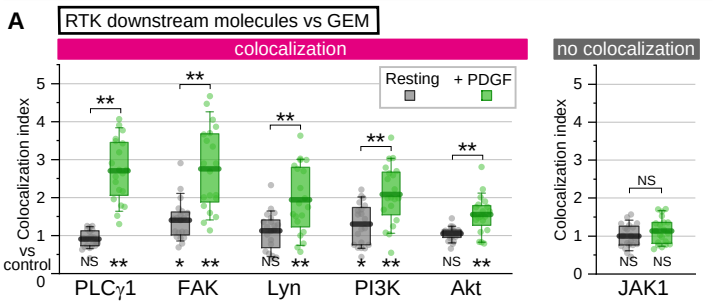

PDGF enhances FAK recruitment and dwell at GEM (T24-T cells)

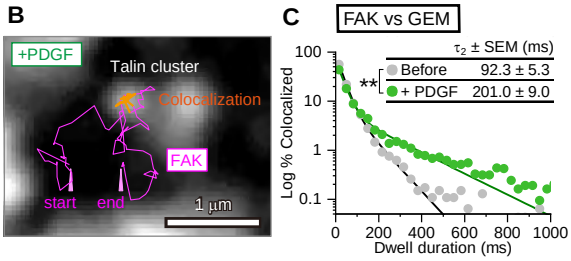

Receptors and downstream molecules recruited to GEM

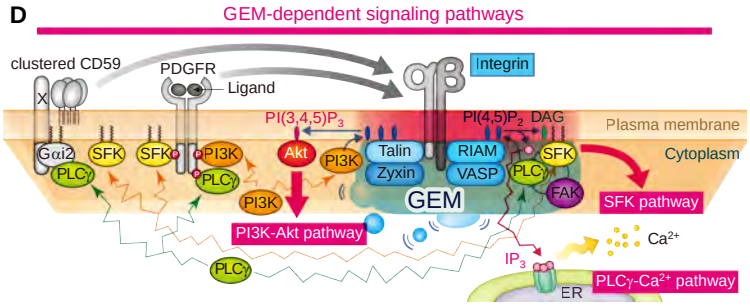

Stimulation-induced PLCγ1 recruitment to GEM requires both FAK and SFK activities (T24-T cells)

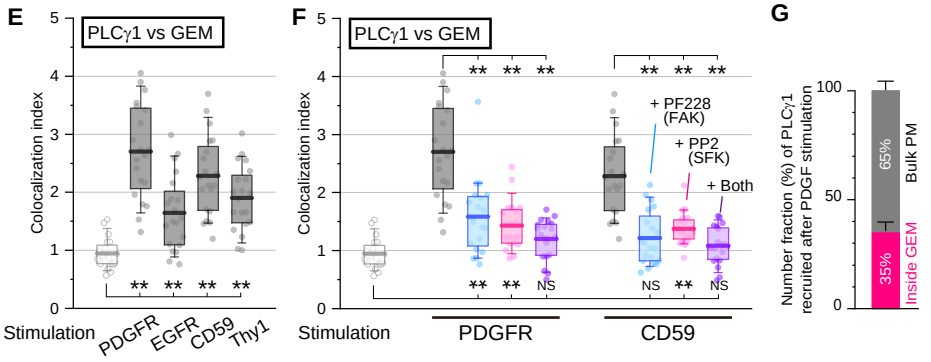

Zyxin IDR2 enables Ca^{2+} and Akt activation

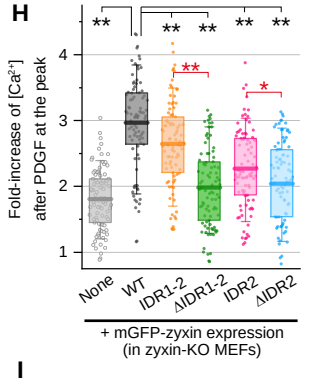

CD59 prolongs MAC-precursor dwell lifetime at GEM (zyxin-rescued KO MEFs ± sh-CD59)

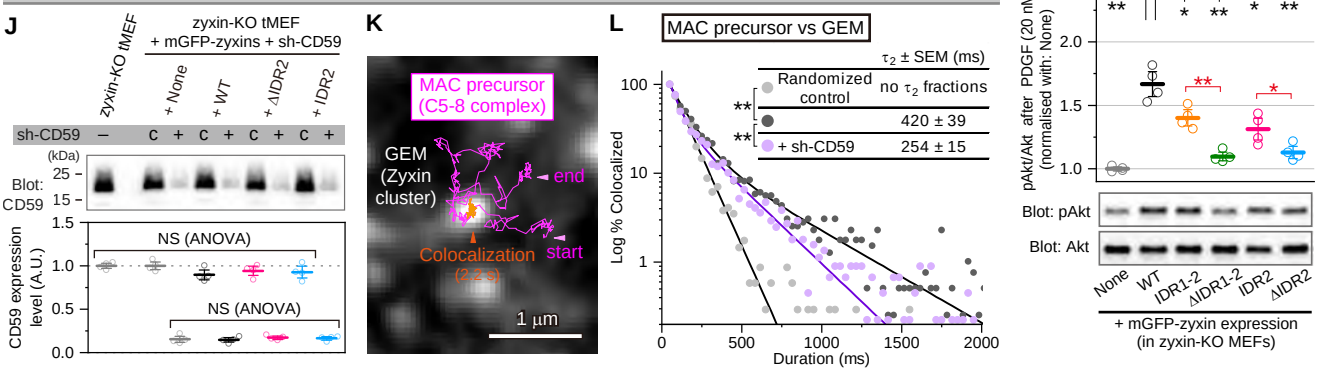

Zyxin IDR2 is essential for CD59-mediated CDC evasion and cell proliferation (zyxin-rescued KO MEFs ± sh-CD59)

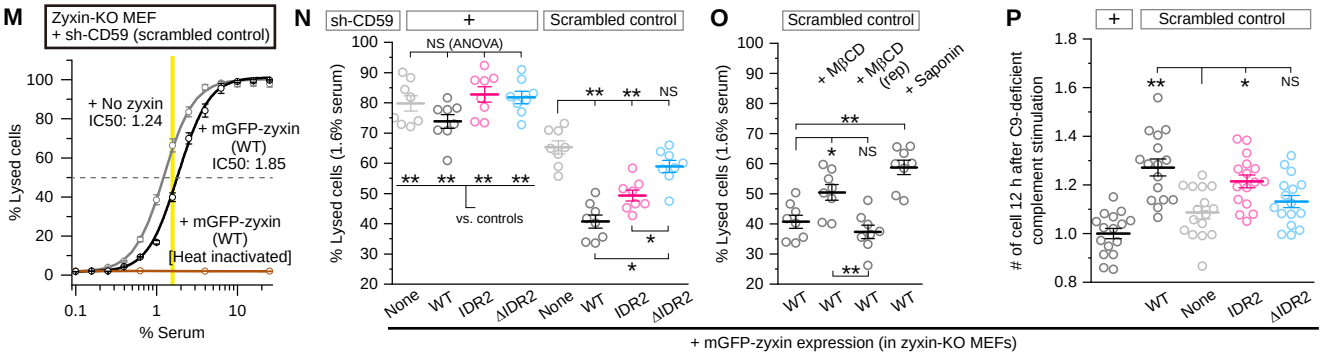

Figure 6

Mild PDGFR+CD59 co-stimulation supralinearly enhances PLCγ1 recruitment to GEM

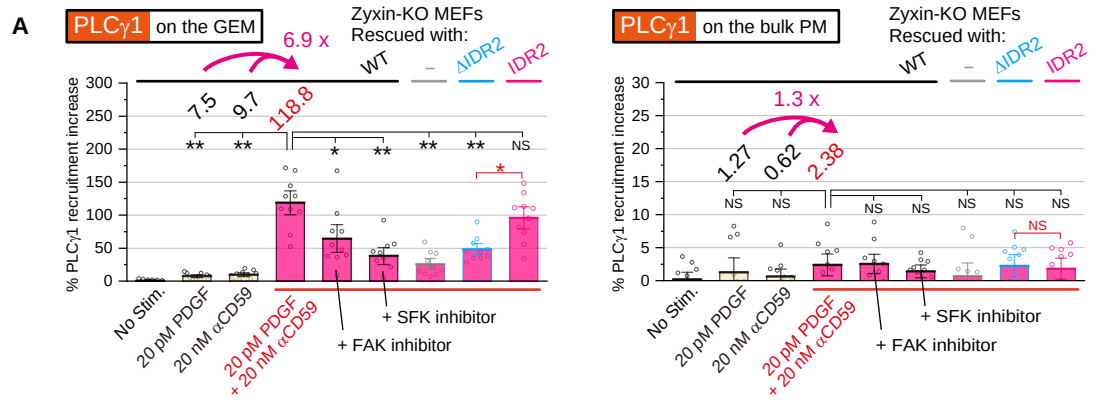

Mild PDGFR+CD59 co-stimulation supralinearly enhances Ca^{2+} signals

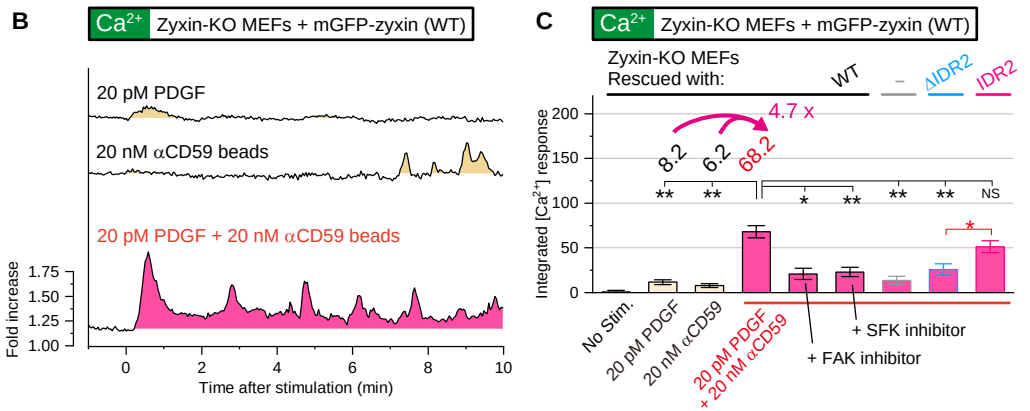

Co-stimulation enhances PI3K

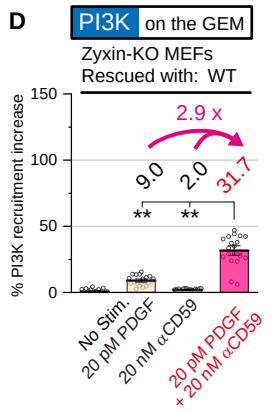

Integrin, FAK, Lyn, and PLCγ1 recruitment after single vs combined mild stimulations

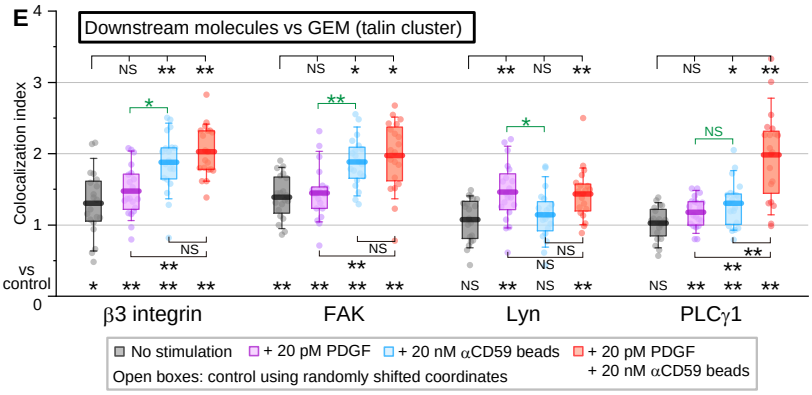

Kinase spiral model for CD59–PDGFR signal integration

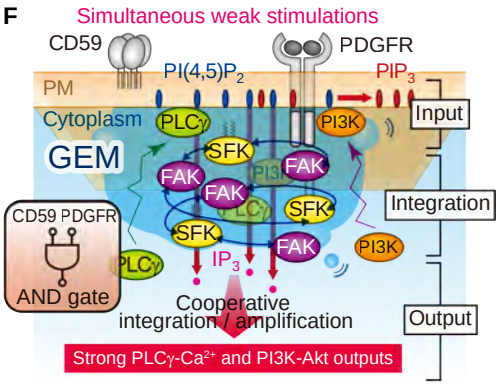

Figure 7

Zyxin IDR2–rescued GEM enhances tumor growth in mice

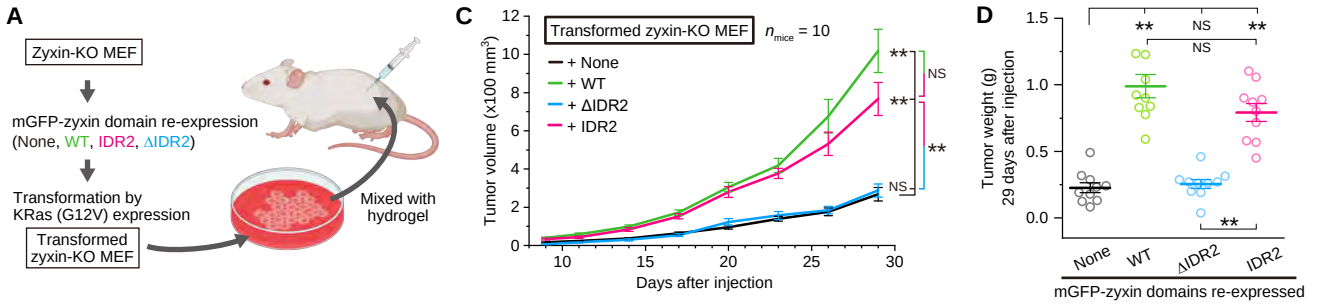

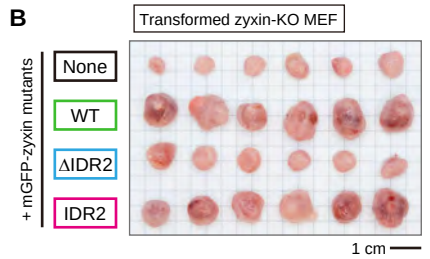

FAK and Akt activation in mouse tumors depends on zyxin IDR2

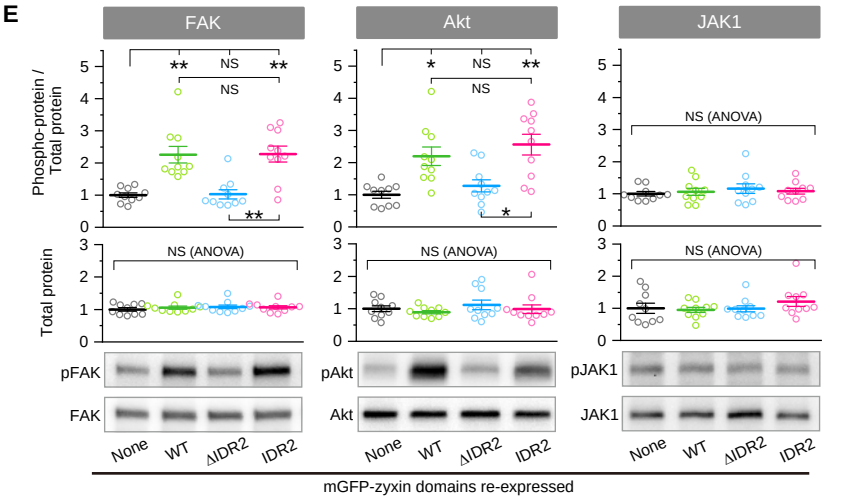

CD59 enhances zyxin IDR2–rescued GEM–driven tumor growth

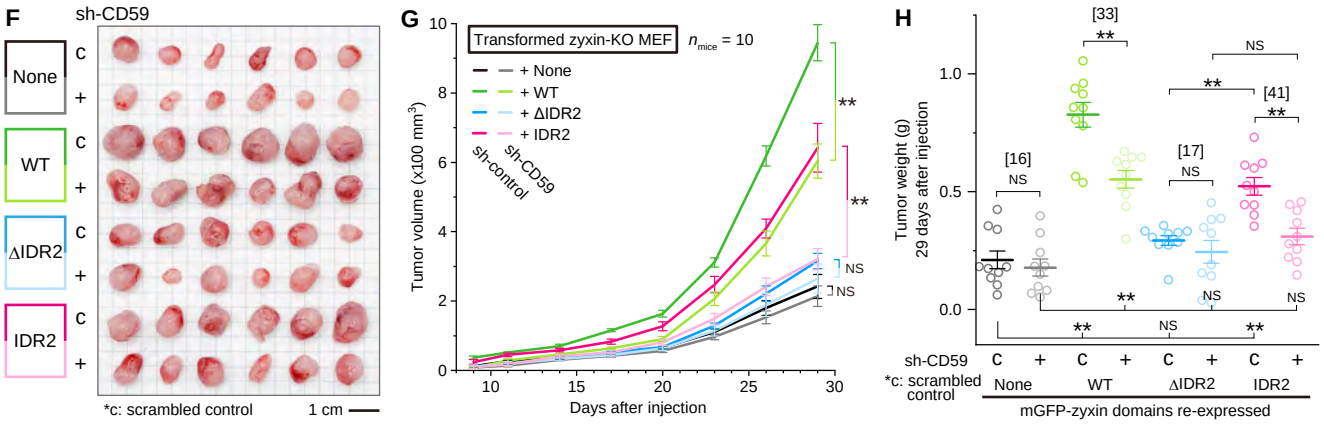

Summary of GEM formation, structure, and function

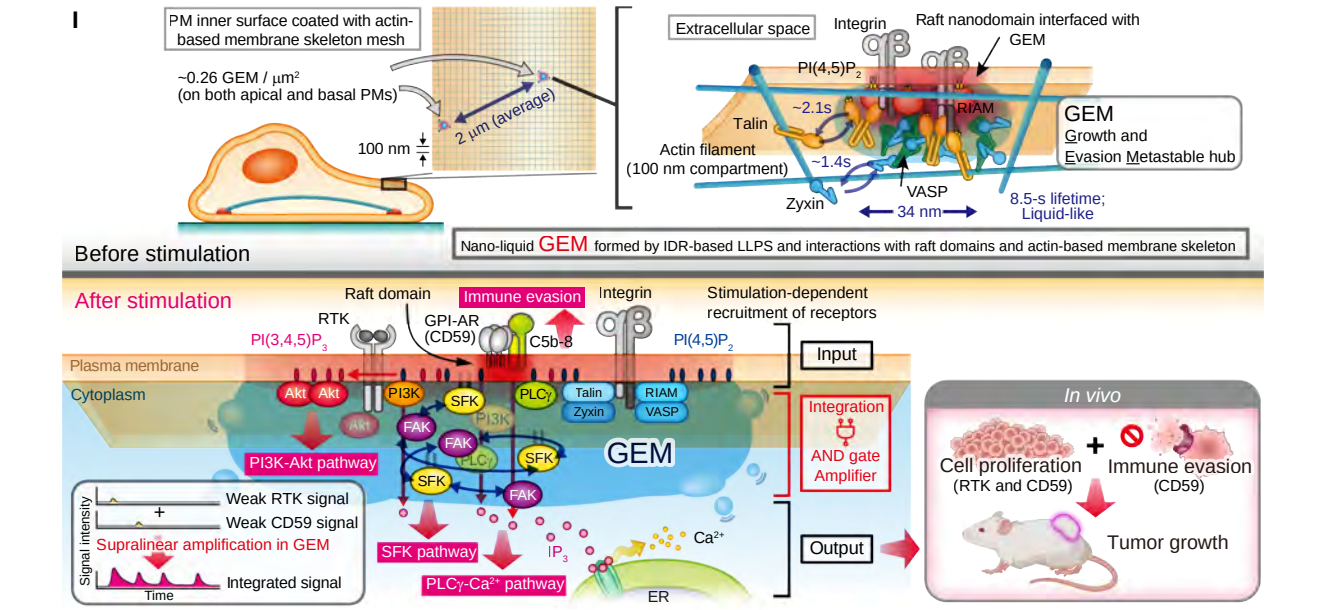

Figure S1

Establishing talin1/2-dKO MEF lines rescued with functional tagged talins (near-endogenous levels)

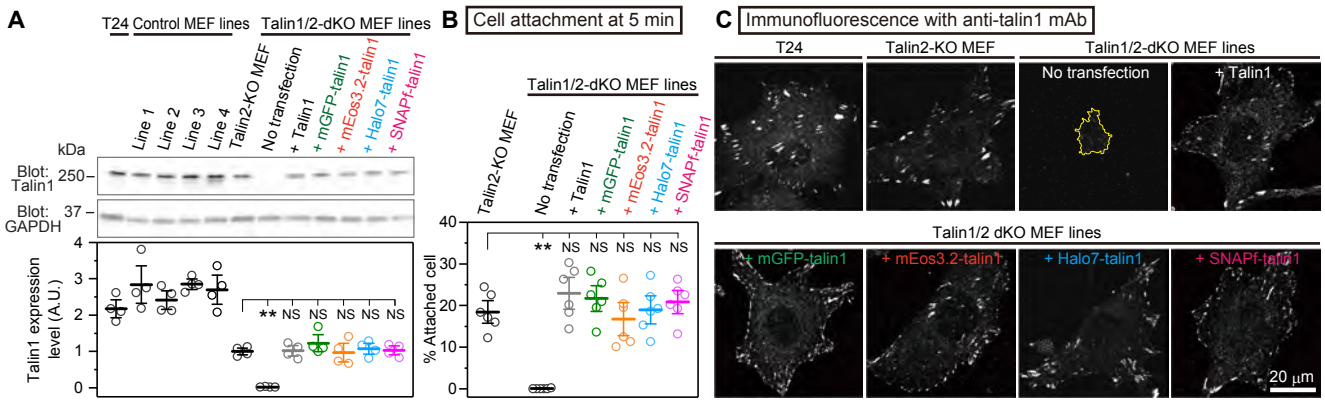

Establishing zyxin-KO MEF lines rescued with functional tagged zyxins (near-endogenous levels)

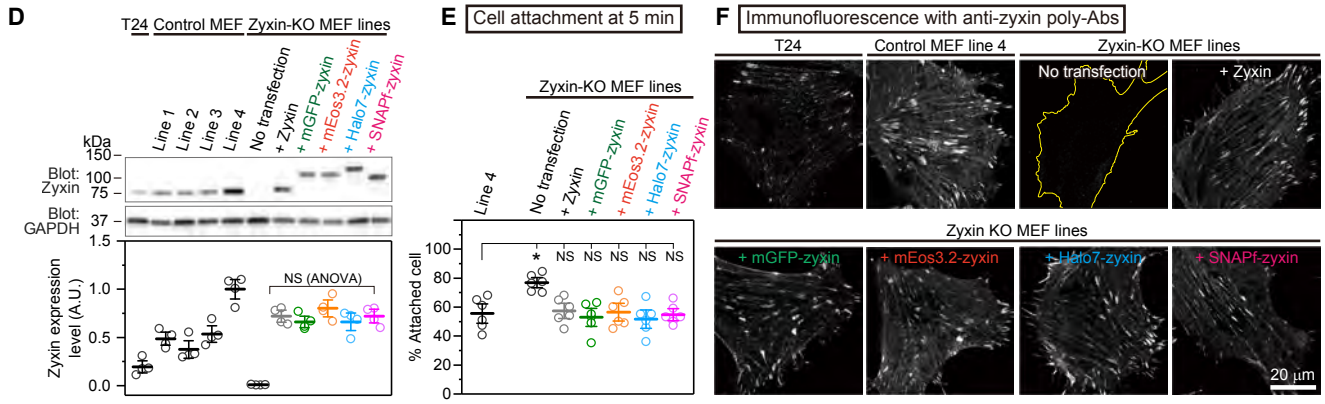

Detection of talin and zyxin clusters (rescued KO MEFs)

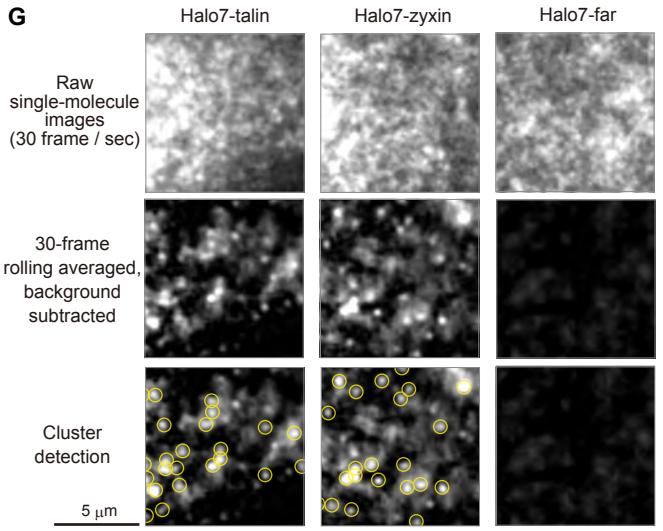

Definition of the single-molecule colocalization index based on PCCF

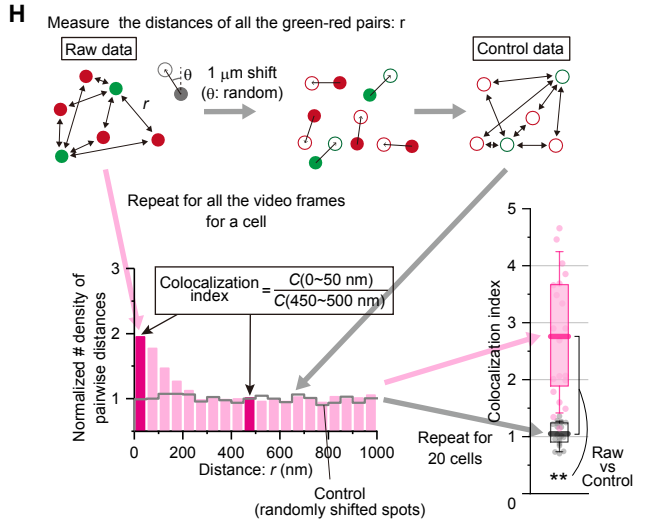

Generation of the T24-T cell line

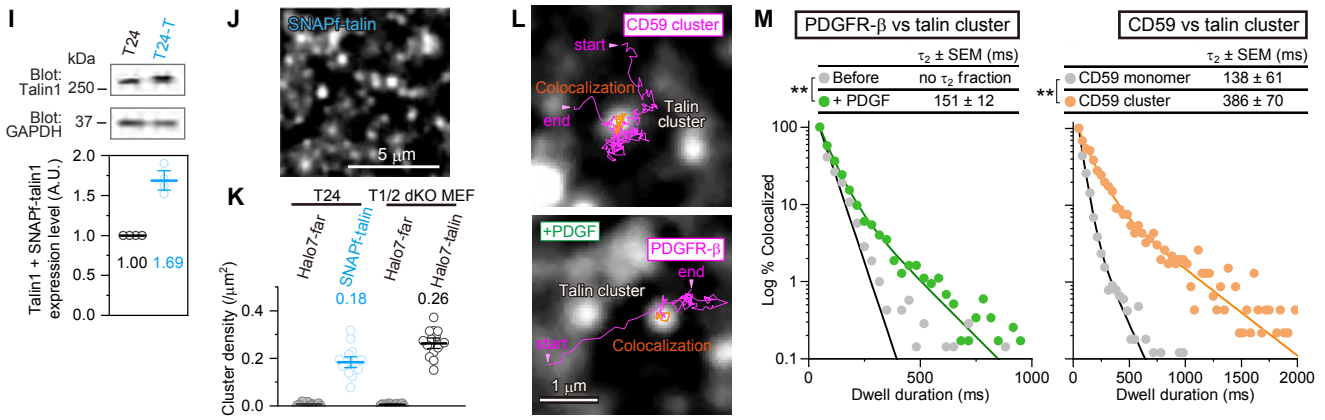

Figure S2

Lifetimes of talin-identified and zyxin-identified GEMs: Long-lived GEMs require both talin and zyxin (rescued KO MEFs)

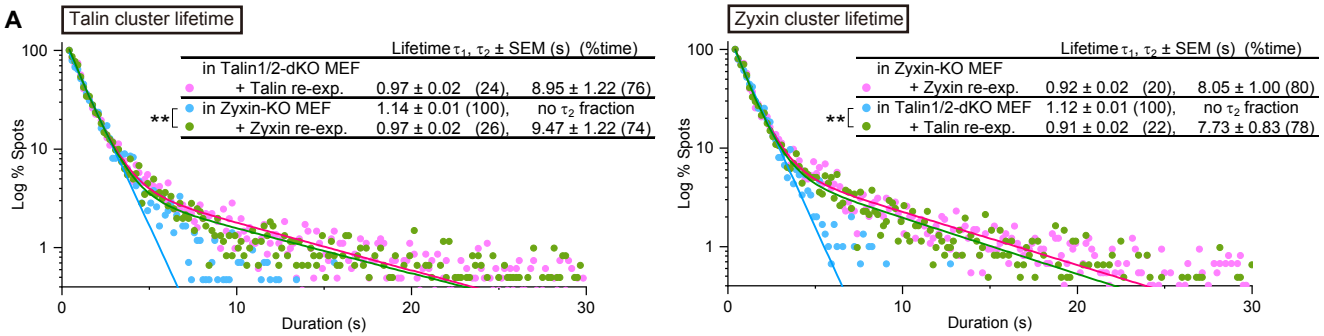

Broad talin–zyxin stoichiometries and dynamic zyxin residency in GEMs

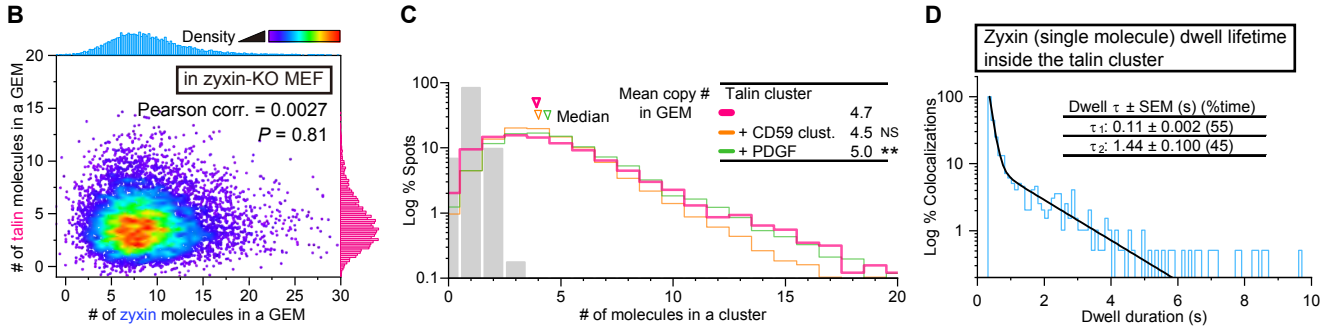

FA- and actin-related proteins and their interactions

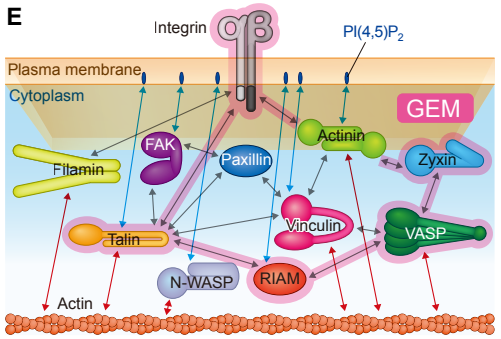

Figure S3

Single-molecule colocalization with GEM: lipid probes, MARCKS, PIP5K, and PI3K (T24-T)

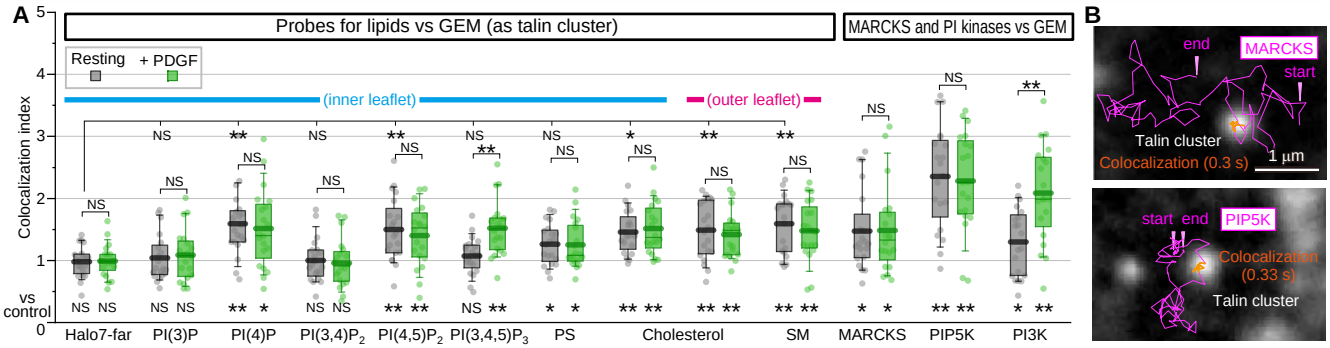

Partial cholesterol depletion reduces GEM size (talin-rescued dKO MEFs)

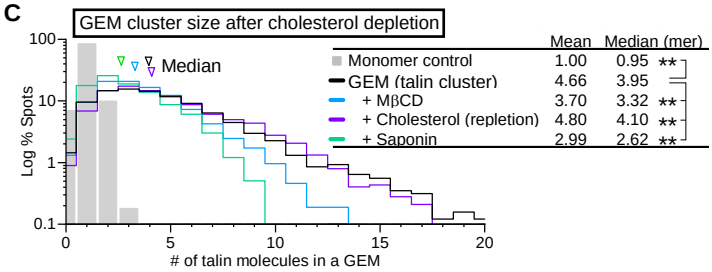

Optogenetic partial PI(4,5)P$_2$ depletion reduces GEM size and density on the PM (talin-rescued dKO MEFs)

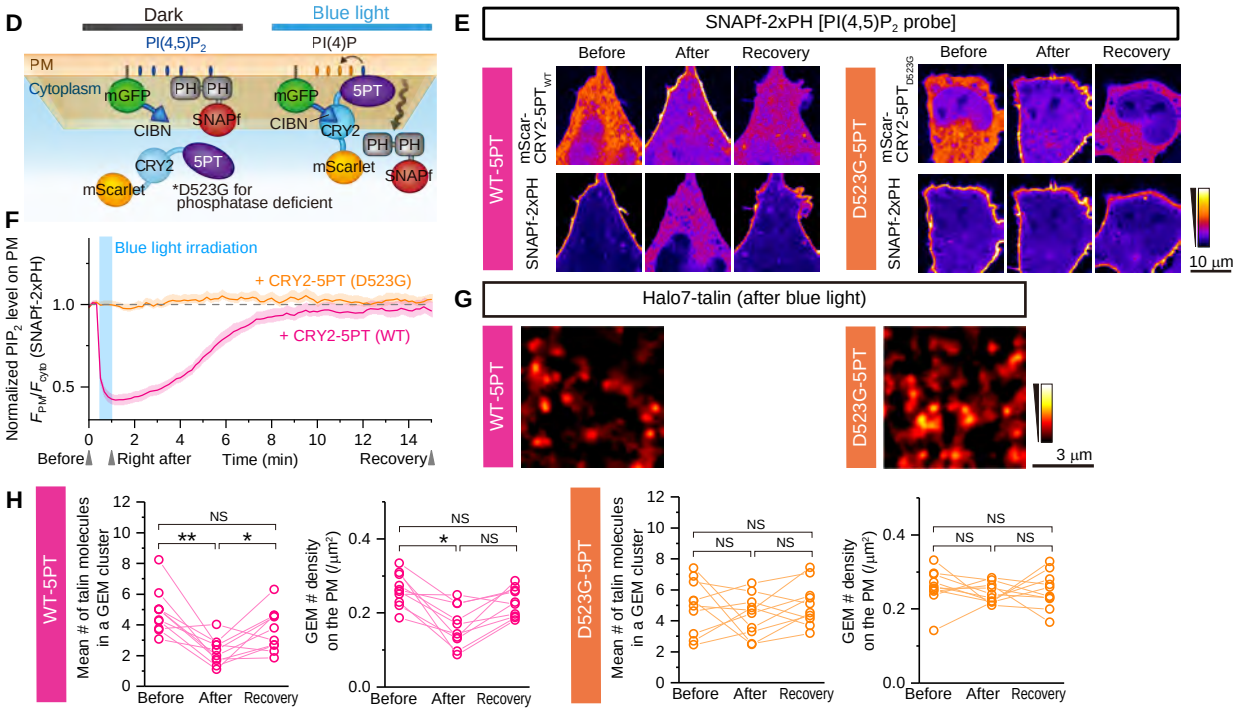

PI(4,5)P$_2$-reducing drugs decrease GEM size (talin-rescued dKO MEFs)

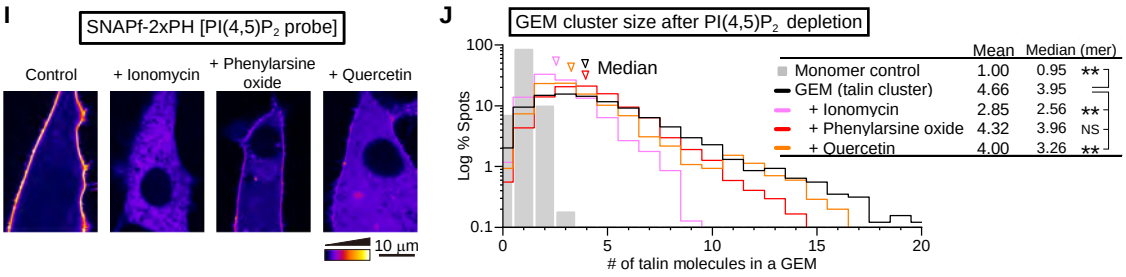

Figure S4

Conventional and PALM super-resolution images of mEos3.2-zyxin

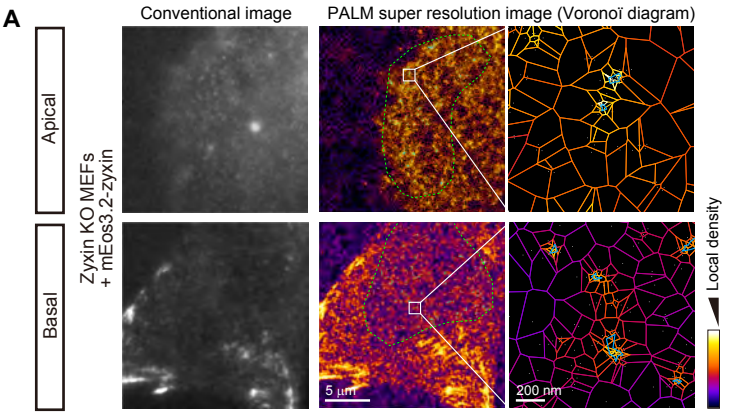

Simulation-based correction of PALM cluster diameters for localization error

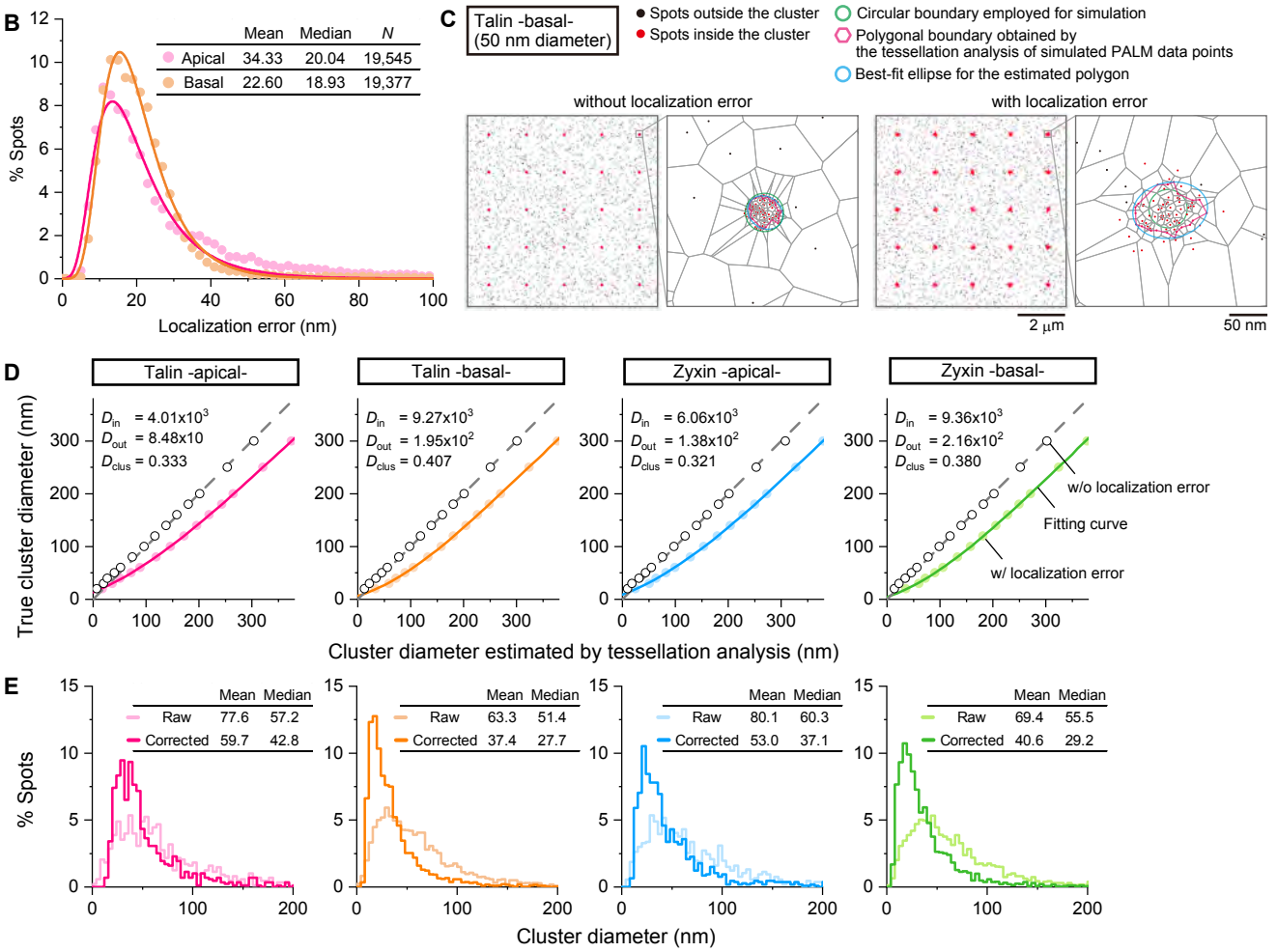

PALM quantification of talin and zyxin clusters

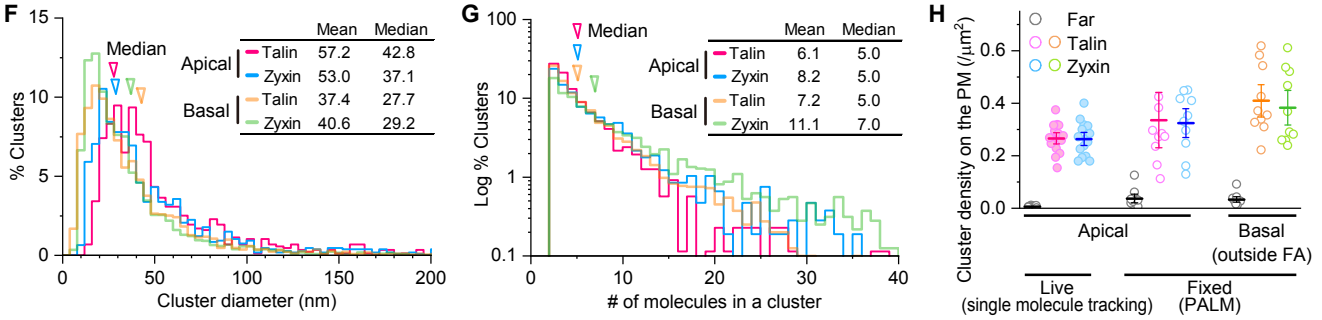

Figure S5

[*In vitro*] Formation of micron-scale liquid-like condensates of zyxin and VASP

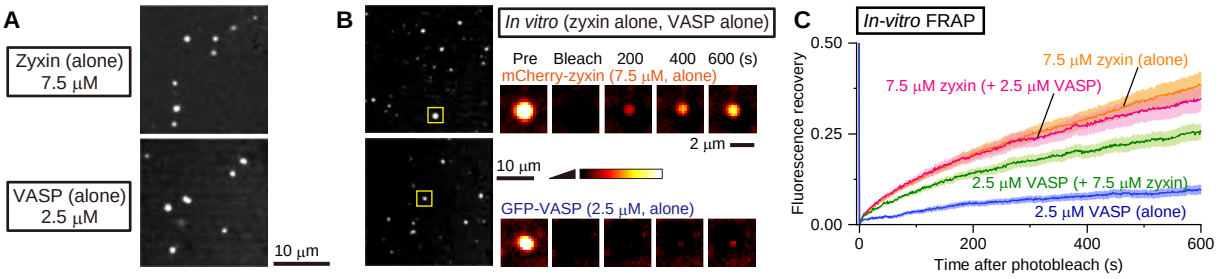

Coarse-grained MD simulations: single-chain Flory scaling and temperature-dependent zyxin IDR2 condensate stability

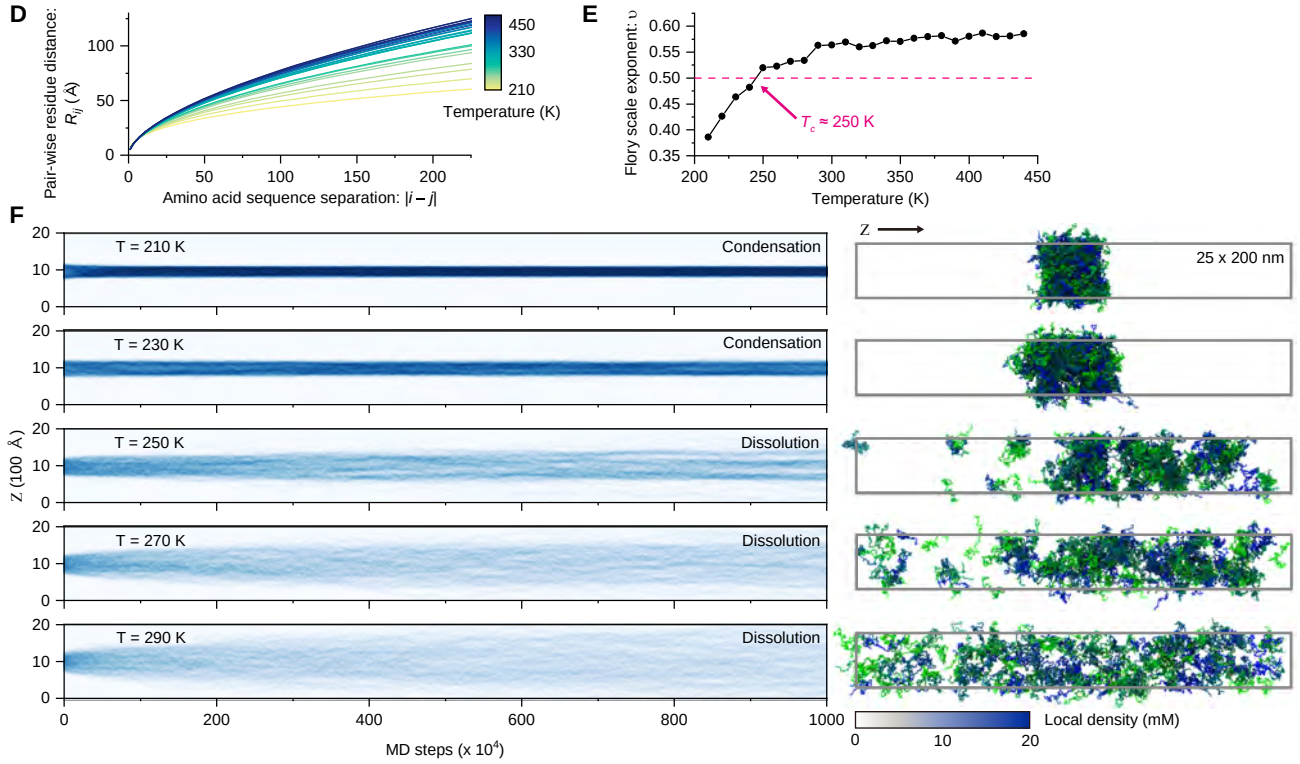

[In cells] Overexpression drives micron-scale zyxin/VASP condensates (not RIAM; Fig. 4H)

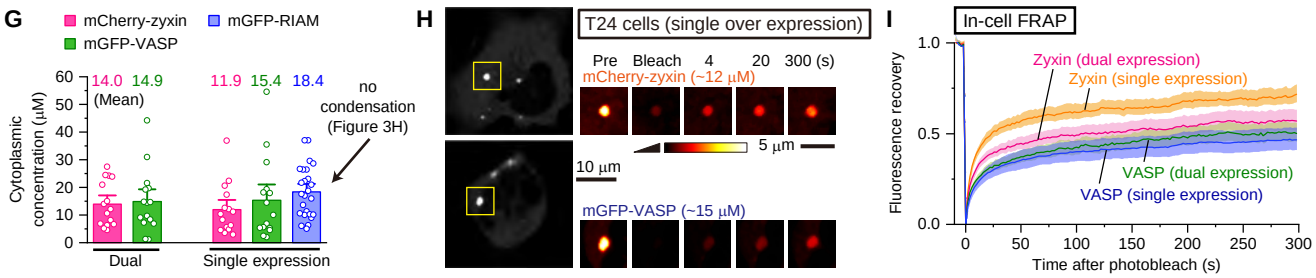

Quantifying zyxin/VASP copy numbers and cytoplasmic volume to estimate cytoplasmic concentrations (Figure 4D)

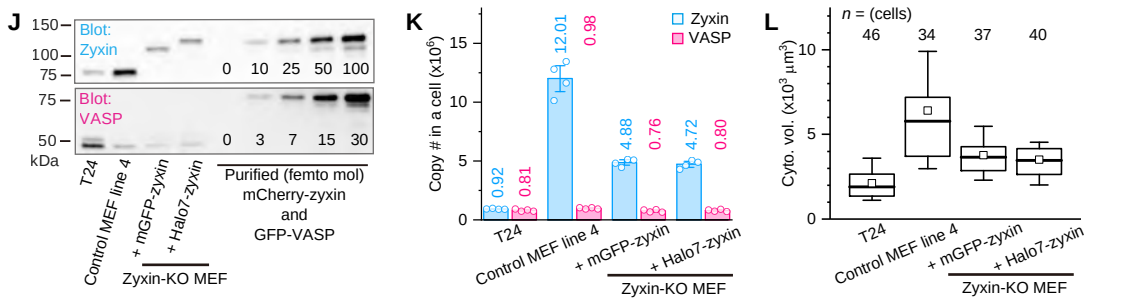

[In cells] GEM shows liquid-like dynamics with merging and splitting (talin-rescued dKO MEFs)

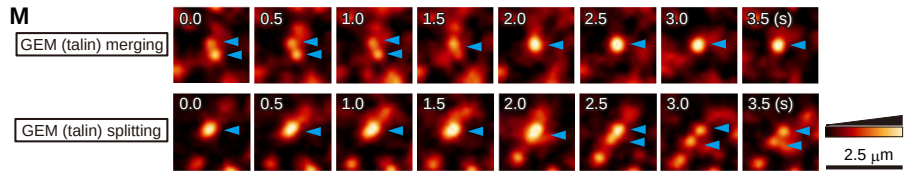

Figure S6

[In cells] OptoDroplet co-assembly of FAK and Lyn enhances Ca^{2+} responses to mild PDGF stimulation (zyxin-rescued KO MEFs)

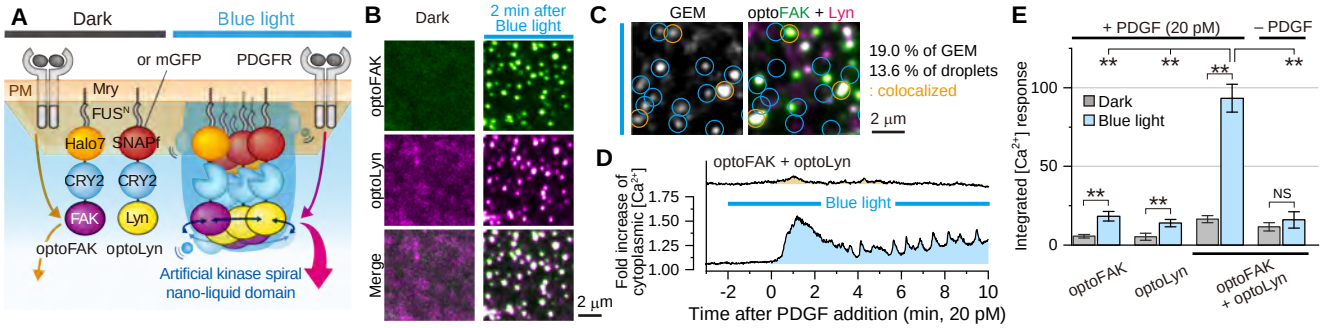

[In cells] Mild PDGF activates FAK in Lyn-containing optoDroplets (binder-tag; zyxin-rescued KO MEFs)

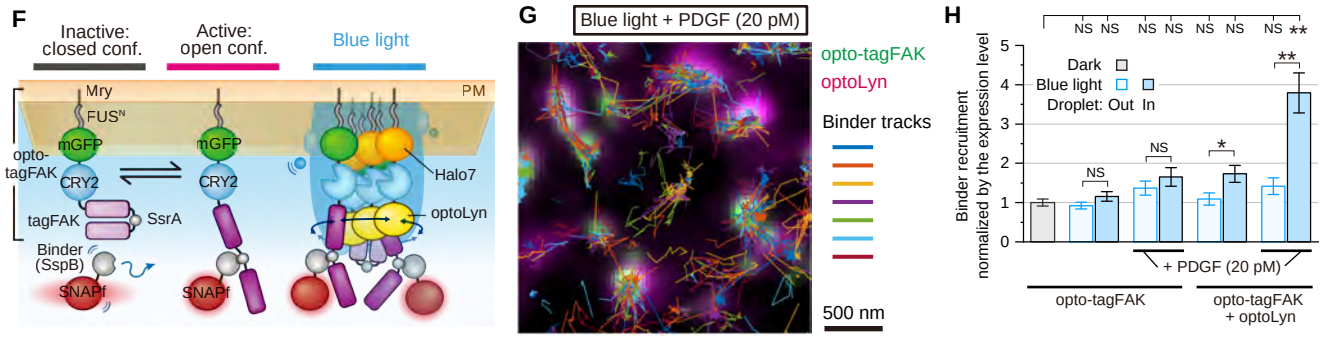

Figure S7

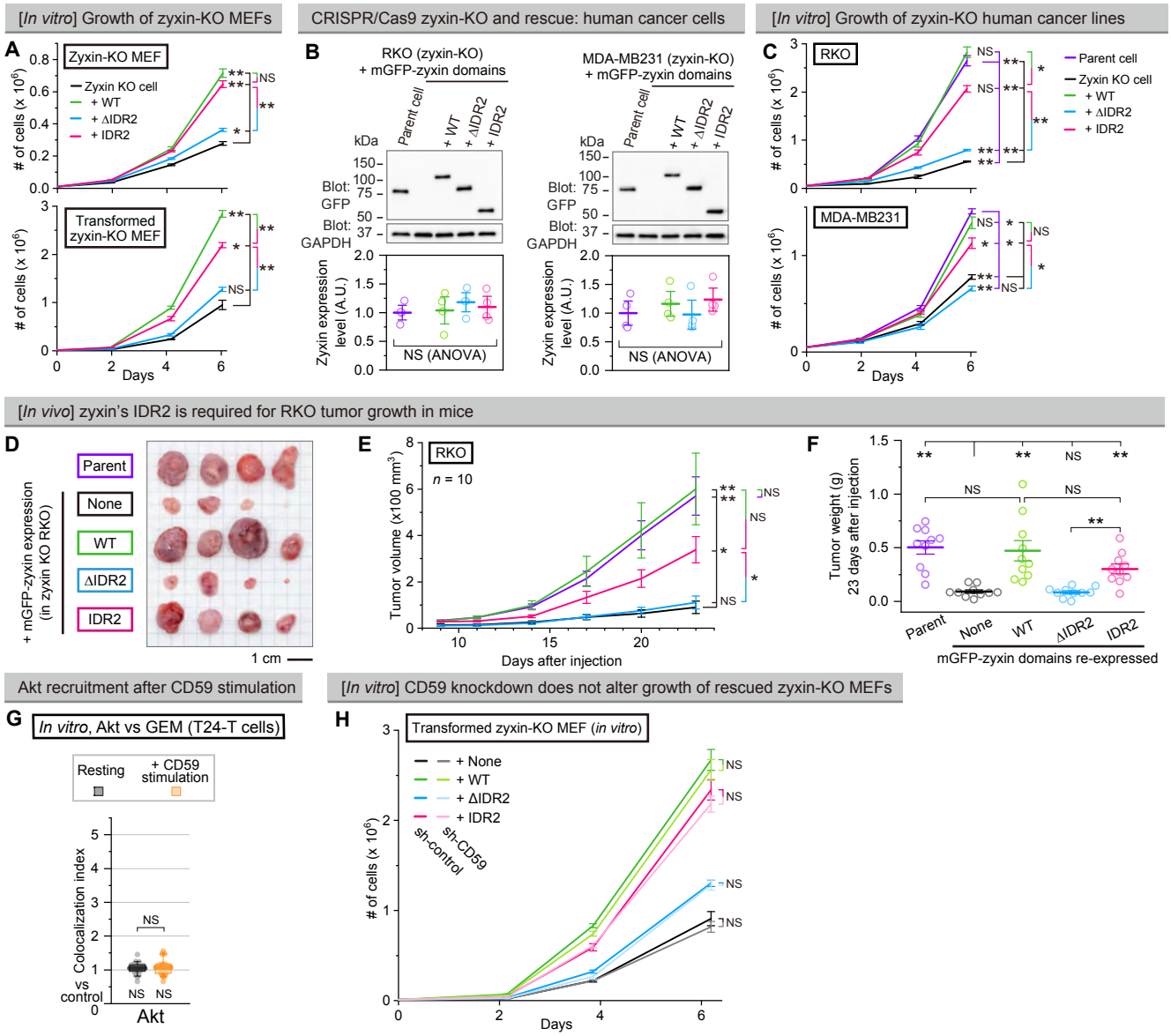
[In vitro] Growth of zyxin-KO MEFs
CRISPR/Cas9 zyxin-KO and rescue: human cancer cells
[In vitro] Growth of zyxin-KO human cancer lines
A
Zyxin-KO MEF
Zyxin KO cell
+ WT
+ ΔIDR2
+ IDR2
# of cells (x 10^6)
Transformed zyxin-KO MEF
Days
B
RKO (zyxin-KO)
+ mGFP-zyxin domains
MDA-MB231 (zyxin-KO)
+ mGFP-zyxin domains
Parent cell
+ WT
+ ΔIDR2
+ IDR2
kDa
Blot: GFP
Blot: GAPDH
Zyxin expression level (A.U.)
NS (ANOVA)
C
RKO
MDA-MB231
Parent cell
Zyxin KO cell
+ WT
+ ΔIDR2
+ IDR2
# of cells (x 10^6)
Days
[In vivo] zyxin's IDR2 is required for RKO tumor growth in mice
D
+ mGFP-zyxin expression (in zyxin KO RKO)
Parent
None
WT
ΔIDR2
IDR2
1 cm
E
RKO
n = 10
Tumor volume (x100 mm^3)
Days after injection
F
Tumor weight (g) 23 days after injection
Parent
None
WT
ΔIDR2
IDR2
mGFP-zyxin domains re-expressed
Akt recruitment after CD59 stimulation
G
In vitro, Akt vs GEM (T24-T cells)
Resting
+ CD59 stimulation
Colocalization index vs control
Akt
[In vitro] CD59 knockdown does not alter growth of rescued zyxin-KO MEFs
H
Transformed zyxin-KO MEF (in vitro)
+ None
+ WT
+ ΔIDR2
+ IDR2
sh-control
sh-CD59
# of cells (x 10^6)
Days